Measurement of Tau Neutrino Appearance and Charged-current Tau Neutrino Cross Section with Atmospheric Neutrinos in Super-Kamiokande

by

Zepeng Li

Department of Physics
Duke University

Date: _____

Approved:

_____
Christopher Walter, Supervisor

_____
Kate Scholberg

_____
Robert Behringer

_____
Shailesh Chandrasekharan

_____
Ying Wu

Dissertation submitted in partial fulfillment of the requirements for the degree of
Doctor of Philosophy in the Department of Physics
in the Graduate School of Duke University
2017

Abstract

Measurement of Tau Neutrino Appearance and Charged-current Tau Neutrino Cross Section with Atmospheric Neutrinos in Super-Kamiokande

by

Zepeng Li

Department of Physics
Duke University

Date: _____

Approved:

_____
Christopher Walter, Supervisor

_____
Kate Scholberg

_____
Robert Behringer

_____
Shailesh Chandrasekharan

_____
Ying Wu

An abstract of a dissertation submitted in partial fulfillment of the requirements for the degree of Doctor of Philosophy in the Department of Physics in the Graduate School of Duke University
2017

Abstract

Super-Kamiokande is a 50 kiloton water-Cherenkov detector in Japan, which has been collecting atmospheric neutrino data for more than 20 years. Tau neutrino appearance is expected in atmospheric neutrinos due to neutrino oscillations. The wide span of neutrino energies and neutrino path lengths in atmospheric neutrinos and the large target mass of Super-Kamiokande allow a detection of charged-current tau neutrino interactions in Super-Kamiokande.

This thesis describes a search for atmospheric tau neutrino appearance and a measurement of the charged-current tau neutrino cross section in Super-Kamiokande. A neural network is applied to identify charged-current tau neutrino interactions contained in the Super-Kamiokande detector. Using 5,326 days of atmospheric neutrino data, Super-K measures the tau normalization to be 1.47 ± 0.32 under the assumption of the normal hierarchy, relative to the expectation of unity for nominal oscillation parameters and assumed charged-current tau neutrino cross section. The result excludes the hypothesis of no-tau-appearance with a significance level of 4.6σ, thus giving a direct evidence of neutrino flavor change due to neutrino oscillations. By scaling the cross sections in the simulations to match Super-K data, a flux-averaged charged-current tau neutrino cross section is measured to be $(0.94 \pm 0.20) \times 10^{-38}$ cm^2, compared with the theoretical flux-averaged charged-current tau neutrino cross section of 0.64×10^{-38} cm^2. This is the second reported measurement of this process. The measured cross section is consistent with the Standard Model prediction.

To my family and my girlfriend.

Contents

List of Tables

List of Figures

List of Abbreviations and Symbols

Abbreviations

All abbreviations are defined in the text, but this section is designed to be a helpful reference for some of the more common ones.

CC	Charged-current
CCQE	Charged-current Quasi-Elastic
DIS	Deep Inelastic Scattering
ES	Elastic Scattering
Evis	Visible Energy
FC	Fully-contained
FSI	Final State Interaction
FV	Fiducial Volume
ID	Inner Detector
MC	Monter Carlo
MEC	Meson Exchange Current
MLP	Multilayer Perceptron
NC	Neutral-current
NN	Neural Network
OD	Outer Detector
PC	Partially-contained

PID	Particle Identification
PMT	Photomultiplier Tube
p.e.	photoelectron
SK	Super-Kamiokande
UPMU	Upward-going Muon
VME	Versa Module Europa

Acknowledgements

I want to first express my gratitude to my advisors, Professor Chris Walter and Kate Scholberg. They have guided me with their knowledge, patience and encouragement in the last six years. They are always ready to answer any of my questions on research. This thesis would not have been completed without their precious guidance.

I also want to thank the great people in the Duke neutrino group: Dr. Josh Albert, Dr. Tarek Akiri, Dr. Alex Himmel, Dr. Erin O'sullivan, Dr. Taritree Wongjirad, Gleb Sinev and Justin Raybern. I learned a lot during the many talks with you. I would like to especially thank Dr. Alex Himmel for guiding me in research and taking me to Japanese restaurants. Alex can always provide valuable help in coding, physics, and academic writing. I began to enjoy sushi after he took me to sushi restaurant when we were in Japan. It has been a great experience working with these great people.

It is really enjoyable working on the Super-Kamiokande experiment, especially in the ATMPD group. Prof. Ed Kearns and Prof. Masato Shiozawa provided valuable advise in this thesis project. Prof. Masato Shiozawa also helped to prepare document for my Japanese visa application for my every travel to Japan. Prof. Roger Wendell can always answer my questions on the ATMPD analysis software. Prof. Yoshinari Hayato taught me a lot on neutrino cross sections. There are many other collaborators from Japan and US that I want to thank. The analysis in this thesis relies on the great work from these collaborators.

I would like to thank my friends and colleagues at Duke. You helped me to get used to Durham and enjoy the life in Durham when I first came to US. You took me to many good Chines restaurants. Among these people, I owe Dong Wang a big thank because he drove me to the airport at 5 am and picked me up from the airport at 12 am in most of my trips to Japan or China. I forgot how many times you have done it. But I still remember you are ready to give a ride every time I turn to you for help. I feel lucky to meet so many good friends at Duke.

Finally, I want to thank my family. They have supported me all the way to my PhD degree. My parents do not know particle physics, but they always encourage me to chase my dream. My brother has given me a lot of help in life and study. He used his own experience to show me the wonderful life in college when I was still in middle school. It was especially important for a child from a rural area. He encouraged me to study abroad when I was in college. I could not have reached today without him. I also want to thank my girlfriend, Guirong Liu, for her love.

1

Introduction

The neutrino is one of the fundamental particles that make up the universe. It is the second most abundant particle in the Standard Model, after only photons, with tens of billions of neutrinos passing through every cubic centimeter of the Earth every second. Ths abundant particle is mysterious because it only interacts with other matter via weak interactions. The discovery of non-zero neutrino mass in the late 1990s opened the new field of neutrino oscillation. The study of neutrino oscillations has broadened our view of nature.

In this dissertation, I will talk about the study of one type of neutrino oscillations, atmospheric tau neutrino appearance in the Super-Kamiokande experiment. Super-Kamiokande is a large water Cherenkov detector in Gifu, Japan, designed to search for proton decay and to study neutrinos from various sources. It is credited for the discovery of the neutrino oscillations by measuring a deficit in the atmospheric muon neutrinos in 1998. This thesis describes a search for atmospheric tau neutrino appearance in Super-Kamiokande. Tau neutrino appearance is expected in the atmospheric neutrinos from three-flavor neutrino oscillations. Benefiting from the wide energy range of atmospheric neutrinos, Super-K is expected to detect charged-current

tau neutrino interactions in its large target mass. By measuring charged-current tau neutrino interactions, a measurement of tau neutrino appearance in Super-K is performed. This measurement is a direct confirmation of three-flavor neutrino oscillations. Additionally, the large expected sample of tau neutrinos in Super-K can shed light on the understanding of tau neutrino interactions. There is only one previously reported measurement of the charged-current tau neutrino cross section. This thesis reports a measurement of the cross section with a smaller uncertainty. The tools developed in the analysis are capable of identifying tau events statistically. Including this sample will increase the sensitivity to the neutrino mass hierarchy in the Super-K three-flavor atmospheric neutrino oscillation analysis.

1.1 Neutrino History

The study of β decay provided the first hint of the existence of the neutrino. The process was thought to be a two-body decay which should produce a discrete energy spectrum as in alpha radiation. However, the spectrum of the beta particle was measured to be continuous, which was in apparent contradiction to the law of conservation of energy. The neutrino was postulated by Wolfgang Pauli (Pauli, 1930) in 1930 to explain the continuous energy spectrum of β decay. In Pauli's new theory, an electrically neutral particle that was not detected in the β decay was responsible for carrying away the energy. By adding this new particle, energy and momentum are conserved in β decay. Based on the evidence at that time, Pauli also predicted that the new neutral particle had a small mass and 1/2 spin, and named it the "neutron".

An electrically neutral particle was discovered soon by Chadwick and he also named it a neutron. However, that particle is much more massive than that postulated by Pauli. We now know that Chadwick discovered what is now known as the neutron. Later, in 1934, Enrico Fermi developed a theory of beta decay (Fermi, 1934). In this theory, the neutron discovered by Chadwick decays into a proton,

an electron and the "neutron" postulated by Pauli. Fermi renamed the particle the neutrino, meaning "little neutral one" in Italian. Fermi's theory of beta decay posits four fermions interacting directly with one another

$$n \rightarrow p + e^{-} + \bar{\nu}_e. \tag{1.1}$$

Fermi's theory of beta decay has a four-point vector current, which only describes the beta decays between nuclear states with identical angular momenta. Later in 1936, Fermi's theory was extended by Gamow and Teller to explain some types of beta decay that involved a change in 1 unit of nuclear spin (Gamow and Teller, 1937).

Two decades after Pauli's proposal, the neutrino was first discovered by Reines and Cowan in 1956 (Cowan et al., 1956) via an inverse beta decay process: $\bar{\nu}_e + p \rightarrow n + e^{+}$. Using $CdCl_2$-doped water, Reines and Cowan observed this reaction through the coincidence measurements of gamma rays from positron annihilation and the delayed gamma rays from the neutron's capture on cadmium. Later in 1962, Lederman, Schwartz and Steinberger confirmed the existence of the muon neutrino (Danby et al., 1962) using a neutrino beam produced by the decay of charged pions into a beam of muon neutrinos. The experiment found that the interactions of neutrinos in the beam produced muons but no electrons, confirming that the muon neutrino is a distinct particle. The tau neutrino was discovered in 2001 by the DONuT experiment (Kodama et al., 2001) through the detection of tau leptons in neutrino interactions. Electron neutrino, muon neutrino and tau neutrino make up three generations of neutrinos, corresponding to three generations of charged leptons (electron, muon and tau).

In 1955, Davis exposed 3,800 liters of CCl_4 to the Brookhaven Graphite Research Reactor to search for the reaction of $\bar{\nu}_e + {}^{37}\mathrm{Cl} \rightarrow e^{-} + {}^{37}\mathrm{Ar}$ (Davis, 1955). By not observing the process, it was confirmed that ν_e and its anti-particle $\bar{\nu}_e$ are different. The same applies to muon neutrinos, which was later found at CERN because in

ν_μ interactions only μ^- in the final state were detected, but not μ^+ (Bienlein et al., 1964).

Parity is defined as a symmetry transformation by an inversion of one spatial coordinate at the origin. In 1956, Lee and Yang found that parity conservation had never been tested for weak interactions and suggested a number of tests (Lee and Yang, 1956). Wu then measured the beta decays of polarized ^{60}Co nuclei (Wu et al., 1957). The decay of ^{60}Co is given by

$$^{60}\mathrm{Co} \rightarrow {}^{60}\mathrm{Ni}^* + e^- + \bar{\nu}_e. \tag{1.2}$$

It was observed that electrons are preferentially emitted in the opposite spin direction to that of the ^{60}Co nucleus, showing that parity is maximally violated in weak interactions. The experiment implies that the neutrino exist in only one helicity state where helicity is defined as the projection of particle's spin along the direction of its momentum. Later in the classic experiment by Goldhaber that used the electron capture of ^{152}Eu (Goldhaber et al., 1958), the helicity of the neutrino was measured to be -1.

The discovery of parity violation suggested that a new approach was needed to describe the true form of weak interactions. In 1957, Robert Marshak and George Sudarshan (Sudarshan and Marshak, 1994) and Richard Feynman and Murray Gell-mann (Feynman and Gell-Mann, 1958) independently proposed a V-A (vector minus axial vector) Lagrangian for the weak interaction. In this theory, the weak interaction only acts on left-handed particles and on right-handed antiparticles, and maximizes parity violation.

1.2 The Standard Model Electroweak Theory

The Standard Model of particle physics is a theory that describes the electroweak (a unification of the weak and electromagnetic interactions) and strong interactions.

In the Standard Model, neutrinos only interact via the weak force; thus electroweak theory is the only part of the Standard Model that is discussed below.

Schwinger was the first to suggest the existence of intermediate vector bosons in weak interactions. In 1957, he proposed a gauge theory of weak interactions that are mediated by two charged bosons (which he named Z^+ and Z^-) (Schwinger, 1957). In the same paper, he also first suggested the unification of electromagnetic interactions and weak interactions. The unification was first formulated by Glashow as a gauge field with SU(2)×U(1) symmetry (Glashow, 1961), and a neutral gauge boson Z^0 was added in the new theory. Salam and Ward proposed a similar model based on SU(2)×U(1) symmetry independently (Salam and Ward, 1964). The SU(2) symmetry defines the weak isospin group. The leptons and quarks that participate in the weak interactions are grouped into isospin doublets, and the leptons that do not interact via the weak interaction are defined as weak isospin singlets. The spontaneous breaking of symmetry through the Higgs mechanism leads to a set of massive vector bosons, W^+, W^- and Z^0 that mediate the weak interaction (Weinberg, 1967; Salam, 1968). This new theory of electroweak interactions is also known as Glashow-Weinberg-Salam theory.

In the Standard Model, the neutrinos only interact with other matter through the exchange of these bosons. The interactions are classified into charged-current interactions and neutral-current interactions based on which boson takes part in the interaction. In the charged-current interaction, a neutrino changes to a charged lepton of the same flavor (or vice versa) via exchanging of a $W^\pm$ vector boson with another particle. In the neutral-current interaction, a neutrino exchanges a Z^0 vector boson with another particle, where the flavor of the neutrino is irrelevant. Fig. 1.1 shows the Feynman diagrams of neutrino interaction vertices.

The Standard Model electroweak theory has withstood all experimental challenges since its inception. In 1973, neutral current interactions were observed in the

(a) Charged-current interactions (b) Neutrino-current interactions.

FIGURE 1.1: Feynman diagrams of neutrino interactions in the Standard Model. (a) Feynman diagram vertex for charged-current interactions where a neutrino changes to a charged lepton (or vice versa) via the exchange of the $W^{\pm}$ vector boson with another particle. (b) Feynman diagram vertex for neutral-current interactions where a neutrino interacts via the exchanges of the Z^0 vector boson.

Gargamelle experiment at CERN (Hasert et al., 1973) and at Fermilab (Benvenuti et al., 1974), which was proposed in the GWS theory but not yet observed at the time the theory was proposed. The $W^{\pm}$ vector bosons were discovered in the UA1 and UA2 experiments at CERN (Arnison et al., 1983; Banner et al., 1983), and the Z^0 was discovered later in the same experiments. Both experiments measured the masses of three vector bosons that were in good agreement with the Standard Model prediction. The existence of the Higgs field which is responsible for the mass of $W^{\pm}$ and Z^0 bosons was also proved by the discovery of the Higgs boson in the ATLAS and CMS experiments at CERN (Aad et al., 2012; Chatrchyan et al., 2012).

The number of light neutrino types can also be determined by measuring the width of the Z^0 boson in collider experiments. Z^0 bosons decay into quarks and charged leptons as well as into neutrinos which are invisible in collider experiments. The invisible partial width, Γ_{inv}, due to Z^0 decays into neutrinos is determined by subtracting the measured partial widths, corresponding to Z^0 decays to quarks and charged leptons, from the total Z^0 width. Fig. 1.2 shows the measurement of the hadron production cross section around the Z^0 resonance from four LEP experiments compared with predicted cross section for two, three and four types of neutrino. The

combined result from four LEP experiments measured the number of neutrino types to be 2.984±0.008.

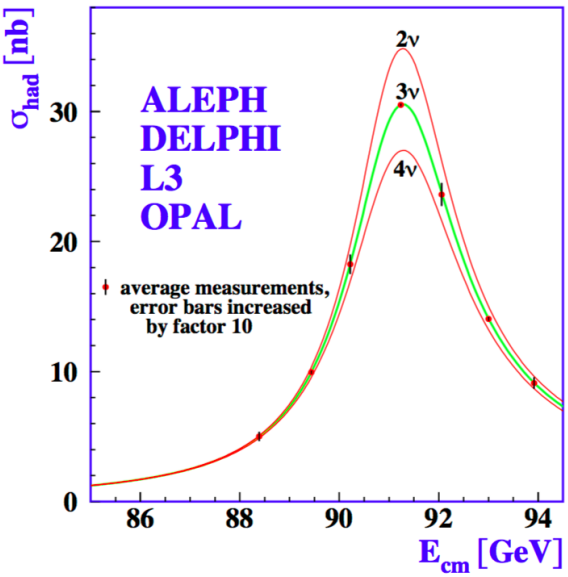

FIGURE 1.2: Measurements of the hadron production cross-section around the Z resonance. The curves indicate the predicted cross-section for two, three and four neutrino species with SM couplings and negligible mass. Taken from (Schael et al., 2006).

1.3 Atmospheric Neutrinos

The analysis in this thesis is performed with the study of atmospheric neutrinos. Atmospheric neutrinos are produced in the interactions of cosmic rays with nuclei in the upper atmosphere, as shown in Fig. 1.3. The interaction produces a shower of hadrons, mostly pions and kaons. The dominant decay (branching ratio > 99%) of charged pions produces a muon and a neutrino, and the muon further decays into a electron, one electron neutrino and one muon neutrino.

$$\pi^+ \rightarrow \mu^+ + \nu_\mu \tag{1.3a}$$

$$\hookrightarrow e^+ + \nu_e + \bar{\nu}_\mu \tag{1.3b}$$

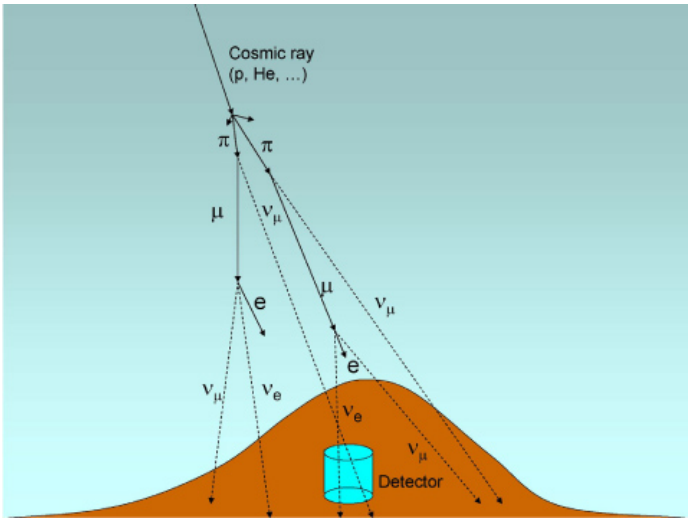

FIGURE 1.3: A schematic representation of atmospheric neutrino production in cosmic ray interactions, taken from (Kajita, 2006).

$$\pi^- \rightarrow \mu^- + \bar{\nu}_\mu \tag{1.3c}$$

$$\hookrightarrow e^- + \bar{\nu}_e + \nu_\mu \tag{1.3d}$$

Based on this kinematic chain, the ratio of muon neutrinos to electron neutrinos is expected to be around 2 below 1 GeV. The ratio is modified at higher energies where neutrinos are produced by decays of more energetic parents. Some muons produced in these decays reach the Earth before decaying due to Lorentz time dilation. Consequently, no electron neutrinos are produced and the ratio of muon to electron neutrino increases with energy.

The flux of cosmic rays above about 10 GeV is isotropic about the Earth; thus the flux of neutrinos is expected to be equal for equal angles with the zenith and nadir. The path length of atmospheric neutrinos varies from $O(10)$ km to $O(10^4)$ km. Due to the wide energy span of cosmic rays, atmospheric neutrinos have energies spanning from $O(10)$ MeV to above PeV. The wide span in path length and energy makes atmospheric neutrinos a robust souce for studying neutrino oscillations.

1.4 Neutrino Oscillations

1.4.1 Discovery of Neutrino Oscillations

The Sun's energy comes from nuclear fusion reactions in which neutrinos are also produced. The flux of neutrinos at the Earth is several ten billion per square centimeter per second. In the late 1960s, the Homestake experiment first measured the flux of neutrinos from the Sun, and found a deficit compared to the prediction of the Standard Solar Model (Davis, 1994). The deficit was confirmed by subsequent experiments, such as Kamiokande (Fukuda et al., 1996), SAGE (Abdurashitov et al., 1999) ,GALLEX (Hampel et al., 1999) and Super-Kamiokande (Fukuda et al., 2001). The discrepancy is known as the solar neutrino anomaly (Bahcall et al., 1996).

Another anomaly was later found in the atmospheric neutrinos. As discussed in Section 1.3, the ratio of ν_μ/ν_e is expected to be around 2 at energies below 1 GeV. However, atmospheric neutrino experiments measured a value significantly smaller than 1 (Fukuda et al., 1994; Becker-Szendy et al., 1992; Allison et al., 1999), indicating that either there was less ν_μ in the data than in the prediction, or there was more ν_e, or both.

The efforts to resolve these two anomalies led to the discovery of neutrino oscillations. The atmospheric neutrino anomaly was first solved by the successor of Kamiokande experiment, Super-Kamiokande, which measured the flux of atmospheric neutrinos with unprecedented precision. The Super-Kamiokande collaboration announced that they had found the evidence for neutrino oscillations in atmospheric neutrinos in 1998 (Fukuda et al., 1998). As shown in Fig. 1.4, the measured neutrino flux showed dependence on zenith angle for muon neutrinos, but not for electron neutrinos. The deficit in the observed ν_μ coming from below, but not from above, was consistent with $\nu_\mu \rightarrow \nu_\tau$ oscillation.

The solar neutrino anomaly was later solved by the Sudbury Neutrino Observa-

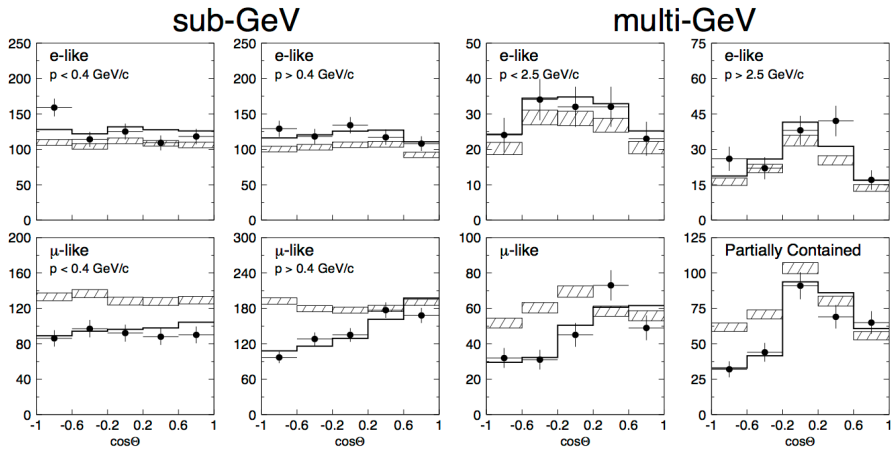

FIGURE 1.4: The zenith angle distributions of $\mu-$like and $e-$ like events in Super-Kamiokande. Upward-going particles have $\cos\Theta > 0$ and downward-going ones have $\cos\Theta < 0$. The hatched regions show the Monte Carlo expectations for no oscillations normalized to the data live-time with statistical errors, and the solid line is the expectations with the best-fit oscillation. Taken from (Fukuda et al., 1998).

tory (SNO) collaboration in 2002, which found direct evidence for neutrino flavor transformation in solar neutrinos (Ahmad et al., 2002). SNO used a tank of D_2O as its target to detect charged-current (CC) interactions, electron elastic scattering (ES), and neutral-current (NC) interactions. The CC interaction is only sensitive to ν_e therefore only measures ν_e flux. For ES, electron neutrinos can interact via both the charged and neutral currents, while ν_μ and ν_τ only interact via neutral current at solar neutrino energies. This channel measures a combination of the electron, muon and tau neutrino flux. The NC interaction is sensitive to all neutrino flavors, thus measures the total flux. As shown in Fig. 1.5, SNO measured a total flux consistent with the Standard Solar Model prediction, but a deficit of electron neutrinos. The result is consistent with $\nu_e \rightarrow \nu_{\mu/\tau}$ oscillation. The solar neutrino anomaly was finally understood, and neutrino flavor transformation was confirmed.

1.4.2 Neutrino Mixing

Neutrino oscillations occur because neutrino flavor eigenstates are not identical to the mass eigenstates. A neutrino flavor eigenstate is composed of a linear combination

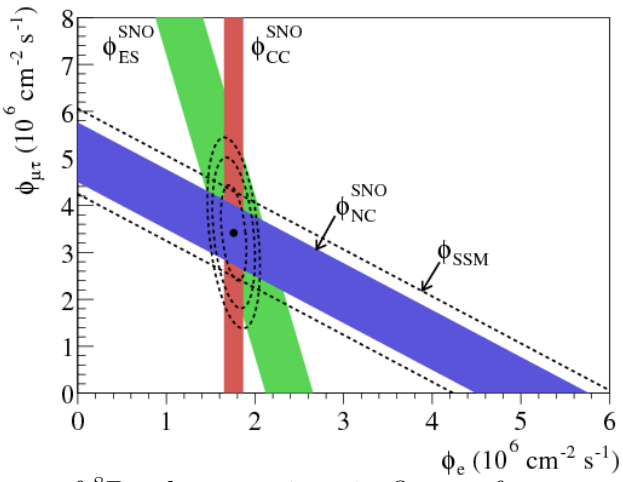

FIGURE 1.5: Fluxes of ^{8}B solar neutrinos in flavor of μ or τ vs electrons deducted from the three neutrino reactions in SNO. The diagonal bands show the total flux from the Standard Solar Model prediction (dashed) and the measurement with NC reaction in SNO. Taken from (Ahmad et al., 2002).

of mass eigenstates, ν_1, ν_2, ν_3, through a mixing matrix, which is analogous to the CKM matrix used for quarks. The flavor eigenstates of neutrinos can be expressed by mixing of mass eigenstates as:

$$\begin{pmatrix} \nu_e \\ \nu_\mu \\ \nu_\tau \end{pmatrix} = \begin{pmatrix} U_{e1} & U_{e2} & U_{e3} \\ U_{\mu 1} & U_{\mu 2} & U_{\mu 3} \\ U_{\tau 1} & U_{\tau 2} & U_{\tau 3} \end{pmatrix} \begin{pmatrix} \nu_1 \\ \nu_2 \\ \nu_3 \end{pmatrix} \tag{1.4}$$

the matrix is known as Pontecorvo-Maka-Nakagawa-Sakata (PMNS) matrix, which is a complex unitary matrix. Therefore, a neutrino of flavor α can be expressed as:

$$\nu_\alpha = \sum_i U_{\alpha i} \nu_i. \tag{1.5}$$

1.4.3 Neutrino Oscillations in Vacuum

Suppose a neutrino beam is produced containing flavor eigenstate ν_α at the origin of x-axis and time 0 and the neutrinos are aimed along the x-axis in free space, the mass eigenstates propagate according to the time-dependent Schrödinger equation

with no potentials

$$i\frac{\partial}{\partial t}\left|\nu_i(x,t)\right\rangle = H\left|\nu_i(x,t)\right\rangle \tag{1.6}$$

The time evolution of the wave-function is determined by the time evolution of the mass eigenstates and can be written as

$$\left|\nu_k(x,t)\right\rangle = e^{-i\phi_k}\left|\nu_k\right\rangle, \tag{1.7}$$

where $\phi_k = p_i \cdot x_i$ is the phase of the plane wave representing the mass eigenstate. We can transform the Schrödinger equation to be expressed in the flavor basis as:

$$\left|\nu_\alpha(x,t)\right\rangle = \sum_k U_{\alpha k} e^{-i\phi_k} \sum_\beta U^*_{\beta k}\left|\nu_\beta\right\rangle = \sum_\beta \sum_k U^*_{\beta k} e^{-i\phi_k} U_{\alpha k}\left|\nu_\beta\right\rangle. \tag{1.8}$$

The amplitude for detecting a neutrino of flavor β is

$$A_{\alpha\beta} = \sum_k e^{-i\phi_k} U^*_{\alpha k} U_{\beta k}, \tag{1.9}$$

The probability of a neutrino changing to a different flavor is then:

$$\begin{aligned} P(\nu_\alpha \to \nu_\beta) =& |A_{\alpha\beta}|^2 \\ =& \delta_{\alpha\beta} - 4\sum_{i>j} Re(U^*_{\alpha i} U_{\beta i} U_{\alpha j} U^*_{\beta j}) \sin^2(\Delta m^2_{ij}\frac{L}{4E})) \\ &+ 2\sum_{i>j} Im(U^*_{\alpha i} U_{\beta i} U_{\alpha j} U^*_{\beta j}) \sin\left(\Delta m^2_{ij}\frac{L}{2E}\right)), \end{aligned} \tag{1.10}$$

where $\Delta m^2_{ij} = m^2_i - m^2_j$, L is the path length of the neutrino, and the phase difference between two mass states, $\phi_i - \phi_j$ can be expressed as $L\frac{m^2_i - m^2_j}{2E}$ since the mass of the neutrino (< 1 eV) is much smaller than the energies (> 1 MeV) of current experiments.

A simple case to consider is the oscillation between two neutrino flavors. In this scenario, there is only one mass-squared difference, and the mixing matrix U reduces

to a 2× 2 unitary matrix with one degree of freedom.

$$U = \begin{pmatrix} \cos\theta & \sin\theta \\ -\sin\theta & \cos\theta \end{pmatrix}, \tag{1.11}$$

where θ is the mixing angle. Equation 1.10 reduces to a simpler form

$$P(\nu_\alpha \to \nu_\beta) = \begin{cases} 1 - \sin^2 2\theta \sin^2 \frac{\Delta m^2 L}{4E}, \alpha = \beta \\ \sin^2 2\theta \sin^2 \frac{\Delta m^2 L}{4E}, \alpha \neq \beta \end{cases}, \tag{1.12}$$

where $\Delta m^2 = m_2^2 - m_1^2$. Note that here and above, we have used natural units. If converting from natural units to laboratory units, there is the change,

$$\frac{\Delta m^2 L}{4E} \to \frac{1.27 \Delta m^2 L}{E} \Big[\frac{eV^2 \cdot km}{GeV}\Big]. \tag{1.13}$$

1.4.4 Neutrino Oscillations in Matter

All the calculations of neutrino oscillations so far have been assuming the neutrinos propagate in vacuum. The oscillations arise from a difference in phase between the mass eigenstates solely due to the mass differences. However, this has to be modified in matter where the phase difference is determined by the total energy of the mass eigenstate. Neutral-current interactions are flavor independent, and so produce a common phase for all components of neutrinos. However, since the Earth contains a large number of electrons, electron neutrinos may interact with them via the $W^\pm$ bosons, while the muon and the tau neutrino do not. Therefore, electron neutrinos passing through matter are affected by coherent elastic forward scattering, as shown in Fig. 1.6, adding a potential to electron neutrinos. The resulting effective potential that electron neutrinos feel is expressed as

$$V_e = \pm\sqrt{2} G_F n_e, \tag{1.14}$$

where G_F is Fermi's constant and n_e is the electron density of the matter, and the contribution is positive for ν_e and negative for $\bar{\nu}_e$. The influence of matter on neutrino

oscillations is often referred to as the MSW effect (Wolfenstein, 1978; Mikheev and Smirnov, 1985).

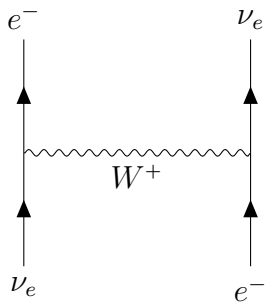

FIGURE 1.6: Neutrino CC forward elastic scattering in matter. This reaction adds a potential to the electron neutrinos.

It is fairly easier to demonstrate the MSW effect in two-neutrino mixing and oscillations where one component is the electron neutrino. The neutrino is then assumed to pass through a medium with constant density. In this model, the Schrödinger equation is

$$i\frac{d}{dt}\begin{pmatrix}\nu_e\\ \nu_\beta\end{pmatrix} = H\begin{pmatrix}\nu_e\\ \nu_\beta\end{pmatrix}, \tag{1.15}$$

where H is the Hamiltonian operator. In a vacuum, this operator is

$$H_{vac} = \begin{pmatrix}E_1 & 0\\ 0 & E_2\end{pmatrix} \approx pI + \begin{pmatrix}\frac{m_1^2}{2E} & 0\\ 0 & \frac{m_2^2}{2E}\end{pmatrix}. \tag{1.16}$$

We define the neutrino mixing by

$$\begin{pmatrix}\nu_e\\ \nu_\beta\end{pmatrix} = \begin{pmatrix}\cos\theta & \sin\theta\\ -\sin\theta & \cos\theta\end{pmatrix}\begin{pmatrix}\nu_1\\ \nu_2\end{pmatrix}. \tag{1.17}$$

Then we transform the Schrödinger equation to be expressed in the flavor basis as

$$i\frac{d}{dt}\begin{pmatrix}\nu_e\\ \nu_\beta\end{pmatrix} = UH_{vac}U^\dagger\begin{pmatrix}\nu_e\\ \nu_\beta\end{pmatrix} = \frac{\Delta m^2}{2E}\begin{pmatrix}\sin^2\theta & \sin\theta\cos\theta\\ \sin\theta\cos\theta & \cos^2\theta\end{pmatrix}\begin{pmatrix}\nu_e\\ \nu_\beta\end{pmatrix}. \tag{1.18}$$

Note that we have subtracted a component proportional to the identity matrix that will not affect the oscillation. Then we have to add an effective potential to the Schrödinger equation that only appears in the e-e component of the weak basis

$$H_m = \begin{pmatrix} V_e & 0 \\ 0 & 0 \end{pmatrix}. \tag{1.19}$$

The total effective Hamiltonian in the weak basis is

$$H = UH_{vac}U^\dagger + H_m = \frac{\Delta m^2}{2E}\begin{pmatrix} \sin^2\theta + \frac{2E}{\Delta m^2}V_e & \sin\theta\cos\theta \\ \sin\theta\cos\theta & \cos^2\theta \end{pmatrix}. \tag{1.20}$$

Note that the mass matrix is no longer diagonal, meaning that the mass eigenstates in matter are not identical to the mass eigenstates in the vacuum. In order to get the correct eigenstates, we need to diagonalize this matrix. The eigenvalues are $\pm\Delta m^2_M = \pm\frac{\Delta m^2}{4E} f_m$ where

$$f_m = \sqrt{\sin^2 2\theta + (\cos 2\theta - \frac{2E}{\Delta m^2}V_e)^2}. \tag{1.21}$$

And the mixing matrix in matter, U_M, is

$$U_M = \begin{pmatrix} \cos\theta_M & \sin\theta_M \\ -\sin\theta_M & \cos\theta_M \end{pmatrix}, \tag{1.22}$$

where it turns out that

$$\begin{aligned} \cos 2\theta_M =& \frac{1}{f_m}(\cos 2\theta - \frac{\Delta m^2}{2E}V_e) \\ \sin 2\theta_M =& \frac{1}{f_m}\sin 2\theta. \end{aligned} \tag{1.23}$$

The two-neutrino oscillation probability in matter in terms of the variables θ_M and Δm^2_M is

$$P(\nu_e \to \nu_\beta) = \sin^2 2\theta_M \sin^2 \frac{\Delta m^2_M L}{E}. \tag{1.24}$$

Obviously, the vacuum oscillations are restored as the matter density gets smaller. Additionally, there exists a resonance effect at certain energies and densities when $\sin^2 2\theta_M = 1$, which was first pointed out by Mikheev and Smirnov (Mikheev and Smirnov, 1985).

It should be noted that the matter effect can determine the sign of the mass splitting. In the mass splitting parameter, Δm^2_M, there is a term $(\Delta m^2 - 2EV_e/\cos\theta)^2$. Depending on the sign of Δm^2, the matter potential, V_e, is part of a term that adds or subtracts from the vacuum mass splitting. In atmospheric neutrinos, the matter effect is a sub-leading factor because neutrinos coming from the bottom of the detector travel a long distance through matter. Therefore, atmospheric neutrino oscillations can in principle help to distinguish the sign of the mass splitting.

For three-flavor neutrino oscillations, it is not possible to calculate the matter effect so elegantly. The change of density in the Earth adds more difficulties to the calculation in the atmospheric neutrino oscillations. For the analysis described here, we use a solution in (Barger et al., 1980) to account for the matter effect. For the density profile of the Earth, we numerically calculate the probabilities by iterating the calculation through a series of constant density layers (Wendell et al., 2012).

1.4.5 Experimental Status

Since the discovery of neutrino oscillations, many experiments have been performed to measure different flavor oscillations using diverse sources of neutrinos, such as solar neutrinos (Ahmad et al., 2002; Fukuda et al., 2001), atmospheric neutrinos (Abe et al., 2011b), accelerator neutrinos (Ahn et al., 2003; Michael et al., 2006; Abe et al., 2012a) and reactor neutrinos (Abe et al., 2012b; An et al., 2012; Ahn et al., 2012). The experimental status of neutrino oscillations is summarized below.

The current values of $\sin^2\theta_{12}$ and Δm^2_{21} come from the measurement of solar neutrinos and reactor neutrinos. Super-K and SNO measured the oscillations of

solar neutrinos as described earlier in this chapter (Ahmad et al., 2002; Fukuda et al., 2001). The oscillations were later confirmed by the KamLAND experiment which measured $\bar{\nu}_e$ disappearance using $\bar{\nu}_e$ coming from reactors (Araki et al., 2005). The neutrinos measured by KamLAND were from sources at various distances to their detector; thus they were exposed to sources with a wide range of L/E. This allowed the experiment to measure a precise sinusoidal L/E dependence of neutrino oscillations (Araki et al., 2005). Fig. 1.7 shows the number of observed events as a function of L/E.

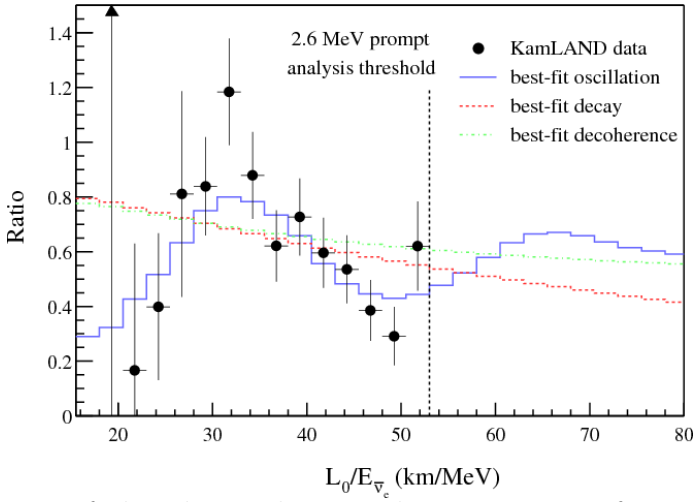

FIGURE 1.7: Ratio of the observed $\bar{\nu}_e$ to the expectation for no oscillation as a function of L/E. Taken from (Araki et al., 2005).

The combination of the these three experiments, Super-K, SNO, and KamLAND put the tightest constraints on the oscillation parameters, $\sin^2\theta_{12}$ and Δm^2_{21}. Fig. 1.8 shows the constraints on these parameters from the three experiments. In this analysis, the values for the solar parameters come from a global fit in the 2014 PDG (Olive et al., 2014).

As discussed earlier in this chapter, Super-K played an important role in the discovery of neutrino oscillations. Super-K has been measuring the oscillations of atmospheric neutrinos since its start, and provides one of the best measurements of

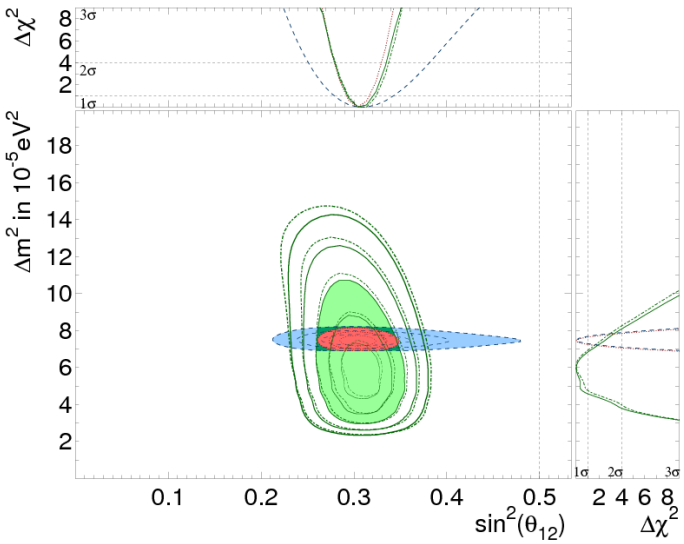

FIGURE 1.8: Allowed contours of $\sin^2\theta_{12}$ and Δm^2_{21} for Super-K solar neutrino data (green solid), Super-K+SNO (green dashed), KamLAND (blue), and combined results (red). Taken from (Sekiya, 2013).

$\sin^2\theta_{23}$ and Δm^2_{32} (Abe et al., 2011b). IceCube-DeepCore is another experiment that measured these parameters by measuring the oscillations of atmospheric neutrino with energies higher than 10 GeV (Aartsen et al., 2016). Recently, the long-baseline experiments, such as MINOS (Adamson et al., 2011), T2K (Abe et al., 2017) and NOvA (Adamson et al., 2016), have provided the most precise measurements of these parameters. These experiments measured oscillations of neutrinos produced at accelerators. Fig. 1.9 shows the constraints on $\sin^2\theta_{23}$ and Δm^2_{32} from both atmospheric and accelerator neutrino experiments. Note that the figure below is the result of a very recent analysis. In the oscillation described in this thesis (Abe et al., 2017), the value for the two parameters are from an older Super-K result in (Abe et al., 2011b).

The mixing angle of θ_{13} was initially expected to be small since the solar and atmospheric neutrino results were consistent with the value of zero. In 2011, T2K first reported the indication of non-zero $\sin^2 2\theta_{23}$ via measuring electron neutrino appearance from muon neutrinos (Abe et al., 2011a). Shortly after the indication

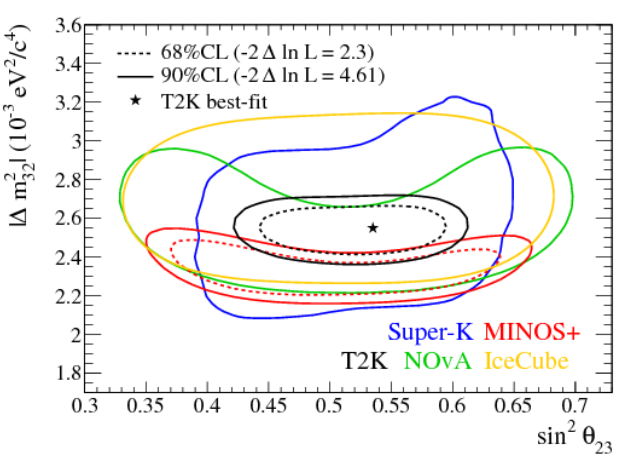

FIGURE 1.9: Allowed contours of $\sin^2\theta_{23}$ and $|\Delta m^2_{32}|$ assuming the normal hierarch from T2K, NOvA, MINOS+, Super-K, and IceCube. Taken from (Abe et al., 2017).

from T2K, several reactor experiments, such as Daya Bay (An et al., 2012), RENO (Ahn et al., 2012) and Double-Chooz (Abe et al., 2012b), measured the value of $\sin^2 2\theta_{13}$ precisely. These experiments measured the disappearance of $\bar{\nu}_e$ with one (or a set of detectors) near the reactor about a few hundred meters away and another (or a set of detectors) a couple of kilometers away. The effect of neutrino oscillations can be measured by comparing the observed neutrinos in the near and far detectors. Fig. 1.10 shows the layout of the Daya Bay experiment, and the measured $\sin^2 2\theta_{13}$ via observing $\bar{\nu}_e$ in their near and far detectors.

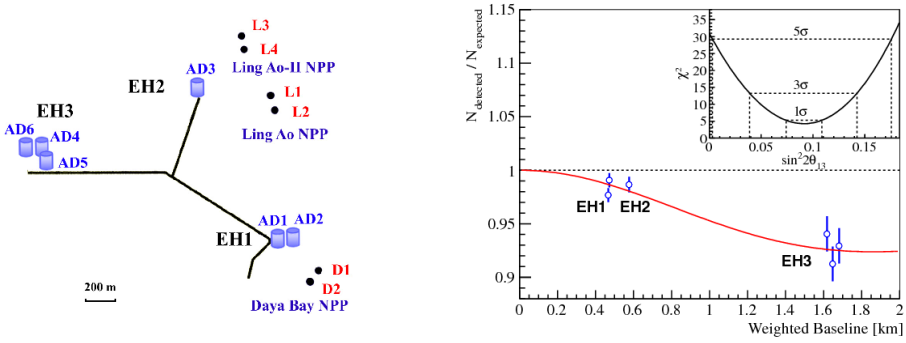

FIGURE 1.10: Left: Layout of the Daya Bay experiment. Right: Ratio of measured versus expected signal in each detector, assuming no oscillation. The oscillation survival probability at the best-fit value is given by the smooth curve. Taken from (An et al., 2012).

Recently, all these three experiments have updated their results with more data, making a more precise measurement of $\sin^2\theta_{13}$ as recorded in (Patrignani et al., 2016). In the analysis described in this thesis, the value for $\sin^2\theta_{13}$ comes from the an older global fit which are recorded in the 2012 PDG (Beringer et al., 2012).

The current best measured values of the oscillation parameters are summarized in Table 1.1.

Table 1.1: Oscillation parameter values as listed in (Patrignani et al., 2016). For Δm^2_{23}, the sign is unknown and the uncertainty is on the absolute value.

parameter	value
$\sin^2\theta_{12}$	0.304 ± 0.014
$\sin^2\theta_{13}$	0.0219 ± 0.0012
$\sin^2\theta_{23}$	0.51 ± 0.05
Δm^2_{21}	$(7.53\pm0.18)\times10^{-5}$ eV^2
Δm^2_{32}	0.00244 ± 0.00004 eV^2

1.4.6 Remaining Questions

Although most of the oscillation parameters have been measured, there are still important open questions to be answered in order to fully understand the nature of neutrinos.

First of all, it is not known whether θ_{23} mixing is exactly maximal (θ_{23}=45°). Current measurements of $\sin^2\theta_{23}$ are consistent with 0.5, but have a large uncertainty. If θ_{23} mixing is maximal, it could be a hint of some underlying symmetry (Xing and Zhao, 2016).

While the squared mass differences between the neutrino mass eigenstates have been measured, the sign of Δm^2_{32} (or Δm^2_{31}) has not yet been determined. In the normal hierarchy: $m_3 > m_2 > m_1$, while in the inverted hierarchy: $m_2 > m_1 > m_3$, as shown in Fig. 1.11. Due to this ambiguity, current experiments have to analyze their results under different assumptions of mass hierarchy. The true hierarchy also

has an important implication in the neutrino-less double beta decay experiments that search for a process involves simultaneous emission of two positrons but no neutrinos. If the mass hierarchy is inverted, the next generation of neutrino-less double beta decay experiments have a chance to detect a signal (Beringer et al., 2012).

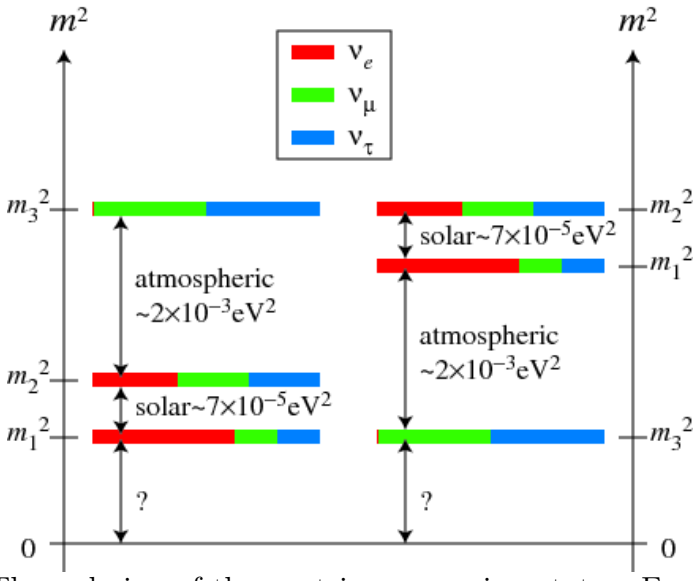

FIGURE 1.11: The ordering of the neutrino mass eigenstates. For the normal hierarchy, m_3 is the heaviest state and Δm^2_{32} >0, while for the inverted hierarchy m_3 is the lightest and Δm^2_{32} <0. Taken from (King and Luhn, 2013).

Another important question is whether CP is violated in neutrino oscillations. The value of δ_{CP} must be non-zero in order for CP violation in neutrino oscillations to happen. It can be probed by comparing the probabilities of the CP-conjugate oscillations, $P_{\nu_\mu \to \nu_e}$ and $P_{\bar{\nu}_\mu \to \bar{\nu}_e}$. If CP turns out to be violated in leptons, it is of importance for the understanding of the matter and anti-matter asymmetry in the universe (Dimopoulos and Susskind, 1978).

1.5 Outline of Thesis

This dissertation is organized as follows: a brief introduction of neutrino history and neutrino physics is presented in Chapter 1. Further discussion of tau neutrino

and the study of tau neutrino appearance are presented in Chapter 2. The experimental setup of Super-Kamiokande is described in Chapter 3. The simulation of neutrino events is described in Chapter 4. The event selection and reconstruction are presented in Chapter 5. A neural network algorithm for tau event identification is described in Chapter 6. The atmospheric tau neutrino appearance search is presented in Chapter 7. A measurement of charged-current tau neutrino cross section is presented in Chapter 8. Future application of the tau identification in three-flavor neutrino oscillation is discussed in Chapter 9. Finally, in Chapter 10, I summarize the tau neutrino analysis.

The work described in this dissertation is made possible with efforts from many Super-Kamiokande collaborators. The works done by Super-K collaborators are presented here to have a full description of the analysis. My contributions to the analysis are listed here: I was one of the data reduction experts in charge of the partially-contained reduction. I used the neural network to select tau events in datasets from SK-I through SK-IV, and developed a new method of search for tau neutrino appearance. I selected and optimized the input variables to the neutral network in the analysis. I carried out the analysis of the measurement of the charged-current tau neutrino cross section. I was a member of oscillation analysis group that developed the three-flavor oscillation analysis with tau neutrino identification.

2

The Tau Neutrino

The tau neutrino, together with the tau, forms the third generation of leptons. It was the last of the leptons in the Standard Model to be discovered. The tau neutrino is responsible for the deficit of muon neutrinos observed in Super-K because the tau neutrinos from muon neutrino flavor change are rarely observed in Super-K. In this chapter, I briefly discuss the status of study of the tau neutrino to better set the context for the analysis in this thesis.

2.1 Direct Observation of the Tau Neutrino

The tau neutrino was first directly observed in DONUT experiment in 2000, as mentioned in Section 1.1. DONUT was designed to search for charged-current (CC) tau neutrino interactions by identifying tau as the only lepton produced at the interaction vertex. Fig. 2.1 shows the experimental setup of the DONUT experiment.

The neutrinos were created by directing 800 GeV/c protons from the Fermilab Tevatron to a 1 meter tungsten target (Kodama et al., 2001). The dominant component in the neutrino beam is electron neutrino and muon neutrino from the decays

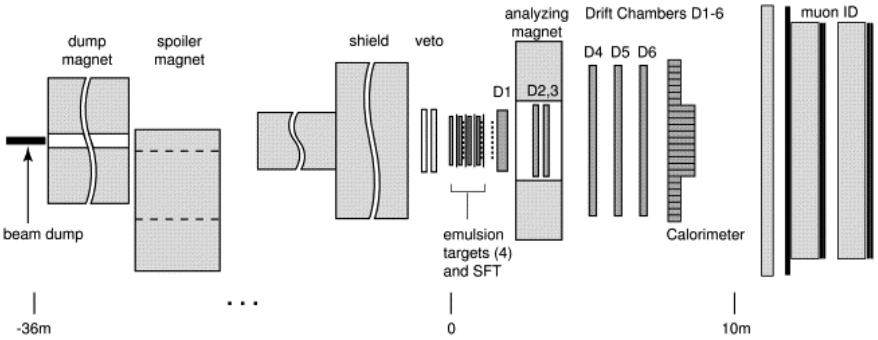

FIGURE 2.1: Schematic view the the experimental setup of DONUT experiment. Taken from (Kodama et al., 2001).

of charmed mesons in the beam dump. The tau neutrinos were primarily produced by the leptonic decays of a D_s meson into τ and $\bar{\nu}_\tau$, and subsequent decay of τ to ν_τ. The muons produced in the proton interactions in the beam dump were absorbed or swept away from the downstream detector using shielding and magnets.

The DONUT detectors consist of a scintillation counter veto wall, the hybrid emulsion target, trigger hodoscopes, and the charged particle spectrometer. The hybrid emulsion target was also used as a tracker which has a spatial resolution of $\sim$1 μm (Kodama et al., 2001). The good spatial resolution is important in the identification of tau at the interaction vertex because of its extremely short lifetime.

In total, DONUT observed 9 CC ν_τ events with an estimated background of 1.5 events based on 3.6×10^{17} protons on target (Kodama et al., 2008). Fig. 2.2 shows four CC ν_τ candidates in DONUT.

DONUT also measured the CC tau neutrino cross section based on the direct observation of CC ν_τ interactions. The total CC ν_τ cross section per nucleon is factored as

$$\sigma(E) = \sigma^{const} E K(E), \tag{2.1}$$

where $K(E)$ is the kinematic effect due to the tau lepton mass as shown in Fig. 2.3. The kinematics of $\nu_\tau n \rightarrow \tau^- p$ (or $\bar{\nu}_\tau p \rightarrow \tau^+ n$) requires that the minimum neutrino

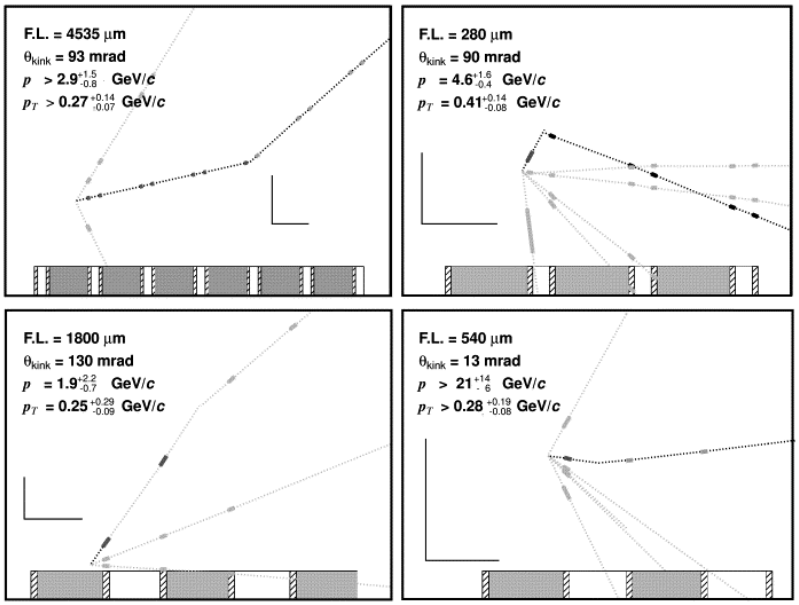

FIGURE 2.2: Four examples of ν_τ CC interaction events in DONUT. The neutrinos are incident from the left. Taken from (Kodama et al., 2001).

energy in the rest frame of the target nucleon is

$$E_{min} = m_\tau[1 + \frac{m_\tau}{2m_N}] = 3.5\text{GeV}. \tag{2.2}$$

The observed number of neutrino interactions can be written as

$$N_{int} = \epsilon_{TOT} N_\nu^{tgt} \frac{N_{nucl}}{area}\sigma, \tag{2.3}$$

where ϵ_{TOT} is the experimental efficiency for observing the interaction, N_ν^{tgt} is the number of neutrinos passing through the target area, N_{nucl} is the number of nucleons in the target area, and σ is the interaction cross section per nucleon.

Because DONUT can not distinguish ν_τ and $\bar{\nu}_\tau$, the measured CC cross section is actually an average of ν_τ and $\bar{\nu}_\tau$ cross sections. The flux of neutrinos was measured to be approximately equal to the flux of antineutrinos (Kodama et al., 2008). σ^{const} is measured to be $(0.39\pm0.13\pm0.13)\times10^{-38}\text{cm}^2$ GeV^{-1}. The first error is statistical, the second one is systematic. The measured cross section has a large statistical error

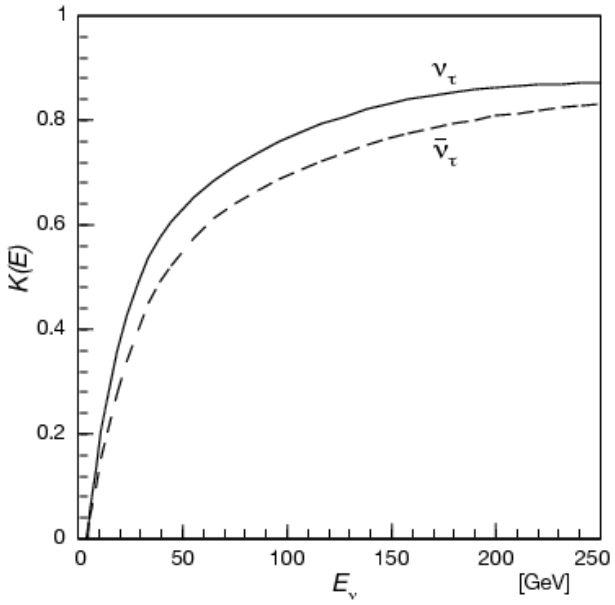

FIGURE 2.3: The suppression of CC tau neutrino cross section compared to CC $\nu_\mu/\bar{\nu}_\mu$ cross sections due to the tau lepton mass. Taken from (Kodama et al., 2008).

because DONUT only observed 9 neutrino interactions. The systematic error is also large because of the large uncertainty on the production and decay of D_s mesons.

2.2 Previous Search for Tau Neutrinos from Neutrino Oscillations

In three-flavor neutrino oscillations, $\nu_\mu \rightarrow \nu_\tau$ oscillation is the reason for the observed deficit of muons neutrinos in Super-K atmospheric neutrinos and long-baseline accelerator neutrinos. Because charged-current tau neutrino cross sections are suppressed by the kinematic effect of relatively large mass of the tau, tau neutrinos from neutrino oscillations interact more rarely than electron neutrinos or muon neutrinos in the detectors. The 3.5 GeV energy threshold is higher than the peak energy of neutrinos in long-baseline experiments that are tuned to maximal disappearance at their baseline. This results in the deficit of observed neutrinos in Super-K and long-baseline neutrino experiments. Additionally, the direct observation of tau neutrinos from neutrino oscillations has been challenging due to the difficulties of detecting and identifying

tau leptons. Nonetheless, Super-K and OPERA experiments have searched for tau neutrino appearance in atmospheric neutrinos and high-energy accelerator neutrinos respectively.

2.2.1 Previous Search for Tau Neutrino Appearance in Super-K

Atmospheric neutrinos have a wide range of energies as described in Section 1.3. This means that the higher energy tau neutrinos from neutrino oscillations have enough energy for charged-current interactions to occur. Super-K published a result of a search for atmospheric tau neutrino appearance based on SK-I data in 2006 (Abe et al., 2006), then updated the result based on SK-I-III data in 2013 (Abe et al., 2013).

Instead of exclusively reconstructing the track of tau at the neutrino interaction vertex, Super-K performed a search for hadronic decays of tau leptons. The decays typically produce multiple pions, which are not often seen in electron or muon neutrino events. The separation of tau events from electron or muon neutrino events was based on a likelihood method or a neural network algorithm. Fig. 2.4 shows the likelihood and neural network output distributions for data taken in SK-I. The events with likelihood > 0 or neural network output >0.5 are defined as tau-like.

The selected tau-like events were fitted with a combination of the expected tau appearance and atmospheric neutrino background in the zenith angle distribution.

$$N_{total}(\cos\theta) = \alpha N_{tau} + \beta N_{bkg}, \tag{2.4}$$

$$\chi^2 = \sum_{i=1}^{10} \frac{(N_i^{obs} - \alpha N_i^{tau} - \beta N_i^{bkg})^2}{\sigma_i^2}, \tag{2.5}$$

The best-fit value of tau normalization is 1.76 (1.71) for the likelihood method (neural network method), corresponding to $138\pm48(\text{stat})^{+15}_{-32}(\text{syst})$ observed tau events. The hypothesis of no-tau-appearance was excluded with a significance of 2.4σ. Fig. 2.5 shows the zenith angle distributions for tau-like events after fit.

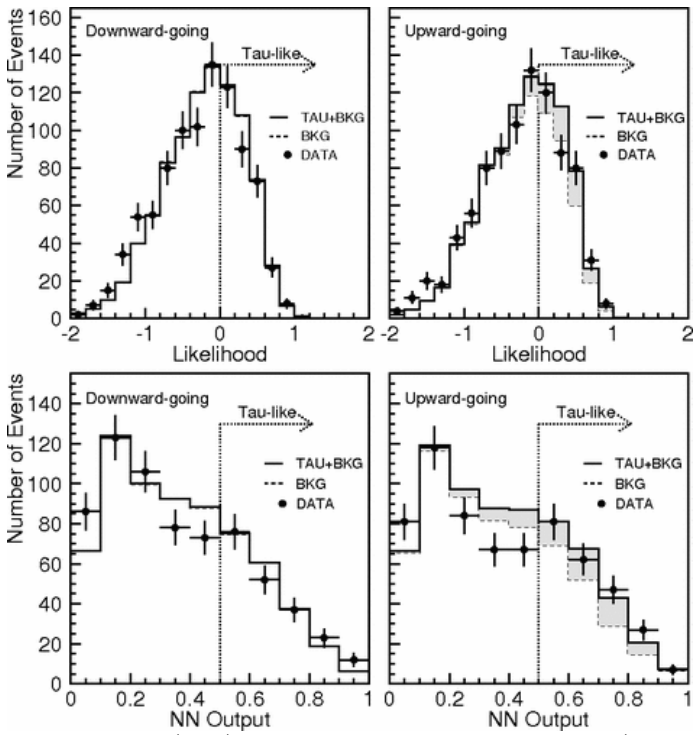

FIGURE 2.4: The likelihood (top) and neural network output (bottom) distributions of downward (left) and upward (right) events for data (dots), atmospheric neutrino background MC (dashed histogram), and tau and background MC (solid histogram). The events for likelihood > 0 and neural network >0.5 are defined as tau-like. Taken from (Abe et al., 2006).

In 2013, Super-K updated the result using improved neural network for tau separation and more data collected in SK-I through SK-III. Additionally, the data were fitted using an unbinned likelihood fit with a combination of the expected tau events and atmospheric neutrino background in two-dimensional distributions of neural network output and zenith angle. The tau normalization was fitted to be $1.42\pm0.35(\text{stat})^{+0.14}_{-0.12}$, corresponding to $180.1\pm44.3(\text{stat})^{+17.8}_{-15.2}(\text{syst})$ observed tau events. The significance of excluding no-tau-appearance was increased to 3.8σ.

2.2.2 OPERA

The OPERA experiment in the underground Gran Sasso Laboratory (LNGS) was designed to detect tau neutrino appearance using accelerator neutrinos. It used a

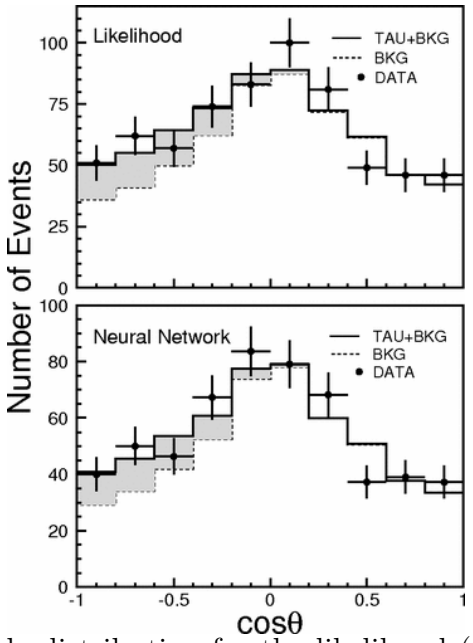

FIGURE 2.5: Zenith angle distribution for the likelihood (top) and neural network (bottom) methods. A fitted excess of tau-like events in the upward-going direction is shown in the shaded area. Taken from (Abe et al., 2006).

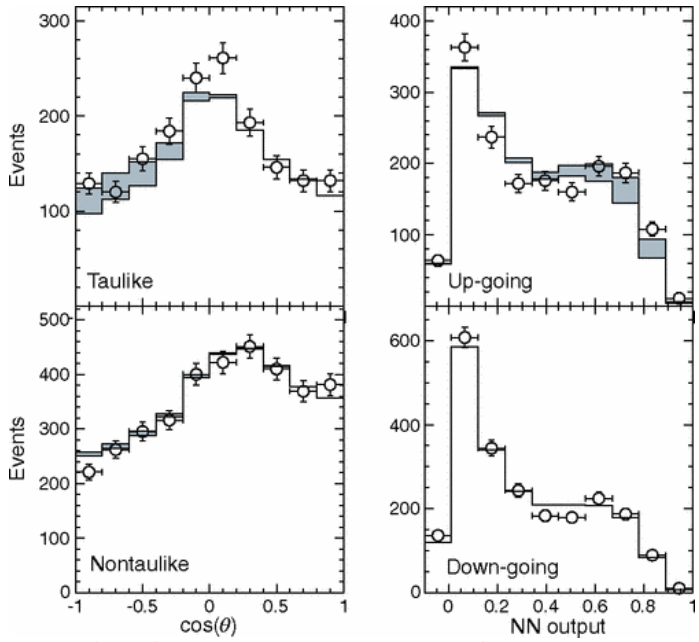

FIGURE 2.6: Fit results showing projections in the NN output and zenith angle distribution. The simulations and data sets have been combined from SK-I through SK-III. The fitted tau signal is shown in gray. Taken from (Abe et al., 2013).

emulsion target similar to that in the DONUT experiment to achieve precise reconstruction of the short track of tau. The detector was placed 730 km downstream the high energy long-baseline CERN to LNGS neutrino beam. Instead of using a neutrino beam containing tau neutrinos at production in DONUT, OPERA used a pure muon neutrino beam that contained almost no tau neutrinos at production. ν_τ appearance is expected after the ν_μ neutrinos travel 730 km to reach the detector. Fig. 2.7 shows a candidate ν_τ event observed in OPERA. At the end of the OPERA

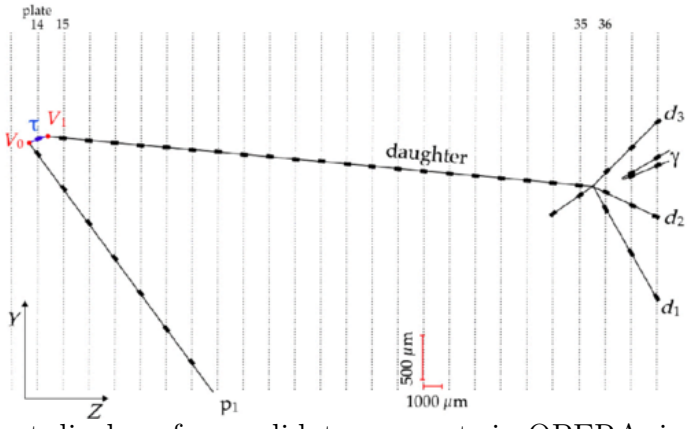

FIGURE 2.7: Event display of a candidate ν_τ events in OPERA, in which tau decay quickly into secondary particles after production. Taken from (Agafonova et al., 2015).

experiment, 5 ν_τ events were detected with an estimated background of 0.25±0.05, rejecting the background-only hypothesis at 5.1σ (Agafonova et al., 2015).

The studies of the tau neutrino and related neutrino oscillations have produced interesting results in the last two decades. However, the studies are still limited by the statistics because of the difficulties in both production and detection of tau neutrinos. The large target mass of Super-Kamiokande, coupling with the wide energy span of atmospheric neutrinos, offers a good opportunity to study the tau neutrino and related neutrino oscillations.

3

Super-Kamiokande

Super-Kamiokande (Super-K) is a large water Cherenkov detector in Japan. It is located in the Mozumi mine at a depth of 1,000 underground in Gifu, Japan. The main purpose of the experiment is to search for proton decays, as well as to study neutrinos from various natural sources, such as neutrinos from the Sun, atmosphere, supernovae, and other astrophysical sources. It was also used as the far detector in K2K experiment (Ahn et al., 2003) between 1999 and 2004. It has been playing the same role in T2K long-baseline neutrino experiment (Abe et al., 2011a) since 2009. Super-K started taking data in 1996, and has been running for more than 20 years. Datasets have been taken in four run periods defined by the detector configurations, SK-I (1996–2001), SK-II (2002–2005), SK-III (2006–2008) and SK–IV (2008-now). The configurations of each phase and detection methods are described here. More detailed information can be found in (Fukuda et al., 2003) and (Abe et al., 2014).

3.1 Cherenkov Radiation

Cherenkov radiation is electromagnetic radiation produced by a charged particle passing through a dielectric medium with a speed faster than the speed of light in that medium. The photons are emitted in a cone along the direction of the particle with an angle as

$$\cos\theta_c = \frac{1}{n\beta}, \tag{3.1}$$

where θ_c is the angle between the direction of Cherenkov light and the direction of the charged particle, n is the refractive index of the medium and β is the ratio of the velocity of the particle to the speed of light in the vacuum. A common analogy is the sonic boom of a supersonic object. The sound waves generated by the object cannot propagate forward from the object, instead forming a shock front. Fig. 3.1 illustrates the production of Cherenkov light and the direction of the light relative to the direction of charged particle. For the ultra-pure water of Super-K, n=1.33 at 580 nm, so that $1/n \approx 0.75$. In water, the energy threshold for Cherenkov radiation is 0.76 MeV for electrons and 158.7 MeV for muons. The number of photons generated per unit track length and per unit wavelength is given by the expression (Mead, 1958),

$$\frac{d^2N}{dxd\lambda} = \frac{2\pi\alpha}{\lambda^2}(1 - \frac{1}{n^2\beta^2}) \tag{3.2}$$

where α=1/137 is the fine structure constant, x is the track length, and λ is the wavelength of the photon. It corresponds to about 400 photons per cm at λ=300-550 nm.

3.2 Super-Kamiokande Detector

The Super-K detector consists of a large cylindrical water tank filled with 50,000 ton of ultra pure water. The tank has a diameter of 39.3 m and a height of 41.4 m.

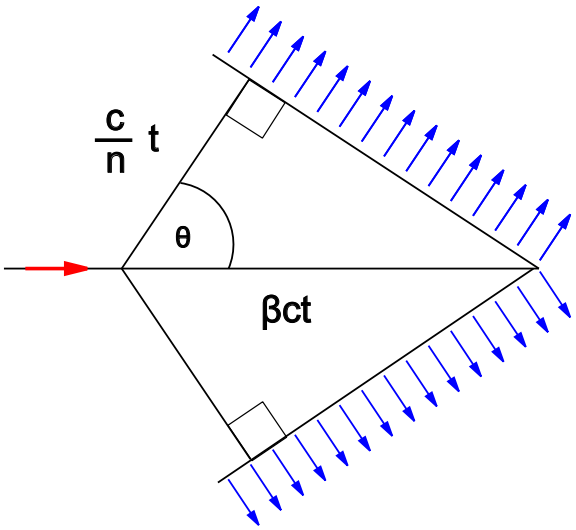

FIGURE 3.1: Schematic of the Cherenkov wavefront.

The detector is optically separated into two concentric cylindrical regions, the inner detector (ID) and the outer detector (OD). The OD is defined as the region extending 2.05 m inward the wall of the barrel, and 2.2 m from its top and bottom. A 55-cm thick stainless steel support structure, which is opaque to light, is installed between the ID and the OD. Photo-multipliers are mounted on both sides of the stainless steel structures to detect Cherenkov radiation produced by charged particles in water. The layout of the detector is shown in Fig. 3.2.

3.2.1 Inner Detector (ID)

The ID has a diameter of 33.8 m and a height of 36.2 m, and contains 32,000 tons of ultra-pure water. 20 inch inward-facing PMTs are installed uniformly on the inner surface of the ID. To prevent light leaks into the OD, the space between the PMTs is lined with black sheet. During the SK-I period, there were 11,146 PMTs, corresponding to about 40% of the ID surface covered by photocathode. An accident in 2001 caused by the implosion of PMTs damaged half of the PMTs, the remaining PMTs were rearranged uniformly in the reconstruction. For SK-II, the detector was run with 5,182 PMTs in the ID, corresponding to about 19% photocathode coverage.

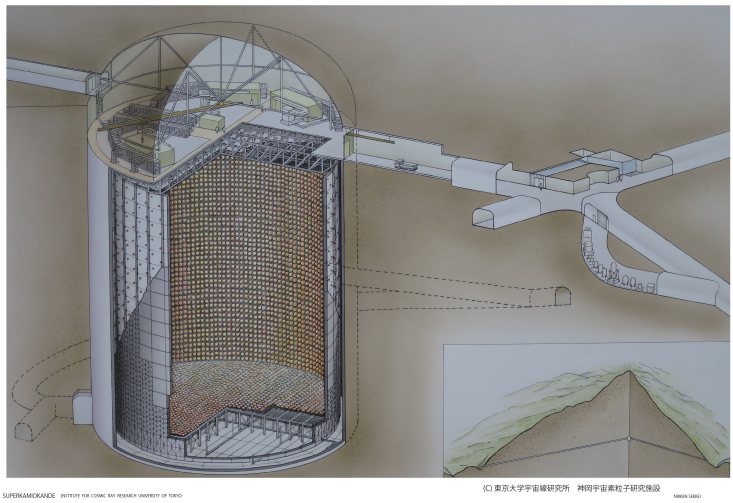

FIGURE 3.2: A sketch of Super-K detector, and the location of the detector under Mt. Ikenoyama.

A full reconstruction in 2006 restored the detector with full photocathode coverage of 40% in the ID, with 11129 PMTs in the ID after the restoration. The period between 2006 and 2008 is known as SK-III. An upgrade of electronics in 2008 marks the start of the SK-IV period.

3.2.2 Outer Detector (OD)

The OD is viewed by 8-inch outward-facing PMTs installed on the OD side of the stainless steel support structure. In all four SK periods, there are 1885 PMTs in the OD. In order to improve the light detection efficiency, the inner surface of the tank and the space between PMTs on the support structure is covered by reflective Tyvek®. Tyvek's reflectivity is ∼90% at the wavelength of 400 nm.

During the full reconstruction of the detector in 2005, Tyvek sheet was installed in the OD to separate the wall barrel region from the top region and the bottom region. Fig. 3.3 shows a schematic view of the OD segmentations.

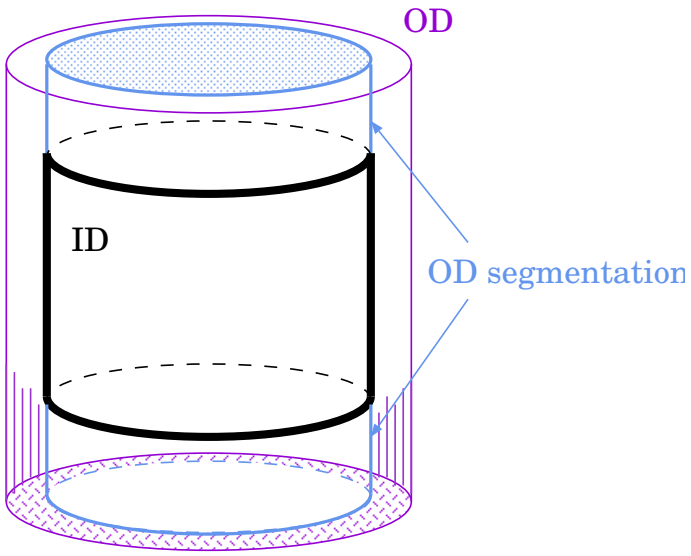

FIGURE 3.3: Schematic view of the Tyvek sheet installed in the OD that divides the OD into top, barrel and bottom regions.

3.3 Photomultiplier Tubes (PMT)

A photomultiplier tube (PMT) is a kind of sensitive detector of ultraviolet, visible and near-infrared ranges of light. An incident photon produces a photo-electron on the photocathode, and the signal current is amplified by multiple dynodes. The PMT enables the detection of single photons when the incident flux of light is very low. It has the advantages of high gain, low noise, ultra-fast response and a large area of collection.

The ID uses a 20-inch diameter Hamamatsu R3600 PMT (Fig. 3.4), developed by Hamamatsu Photonics K.K. in cooperation with Kamiokande collaborators (Kume et al., 1983). The dynode structure and bleeder circuit were modified to improve timing response and collection efficiency for Super-K (Suzuki et al., 1993). The photocathode of the PMT is coated with bi-alkali (Sb-K-Cs) that has high sensitivity to Cherenkov light and low thermal emission. A peak quantum efficiency (22%) is found in the region of 360–400 nm wavelength, that also corresponds to the peak of the relative Cherenkov spectrum in pure water as shown in Fig. 3.5. The gain of the

ID PMT is 10^7 at a high voltage of 1500 V to 2000 V. Fig. 3.6 shows the pulse height distribution for a single p.e in the ID PMT. Additional specifications are listed in Table 3.1.

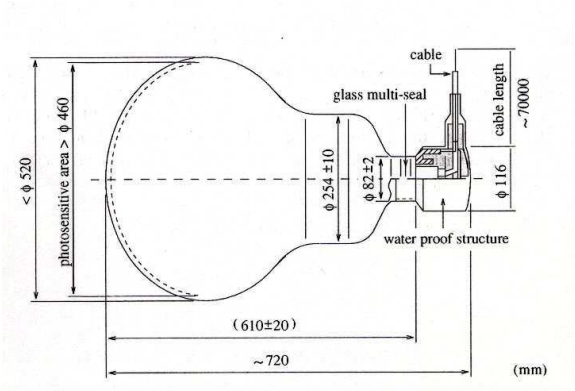

FIGURE 3.4: A schematic of the 20-inch PMT used in the ID. Taken from (Fukuda et al., 2003).

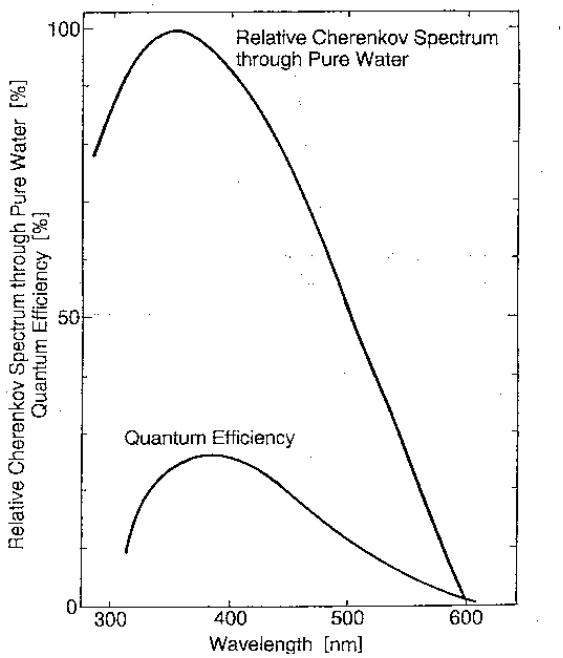

FIGURE 3.5: Quantum efficiency of the ID PMT, with relative spectrum of Cherenkov light in pure water overlaid. Taken from (Nishino, 2009).

The geomagnetic field at the Super-Kamiokande detector is about 450 mG, which affects photoelectron trajectories inside the PMTs. In order to compensate the field,

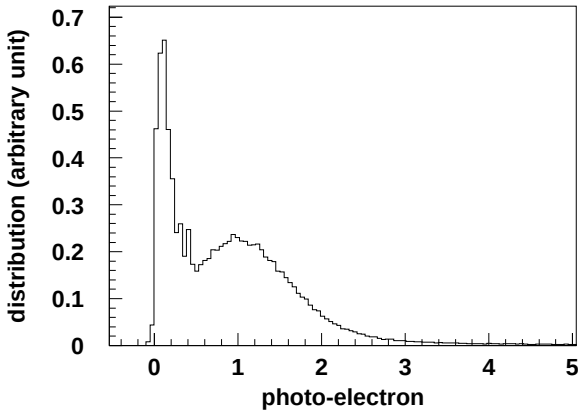

FIGURE 3.6: Pulse height distribution for a single p.e. in a 20-in PMT. The peak near zero is from dark current (Fukuda et al., 2003).

Table 3.1: Specification of the 20-inch PMT used in Super-Kamiokande.

Shape	Hemispherical
Photocathode area	50 cm diamater
Window material	Bialkali (Sb-K-Cs)
Quantum efficiency	22% at $\lambda = 390$ nm
Dynodes	11 stage Venetian blind type
Gain	10^7 at $\sim$ 2000 V
Dark current	200 nA at 10^7 gain
Dark pulse rate	3 kHz at 10^7 gain
Cathode non-uniformity	$< 10\%$
Anode non-uniformity	$< 40\%$
Transit time	90 nsec at 10^7 gain
Transit time spread	2.2 nsec (1 σ) for 1 p.e. equivalent signals
Weight	13 kg
Pressure tolerance	6 kg/cm^2 water proof

26 sets of horizontal and vertical Helmholtz coils are arranged around the inner surface of tank, reducing the magnetic field to $\approx$ 50 mG.

Following the accident in November 2001, the ID PMTs were instrumented with acrylic covers. A clear 12-mm thick UV-transparent acrylic dome is installed over the photocathode of each PMT, and the side of each PMT is protected with Fiber-Reinforced Plastic (FPR), with holes allowing water to flow freely. The transparency of the cover for photons with normal incident angle in water is $> 96\%$ above 350 nm

wavelength.

The OD uses 1885 8-inch PMTs. The photocathode of each PMT is covered by a 60 cm×60 cm×1.3 cm wavelength shifter plater (Becker-Szendy et al., 1993), which increases the light collection efficiency by 60%. The plates degrade the timing resolution of the OD PMTs from 13 ns to 15 ns. Since the OD is used as a veto for cosmic ray muons rather than a particle tracker, the light collection efficiency is more important than the timing resolution.

3.4 Electronics and Data Acquisition (DAQ)

The Super-Kamiokande electronics and data acquisition systems (DAQ) were designed to process signals from a large number of channels quickly and efficiently. The electronics and DAQ were upgraded in 2008, which marked the start of SK-IV. In this chapter, I briefly describe the features of the Super-K electronics and DAQ system.

3.4.1 Inner Detector Electronics and DAQ (SK I-III)

For the first three running periods, each of the ID PMT was connected to one of 12 input on custom analog timing modules (ATMs) for signal processing. The ATMs recorded integrated charge and arrival time of all ID PMTs. Each ATM was housed in a crate containing 20 ATMs, with a total of 48 crates evenly distributed among four electronics huts located above the detector tank.

Each input channel of the ATM has two switching channels containing both a Charge to Analog Converter (QAC) and a Time to Analog Converter (TAC), allowing one channel to be active while the other one is digitizing. This two channel setup minimizes dead time, in particular for events in which there may be two stages occurring in rapid succession. Detailed specifications of the ATM are shown in Table 3.2. Each ATM is set at a threshold of 0.23 p.e. equivalent. When a PMT is hit and

Table 3.2: Specifications of the ATM.

Number of channels	12/board
One hit processing time	∼5.5 μs
Charge dynamic range	∼400-600 pC (12-bit)
Timing dynamic range	∼1300 ns (12-bit)
Charge resolution (LSB)	0.2 pC
Charge resolution (RMS)	0.2 pC
Timing resolution (LSB)	∼0.3-0.4 ns
Timing resolution (LSB)	0.4 ns
Temperature dependence (QAC)	3 Count/deg. ↔0.6 pC/deg.
Temperature dependence (TAC)	2 Count/deg. ↔0.8 pC/deg.
Event number	8-bit
Data size of one hit	6 bytes
FIFO	2 kBytes (340 hits)

triggered, a 15 mV 200 ns wide square wave is issued to the ATM front panel and a 900 ns veto is placed on the channel to prevent after-pulsing hits. An analog sum of all such waves is known as the "HITSUM". A global trigger is issued at 29 PMT hits, corresponding to roughly 5 MeV of energy. On a global trigger, a stop signal is sent to TAC, then the information in the QAC and TAC is digitized by the ADC. The integrated charge and time information from all ATM channels is stored along with the event number information distributed by GONG (Go/No-Go) modules. Other header information is sent to Super Memory Partner boards (SMP). Data stored in the SMPs are later read out by online computers via Versa Module Europa (VME). More details of the DAQ process can be found in (Fukuda et al., 2003).

3.4.2 Outer Detector Electronics and DAQ (SK I-III)

The paddle cards are used to distribute high-voltage to the OD PMTs. Each paddle card is connected to 12 PMTs via coaxial cables and is itself powered by a LeCroy 1454 mainframe. The coaxial cable is used to supply high-voltage and transmit analog signals from the PMTs. The signals are then sent to charge-to-time conversion (QTC) modules that convert the PMT signal to a rectangular pulse with a width

proportional to the input charge. This pulse is generated along with a 25 mV high 200 ns wide analog signal used to create an OD "hitsum" when a PMT exceeds a 0.25 p.e. threshold in a 200 ns wide time window. When a global trigger is issued, the logical pulse from the QTC is fed to a time-to-digital converter (TDC) which is read out across all OD channels. OD data are stored 10 μs before and 6 μs after the trigger and are read out via VME to online computers for analysis.

3.4.3 Triggering (SK I-III)

Three types of Super-K triggers are implemented based on the number of hit PMTs (HITSUM) in the ID within a 200 ns time window, corresponding roughly to separate physics analyses of interest. The high energy (HE) trigger is issued when HITSUM exceeds 31 hits and fires at a rate of $\sim$5 Hz. The low energy (LE) trigger corresponds to 29 hits and has a rate of $\sim$11 Hz. Finally, the super low energy (SLE) trigger was implemented about a year into SK-I period to lower the solar neutrino analysis threshold. The OD trigger system works similarly, with a trigger threshold of 19 hits within a 200 ns time window. When a trigger is issued, it is sent to a hardware trigger module TRG that signals the readout of the PMT channels.

3.4.4 SK IV Electronics and DAQ Upgrade

In order to reduce dead time, the Super-K front-end electronics and DAQ system were upgraded in 2008 (Yamada et al., 2010; Nishino et al., 2009). Here, I briefly describe the upgrade.

The new front-end electronics are QTC-Based Electronics with Ethernet (QBEE). One QBEE board is equipped with eight QTC chips, and each QTC chip has three input channels. The QTC has three gain ranges (small, medium, large) for PMT readout that covers a wider dynamic range (0.2 - 2500 pC) than the ATMs. The timing and charge resolution are similar to those of the ATMs. The QTC outputs

a pulse whose leading edge contains the timing information and whose width is proportional to the total charge. The ethernet cables improves data flow relative to the old TKO readout.

Instead of hardware triggers in SK-I-III, a software trigger is implemented in SK-IV that contains all PMT hit information. The software trigger makes selections based on the same hit threshold described above for SK-I-III trigger system.

3.5 Background Reduction

3.5.1 Water Purification

Since the light collected by the PMTs has to travel through the water, it is important to keep the water as pure as possible. Water taken from the mine is first passed through a 1 μm filter to remove large particles. It is then passed through a heat exchanger that cools the water to about 13 °C to limit the growth of bacteria. Following this, a cartridge polisher removes heavy ions, and a UV sterilizer kills the remaining bacteria. The water then goes through a reverse osmosis and vacuum degassifier system that removes radon and other dissolved gas. In the final stage ultra filters remove particles larger than ∼10 nm in diameter. The water is then returned to the tank. Water in the tank circulates through the system at about 60 tons/hour.

3.5.2 Air Purification System

The air in the mine housing Super-K detector has a high concentration (10–5000 Bq/m^3) of radon. To limit the amount of this background entering Super-K, fresh air is continuously pumped into the control room and cavern area of the experiment. Radon concentrations are kept around 20-30 Bq/m^3 inside the top of the Super-K tank and below 100 Bq/m^3 at the cavern.

3.6 Calibration

3.6.1 PMT Calibration

Absolute gain

For the absolute gain, the single p.e. distribution must be measured in order to convert the charge measured by the PMTs to the number of p.e.s. The calibration uses a ^{252}Cf source surrounded by a spherical mixture of nickel oxide and polyethylene. Spontaneous fission of the ^{252}Cf produces neutrons that are brought to thermal equilibrium by the polyethylene, and then captured by the nickel. The neutron captured by nucleus isotropically emits ∼9 MeV gamma rays. The nickel source is deployed at the center of the tank, and generates about 100 photons per capture. Therefore, most hit PMTs will have only a single p.e. The mean value of the 1 p.e. charge distribution is taken as a constant to convert charge measured by PMTs to the number of p.e.s, as shown in Fig. 3.7. The constants in SK-I through SK-IV are 2.044 pC/p.e., 2.297 pC/p.e., 2.243 pC/p.e., and 2.658 pC/p.e. respectively.

Relative PMT gain

The high voltage of each PMT is set so that all PMT gains are approximately the same. The relative gain describes the response of each PMT relative to the average. Fig. 3.8 shows a schematic view of the relative gain calibration system. Light from a Xe lamp is passed through an ultraviolet filter and injected into a scintillator ball lowered into the tank. The scintillator ball absorbs the remaining UV light and re-emits photons with wavelength of 440 nm uniformly. The intensity of the Xe light is monitored by two photodiodes and a 2-inch PMT that also serves as a calibration trigger. PMT high voltages are adjusted so that the charge measured in each tube after corrections for light attenuation, acceptance and shape of the scintillation ball agree between all of the PMTs. This measurement is performed at various positions of the ball within the tank. The relative gains distribution had width of 7.0% at the

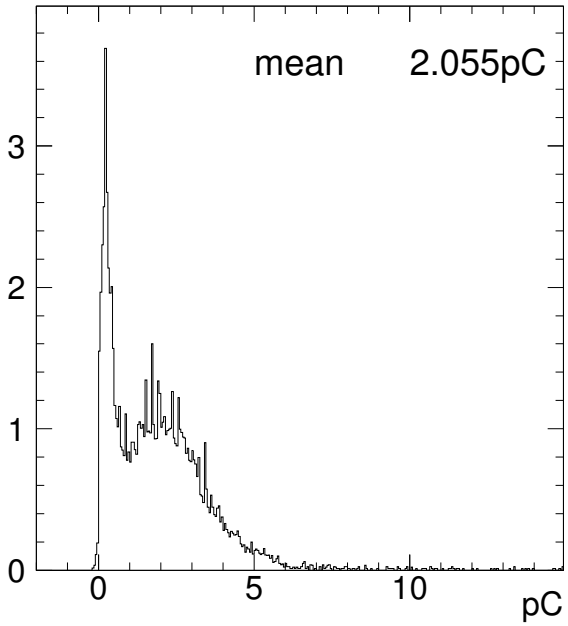

FIGURE 3.7: Single photoelectron distribution of a typical ID PMT. The bump at about 2.0 pC corresponds to on p.e.. Taken from (Fukuda et al., 2003)

beginning of SK-I.

Relative timing calibration

The hit timing of PMTs varies across the detector due to several factors. Since the Super-K tank is very large, the timing difference arises from different PMT cable lengths. Similarly, the timing is a function of the amount of charge collected by a PMT because larger hits exceed TDC threshold earlier due to slewing in the discriminators. Therefore, each PMT's timing response is measured as a function of charge and stored as a look-up table called the time-charge (TQ) map. TQ maps are measured with the apparatus in Fig. 3.9. Light from a N_2 laser is split into two beams, one sent to a diffuser ball deployed in the tank and the other to a reference PMT. The laser produces a 3 ns wide pulse of 384 nm light. The intensity of the light is varied with an optical fiber in order to measure the timing at different pulse

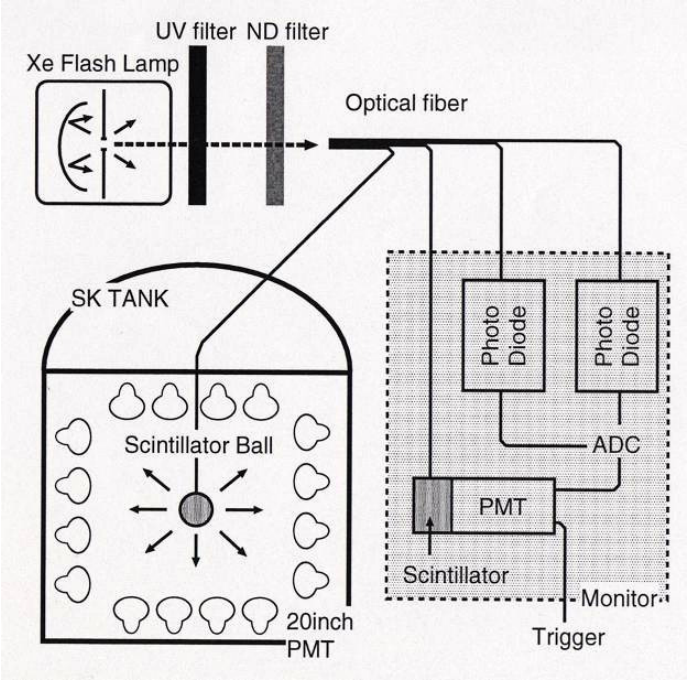

FIGURE 3.8: Schematic view of the relative gain measurement system. Taken from (Lee, 2012)

heights. A TiO_2 tip at the center of the diffuser ball works in conjunction with a silica gel to diffuse light without smearing its time profile. A typical TQ map is shown in Fig 3.10.

QBEE charge linearity

For the QBEE modules in SK-IV, a dedicated calibration run is taken to measure the linearity of the readout system. The measurement covers a wide range of light intensity, all the way into saturation. Ten ID PMTs, that are read out with well-understood, high-resolution CAMAC ADC, are selected as reference in the measurement. The laser system mentioned in the relative timing calibration is used to inject laser of thirty different intensities into the tank. The relative intensities of these 30 sets of different-intensity laser shots were established by the reference PMTs. The intensity scale for each ID PMT is fixed by the chosen intensity for which its

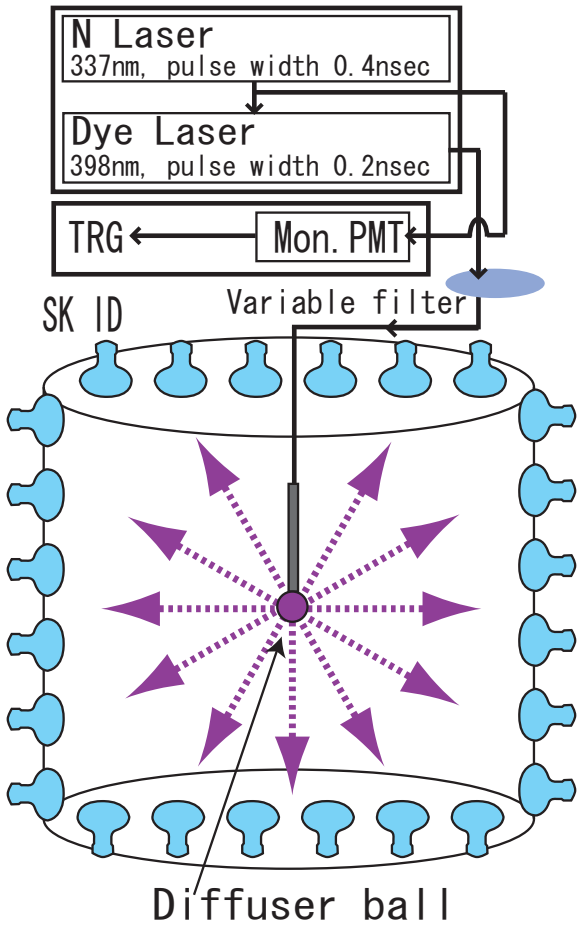

FIGURE 3.9: Schematic view of the relative timing measurement using a laser. Taken from (Ishihara, 2010).

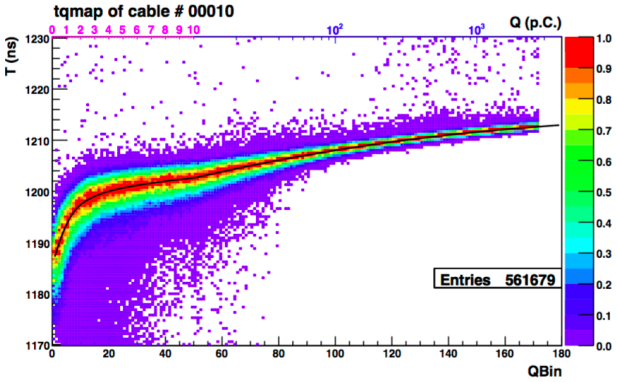

FIGURE 3.10: A characteristic TQ map for an ID PMT (Abe et al., 2014).

observed charge is closest to 30 p.e.s. Using the relative intensities derived from the ten reference PMTs, we can calculate the expected charge for each of the other 29 laser intensities. The charge linearity is measured as the ratio of observed charge to expected charge. Fig. 3.11 shows the result of the linearity measurement. The response of the ID PMTs is linear within 1% with less than 200 p.e.s, and increases to more than 10% at above 1000 p.e.s. This non-linearity is taken into account in the MC simulations.

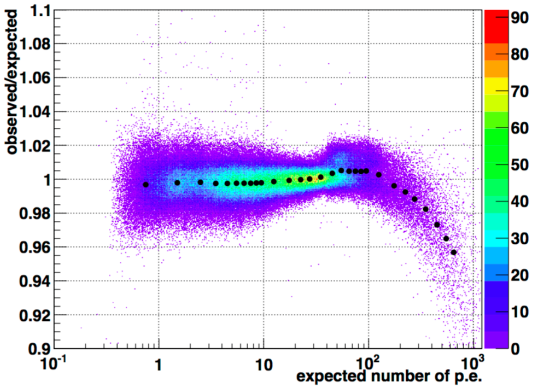

FIGURE 3.11: Charge linearity of all ID PMTs. The points shows the average for each expected number of photoelectrons region. Taken from (Abe et al., 2014).

3.6.2 Water Calibration

Measurement of light scattering and absorption in water with a laser

The attenuation of light during travel in the water depends on the water transparency. Water transparency is affected by absorption and scattering of light. The relevant scattering processes in SK are Rayleigh and Mie scattering. The attenuation length in water can be described by three parameters:

$$L_{atten}(\lambda) = \frac{1}{\alpha_{Ray}(\lambda) + \alpha_{Mie}(\lambda) + \alpha_{abs}(\lambda)}. \tag{3.3}$$

These three parameters are measured with a laser system that injects light tuned to different wavelengths via an optical fiber into the tank from eight different positions.

The charge and timing information from the laser light measurement was used to tune the water parameters in Monte Carlo simulations (MC) until good agreement between data and MC was found. The measured parameters are shown in Fig. 3.12

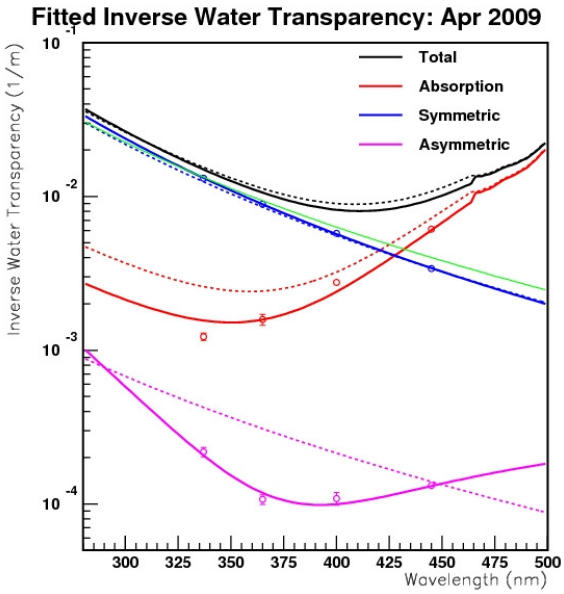

FIGURE 3.12: Typical fitted water coefficient functions used in the SK-MC. The points are the data obtained in April 2009. Taken from (Abe et al., 2014).

Water transparency measurement with cosmic ray muons

Cosmic ray muons passing through the detector at a rate of a few Hz, making up the bulk of high energy events. Muons below 100 GeV deposit energy via ionization at a rate of about 2 MeV/cm. Therefore, they are a natural calibration source and cover a much wider energy range than the laser sources described above. Only vertical muons are selected in this measurement. The muon track is reconstructed by connecting the entrance and exit points in the ID. Assuming the light is not scattered, the number of photoelectrons detected in a cosmic ray muon event is expressed by:

$$Q(l) = Q_0 \frac{f(\theta)}{l} e^{-l/L_{atten}} \tag{3.4}$$

where Q_0 is a constant, $f(\theta)$ is the PMT angular acceptance with θ as the angle respect to the normal, l is the photon path length, and L_{atten} is the attenuation length. The water attenuation length is measured continuously with comic ray muons. Fig. 3.13 shows the measurements of Equation 3.4 and time variation of the attenuation length.

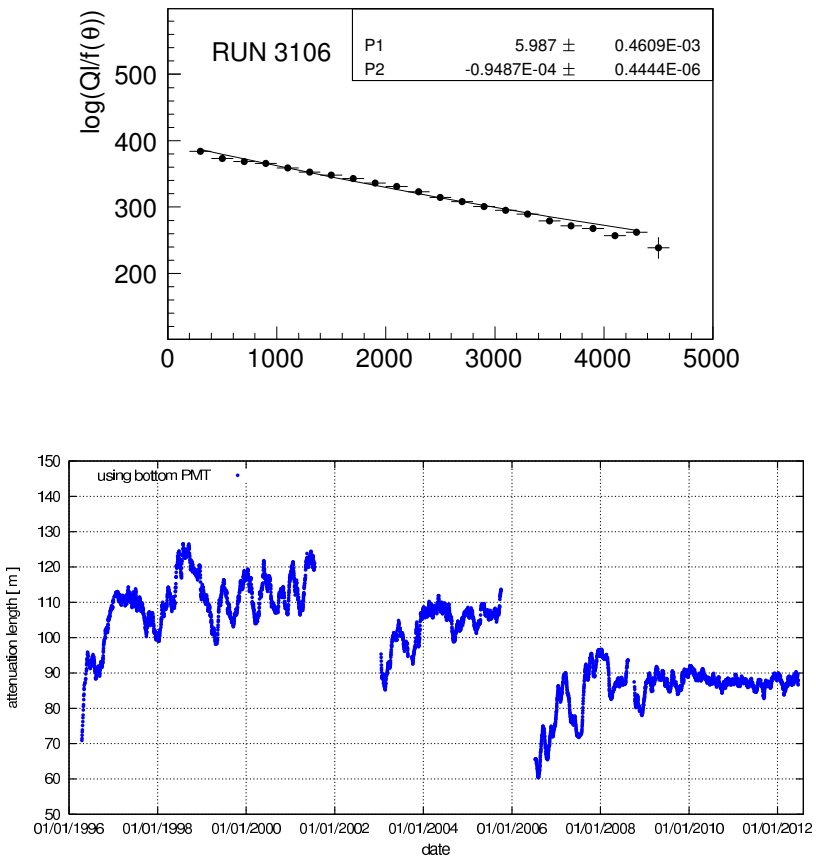

FIGURE 3.13: Effective observed charge for through-going muons as a function of photon pathlengths (l), where Q is the detected charge and $f(\theta)$ is the PMT acceptance (top).Time variation of water attenuation lengths for SK-I, SK-II, SK-III and SK-IV (bottom). Taken from (Abe et al., 2014).

3.6.3 Energy Scale

Precise knowledge of the detector energy scale is important for energy reconstruction. Four independent sources are used to calibrate the energy scale in momentum range

from a few tens of MeV/c to about 10 GeV/c.

Track length of high energy stopping muons

Momentum of high energy muons is approximately proportional to their track lengths. Muons entering from the top and stopping inside the detector are selected for calibration. The track length is reconstructed by connecting the entering point and the vertex position of the subsequent decay electron. Resolutions of stopping muon entering position and decay electron vertices are better than 50 cm. The accuracy of the absolute energy scale is checked by comparing calibration data with Monte Carlo simulations. The agreement between data and MC is within 0.7%, 1.1%, 2.0% and 2.2% for SK-I, SK-II, SK-III, and SK-IV respectively.

Low energy stopping muons

The Cherenkov angles of low energy muons are used for low momentum ($<$ 400 MeV/c) calibration. As shown in Equation 3.1, the angle of the emitted Cherenkov photons relative to the charged particle is a function of the particle's energy. By measuring the Cherenkov angle of stopping muons, their momentum can be determined as:

$$p = \frac{m}{\sqrt{(n\cos\theta)^2 - 1}}. \tag{3.5}$$

where n is the refraction index of water, m is the mass of muon, and p is the muon momentum. The Cherenkov angle reaches a limiting value for high momenta, so only muons with momentum less than 400 MeV/c are used. Fig. 3.14 shows the averaged $P_{p.e.}/P_\theta$ and the double ratio of MC to data as a function of P_θ. The agreement is within 0.7%, 1.3%, 2.1% and 2.1% for SK-I, SK-II, SK-III and SK-IV respectively.

Neutrino induced π^0

Neutral pions are produced by neutral-current interactions of atmospheric neutrinos in the detector, which then decay into two photons. The invariant mass of π^0

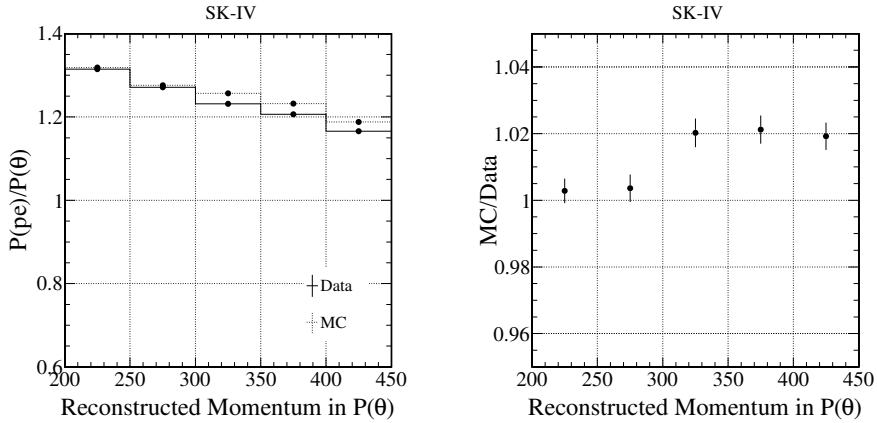

FIGURE 3.14: The averaged $P_{p.e.}/P_\theta$ where P_θ is the momentum reconstructed with θ_C for SK-IV data (solid) and MC (dashed) (left), and the double ratio between MC and data (right). Taken from (Lee, 2012).

can be reconstructed by combining momentum of two photons. The distribution of the invariant mass is centered around 135 MeV as shown in Fig. 3.15. A Gaussian fit of the data and MC found that the agreement between data and MC is within 0.7%, 1.3%, 0.3% and 1.7% for SK-I, SK-II, SK-III and SK-IV respectively.

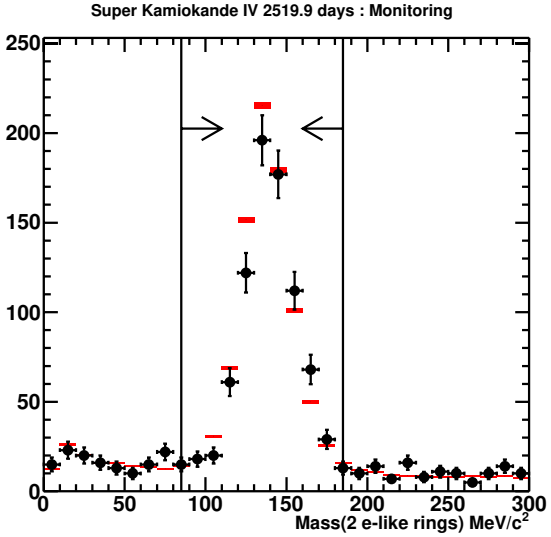

FIGURE 3.15: Invariant mass distribution of neutrino-induced π^0 events for data (dot) and MC (boxes). MC is normalized to the live time of data.

Decay electrons

Decay electrons from decay of stopping muons are abundant and their energy spectrum is useful for energy calibration in the tens of MeV region. Muons are susceptible to muon capture by a nucleon, in which no electrons are produced. These stopping muons are rejected in the search for decay electrons. Specific selection criteria for decay electrons will be described in Section 5.2. Fig. 3.16 shows the momentum distribution of decay electrons in data and MC.

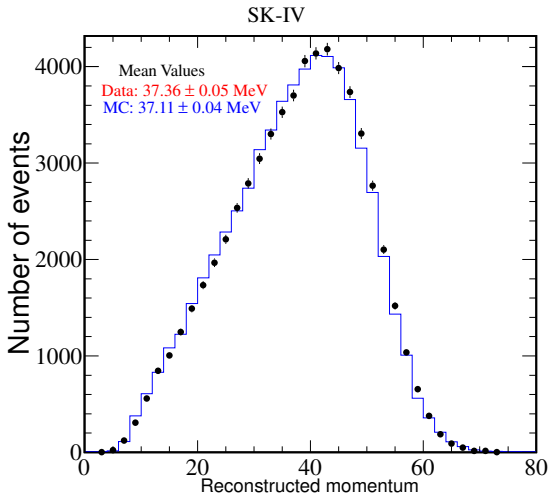

FIGURE 3.16: Momentum of decay electrons for data (crosses) and MC (solid histogram). Taken from (Abe et al., 2014).

Summary of energy scale

Fig. 3.17 shows the energy scale uncertainty as a function of momentum for the calibration sources described above. The uncertainty is within 3% for all samples considered.

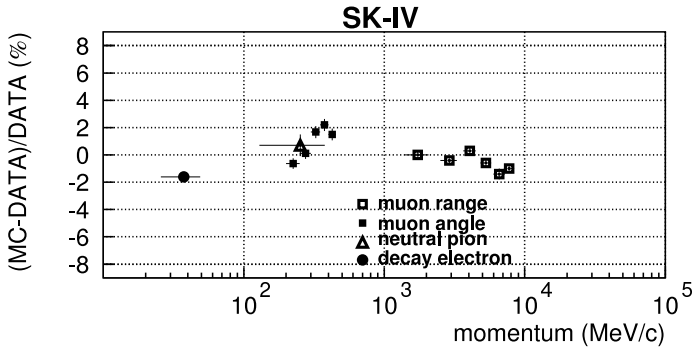

FIGURE 3.17: Energy scale uncertainty as a function of momentum for calibration measurements in SK-IV, decay electrons (solid circle), single π^0 (solid triangles), low-energy stopping muon (open squares) and high-energy stopping muons (solid squares). Taken from (Ishihara, 2010).

4

Atmospheric Neutrino Simulations

Monte Carlo (MC) simulation is essential for the Super-K atmospheric neutrino analysis. The neutrino interactions in the detector are simulated, then compared with the collected data samples. The MC simulation of atmospheric neutrinos in Super-K is done in stages - modeling the interactions of neutrinos in the water, subsequent particle tracking inside the detector volume and the detector's response to these particles. Each of these stages are described here.

4.1 Atmospheric Neutrino Flux

The analyses of atmospheric neutrinos are essentially done by investigating the change of the observed neutrino flux at the detector relative to the expectation. Therefore, it is important to have an accurate model of atmospheric neutrino production. The Honda flux calculation (Honda et al., 2015) is adopted to model the atmospheric neutrino flux at Super-K. It is fully three-dimensional and tracks every necessary particle from its generation to interaction within the atmosphere. The model takes into account the primary cosmic ray spectra, the hadronic interactions

in the atmosphere and the effects of the geomagnetic field in the calculation. The model is briefly described below.

The primary cosmic rays consist of mostly proton and helium nuclei. The primary cosmic ray flux, which is the input to the neutrino flux calculation, is based on experimental measurements by AMS (Alcaraz et al., 2000) and BESS (Sanuki et al., 2000; Haino et al., 2004). The effect of the magnetic field from the solar wind is prominent at low cosmic ray momenta ($\sim$ 1GeV/c), which is included in the calculation. Fig. 4.1 shows the primary cosmic ray flux in the Honda model.

The US standard atmospheric model (NOAA and Force, 1976) is used as the model for the density structure of the atmosphere. Geomagnetic field induces a up-down and east-west asymmetry of the neutrino flux as well as a low-energy cutoff in the flux due to the deflection of low energy primary cosmic rays. Its effects are calculated based on the IGRF2005 model (Thébault et al., 2015).

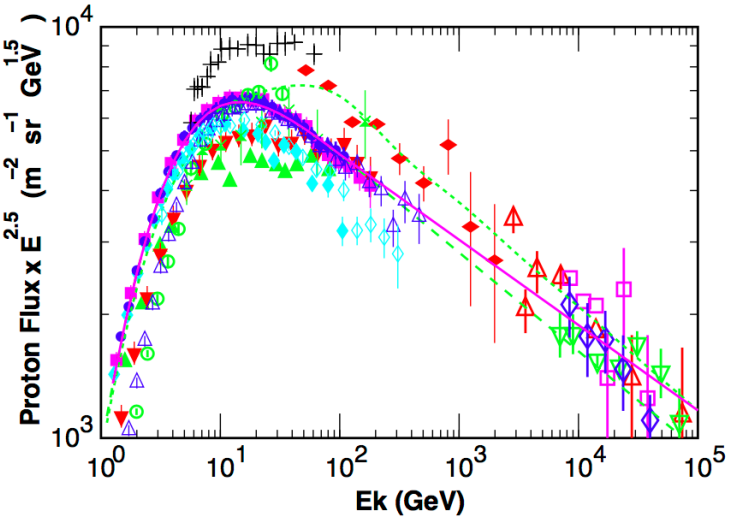

FIGURE 4.1: The primary cosmic ray protons at solar minimum as calculated in (Honda et al., 2004). Overlaid data points (see (Honda et al., 2004) for references) are taken from Webber (crosses), LEAP (upward triangles), MASS1 (open circles), CAPRICE (vertical diamonds), IMAX (downward triangles), BESS98 (circles), AMS (squares), Ryan (horizontal diamonds), JACEE (downward open triangles), Ivanenko (upward open triangles), Kawamura (open squares) and Runjob (open diamonds).

For the production of secondary particles in the atmosphere, DPMJET-III (Roesler et al., 2000) is used for hadronic interactions above 32 GeV while JAM (Niita et al., 2006) is used for energy below 32 GeV due to its better agreement with low energy cosmic muon data. The hadronic interaction simulations are fine tuned to match the simulated cosmic ray muons with experimental measurements from (Motoki et al., 2003; Achard et al., 2004; Haino et al., 2004; Sanuki et al., 2002).

Fig. 4.2 shows the zenith angle distributions of neutrino flux for three different neutrino energies simulated with Honda model. The distribution is peaked at the horizontal because the cosmic ray particles can travel longer distances in the atmosphere horizontally and have more time for decay. The large up-down asymmetry in the left plot is due to the geomagnetic field.

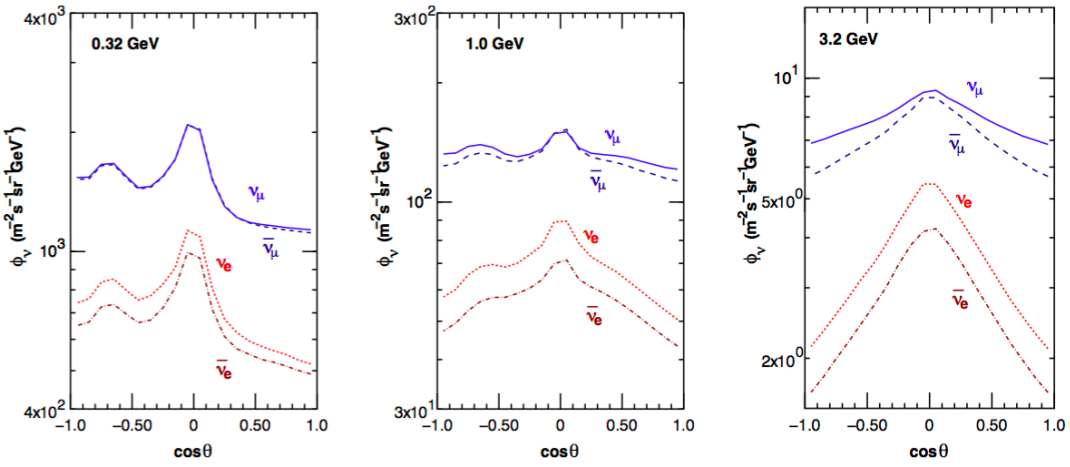

FIGURE 4.2: Zenith angle dependence of atmospheric neutrino flux at Super-K averaged over the azimuthal at 0.32 GeV (left), 1.0 GeV (middle) and 3.2 GeV (right). $\cos\theta$=1 represents vertically downward going and $\cos\theta$=-1 represents vertically upward going neutrinos. Taken from (Honda et al., 2015).

Fig. 4.3 shows the direction-averaged neutrino flux as a function of neutrino energy at Super-K. The plots compare the flux predictions from Honda model with other models such as the Fluka model (Honda et al., 2015) and the Bartol model (Honda et al., 2015). The differences in the flux predictions between Honda model

and other models are used to estimate the systematic uncertainties on the atmospheric neutrino flux.

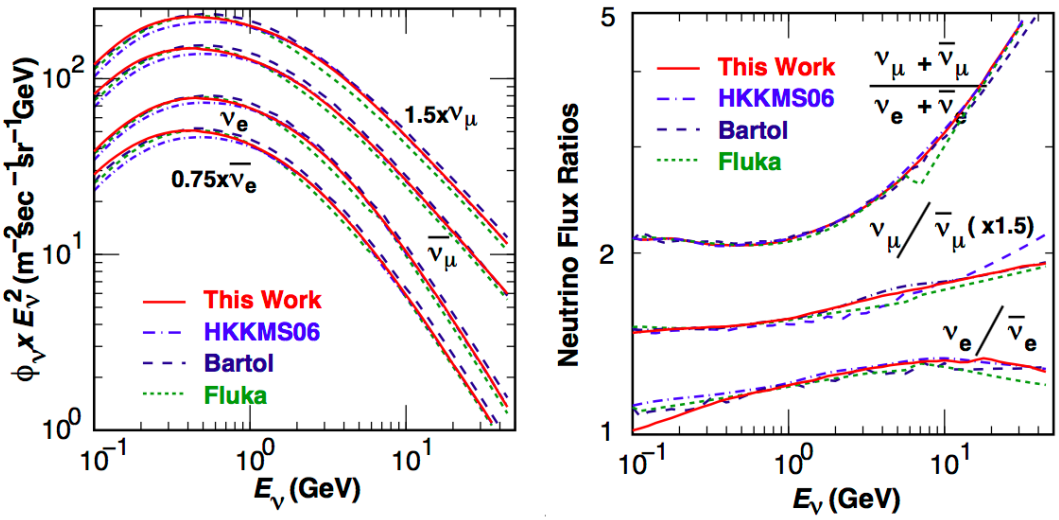

FIGURE 4.3: The direction-averaged atmospheric neutrino flux at Super-K as a function of neutrino energy. The left plot is absolute flux and the right plot is the flux ratios. Honda flux model is shown in red. Other model predictions are compared with Honda model to estimate the systematic uncertainties on the flux. Taken from (Honda et al., 2015).

The MC events are generated using the predicted flux at Super-K assuming all neutrinos reach the detector as their original flavor at the production in the atmosphere. Oscillations are applied by reweighting each MC event at the time of performing an analysis according to its oscillation probability given the neutrino energy and direction.

4.2 Simulation of Neutrino Interactions

Atmospheric neutrinos are detected when they interact with water in the tank or the rock surrounding the Super-K detector. Neutrino interactions at Super-K are simulated by the neutrino event generator NEUT (Hayato, 2009). The software simulates the neutrino interactions with nuclei in water and rock. The interactions with atomic electrons are neglected due to the three orders of magnitude smaller

cross section relative to that for nuclei at typical atmospheric neutrino energies. The volumes simulated include the rock surrounding the Super-K detector, the OD and the ID regions.

Neutrino interactions can classified into charged-current and neutral-current interactions based on which bosons take part in the interaction. A neutrino interacts with other particles by exchanging a $W^{\pm}$ boson in a CC interaction in which a charged lepton of the same flavor as the neutrino is produced. The flavor of a neutrino can be determined by detecting the charged lepton produced in its CC interactions. On the other hand, a NC interaction is mediated by a Z^0 boson which does not leave any signal of the neutrino flavor in the detector.

Five main modes are simulated:

- quasi-elastic scattering: $\nu + N \rightarrow l + N'$
- meson exchange current: $\nu + NN^* \rightarrow l + N'N'^*$
- single meson production: $\nu + N \rightarrow l + N' + m$
- coherent pion production: $\nu +^{16} O \rightarrow l +^{16} O + \pi$
- deep inelastic scattering: $\nu + N \rightarrow l + N' + hardons$

where ν is a neutrino or anti-neutrino of any flavor, N/N^* and N'/N'^* are the incoming and outgoing nucleons respectively, and l is the outgoing lepton. All modes except meson exchange current can occur in CC and NC types. The interactions are described below.

4.2.1 Quasi-elastic Scattering

Charged-current quasi-elastic scattering (CCQE) is simulated for both free protons and bound nucleons based on the models of (Llewellyn Smith, 1972) and (Smith and Moniz, 1972) respectively. A relativistic Fermi gas model is used in the bound

nucleon calculation. In both cases, the calculation uses vector and axial vector form factors. The vector mass is set to 0.84 GeV/c^2, and the axial vector mass is set to 1.2 GeV/c^2. Both are tuned to match model prediction with measurement from K2K (Gran et al., 2006) and MiniBooNE (Aguilar-Arevalo et al., 2008). Fig. 4.4 shows the calculated CCQE cross sections from NEUT and measurement results.

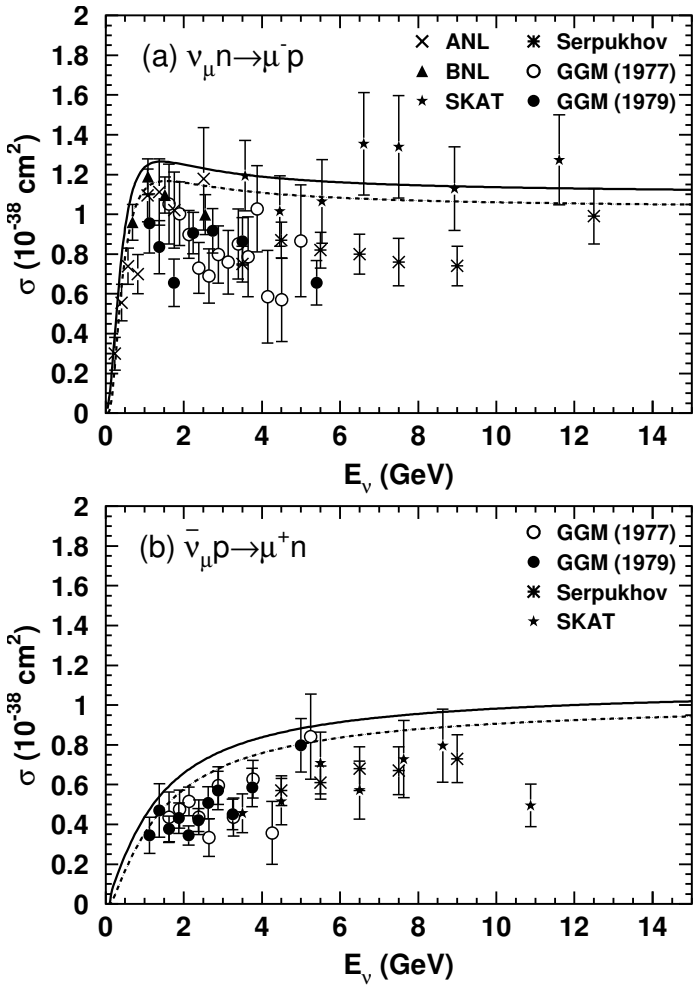

FIGURE 4.4: CCQE cross sections of ν_μ (top) and $\bar{\nu}_\mu$ from NEUT calculation, and overlaid measurement data from ANL (Barish et al., 1977), Gargamelle (Bonetti et al., 1977; Pohl et al., 1978), BNL (Ahrens et al., 1986), Serpukhov (Belikov et al., 1985) and SKAT (Brunner et al., 1990). Solid lines represent scattering off a free proton, and dashed lines represent scattering off bound nucleons in ^{16}O. Taken from (Hayato, 2009).

NC elastic cross sections are determined by scaling their charged-current quasi-

elastic counterparts (Hayato, 2009).

$$\sigma(\nu p \to \nu p) = 0.153 \times \sigma(\nu n \to e^{-} p), \tag{4.1}$$

$$\sigma(\bar{\nu} p \to \bar{\nu} p) = 0.218 \times \sigma(\bar{\nu} p \to e^{+} n), \tag{4.2}$$

$$\sigma(\nu n \to \nu n) = 1.5 \times \sigma(\nu p \to \nu p), \tag{4.3}$$

$$\sigma(\bar{\nu} n \to \bar{\nu} n) = 1.0 \times \sigma(\bar{\nu} p \to \bar{\nu} p) \tag{4.4}$$

4.2.2 Meson Exchange Current

In the CCQE interactions on a bound nucleon described above, an assumption is made that direct correlations between the nucleons in the nucleus are negligible such that a neutrino interacts with a single nucleon. However, the correlations among the nucleons can result in neutrino interaction that involve multiple nucleons, which is known as meson exchange current interactions (MEC). The MEC is conceived to be responsible for the tension between the existing CCQE model and the data from experiments such as MiniBooNE (Aguilar-Arevalo et al., 2013). MEC interactions simulation has been recently introduced to NEUT, based on the model by (Nieves et al., 2011).

4.2.3 Single Meson Production

Single meson production is the dominant hadron production mechanism in the region where the hadronic invariant mass is less than 2.0 GeV/c^2. Rein and Seghal's method is adopted to simulate the neutrino induced single pion production (Rein and Sehgal, 1981). In this method, the interaction is split into two steps as:

$$\nu + N \to l + N^{*}, N^{*} \to \pi + N', \tag{4.5}$$

where N and N' are nucleons, N^{*} is the baryon resonance. In total, 18 resonances below 2 GeV/c^2 are taken into account. Their amplitudes of production, multiplied by the decay probability of a resonance into one pion and one nucleon, are calculated

to obtain the cross sections. Interferences among the resonances are also taken into account in the calculation. The pion angular distribution in the final state is calculated from the Rein and Sehgal model for the $\Delta(1232)$ resonance, and is assumed to be isotropic for other resonances. The Pauli blocking effect in the decay of resonance is taken into account by requiring the momentum of nucleon larger than the Fermi surface momentum. Finally, absorption of pions is also considered, resulting in about 20% of single pion production interactions having only an outgoing lepton and nucleon. Fig. 4.5 shows the calculated charged current single pion production cross sections and experimental measurements.

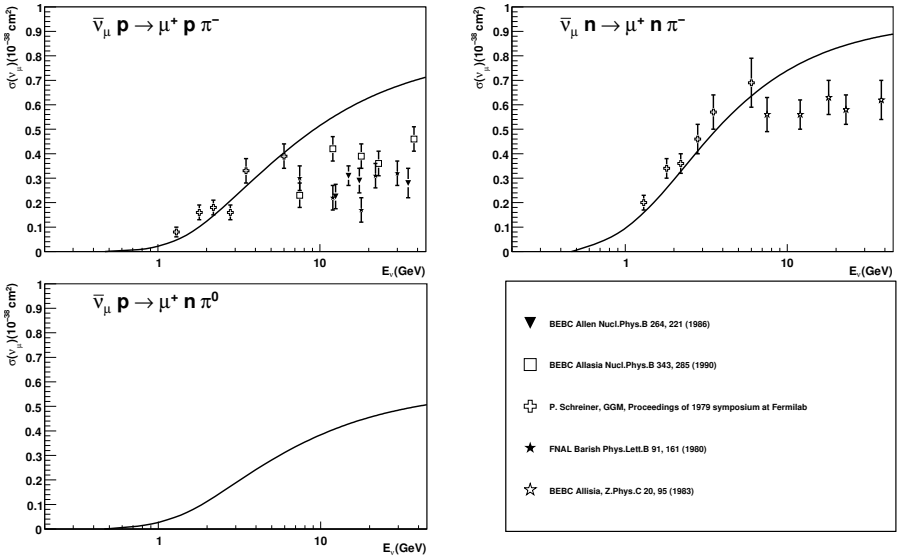

FIGURE 4.5: Cross section for $\bar{\nu}_\mu$ charged current single pion productions. Solid lines are NEUT calculations, points are experimental data. Taken from (Hayato, 2009).

Based on the amplitudes of neutrino resonance productions in Rein and Seghal's model, it is also possible to calculate the cross sections of single photon, K, and η production by changing the decay probabilities of the resonances. These interactions are also included in the simulation package.

In coherent pion production, the incident neutrino interacts with the entire oxy-

gen nucleus producing a pion. Due to the low momentum transfer in the interaction, the outgoing lepton and pion produced in this process are peaked in the forward direction. The interaction is simulated with a modified Rein and Seghal model (Rein and Sehgal, 1983).

4.2.4 Deep Inelastic Scattering

In deep inelastic scattering (DIS), the incident neutrino interacts with a quark in the target nucleons and produces multiple hadrons. The process is included when the hadronic invariant mass > 1.3 GeV/c^2. The cross section is calculated by integrating the following equation:

$$\begin{aligned}
\frac{d^2\sigma}{dxdy} =& \frac{G_F^2 M_N E_\nu}{\pi}((1-y+y^2+C_1)F_2(x,q^2) \pm y((1-\frac{y}{2}+C_2))xF_3(x,q^2)), \\
C_1 =& \frac{yM_l^2}{4M_N E_\nu x} - \frac{xyM_N}{2E_\nu} - \frac{}{M_l^2}4E_\nu^2 - \frac{M_l^2}{2M_N E_\nu x}, \\
C_2 =& -\frac{M_l^2}{4M_N E_\nu x},
\end{aligned} \tag{4.6}$$

where M_N and M_l are the nucleon and outgoing lepton mass, E_ν is the neutrino energy, q^2 is the squared momentum transfer, and the variables $x = -q^2/(2M_N(E_\nu - E_l))$ and $y = (E_\nu - E_l)/E_\nu$ are the Bjorken scaling parameters. The nucleon form factors, F_2 and xF_3, are taken from the GRV98 parton distribution functions (Gluck et al., 1998), with corrections from Bodek and Yang (Bodek and Yang, 2002) in the low q^2 region. The NC cross sections are obtained by multiplying the CC cross section by linear functions of neutrino energy (Hayato, 2009). The probability of pion multiplicity, which is a function of W, provides the probability to generate more than one pion in the region 1.3GeV/c^2 < W <2.0 GeV/c^2. The average multiplicity of charged pions is estimated from the Fermilab 15-foot hydrogen bubble chamber experiment (Derrick et al., 1978) as

$$\langle n_\pi \rangle = 0.09 + 1.83\ln(W^2). \tag{4.7}$$

The number of pions in each event is determined with KNO scaling (Hayato, 2009). The forward-backward asymmetry of pion multiplicity in the hadronic center of mass is included by using the result of BEBC experiment (Barlag et al., 1982) as:

$$\frac{n_\pi^F}{n_\pi^B} = \frac{0.35 + 0.41 \ln W^2}{0.5 + 0.09 \ln W^2}. \tag{4.8}$$

In the region of W>2.0GeV/c^2, PYTHIA/JETSET (Sjostrand, 1995) is used to determine the hadron kinematics.

4.3 Simulation of Charged-current Tau Neutrino Interactions

4.3.1 Simulation of Tau Neutrino Interactions in Water with NEUT

Although the original neutrino flux produced in the atmosphere only consists of electron and muon neutrinos, tau neutrinos are also detected in Super-K due to neutrino oscillations. NEUT is used to simulate tau neutrino interactions as well. Because NC simulation has included neutrinos of all three flavors, only charged-current tau neutrino interactions are simulated and added to the final simulation sample. In the NEUT simulation, the following charged-current tau neutrino interactions are considered:

- $\nu_\tau N \rightarrow \tau N'$, charged-current quasi-elastic scatter
- $\nu_\tau N \rightarrow \tau N' \pi$, charged-current single π production
- $\nu_\tau N \rightarrow \tau N' \gamma$, charged-current single γ production
- $\nu_\tau N \rightarrow \tau \Lambda' \pi$, charged-current single kaon production
- $\nu_\tau N \rightarrow \tau N' \eta$, charged-current single η production
- $\nu_\tau N \rightarrow \tau N' hadrons$, charged-current deep inelastic scattering

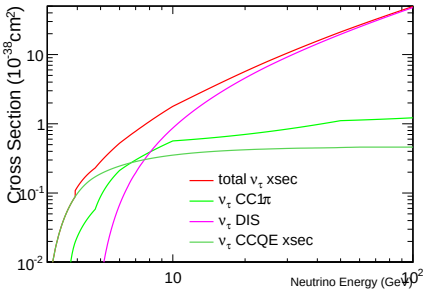

(a) The charged-current ν_τ neutrino cross sections as a function of neutrino energy for different channels in NEUT.

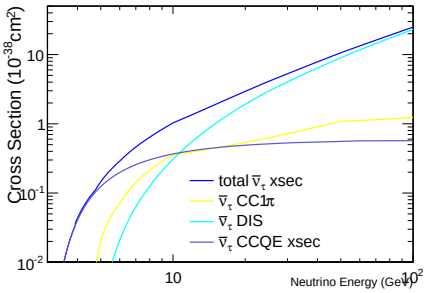

(b) The charged-current $\bar{\nu}_\tau$ neutrino cross sections as a function of neutrino energy for different channels in NEUT.

FIGURE 4.6: Charged-current tau neutrino cross sections in NEUT.

- $\nu_\tau^{16}O \rightarrow \tau\pi X$, charged-current coherent π production

The cross sections for CC tau neutrino interactions are calculated with the same models for ν_μ and ν_e neutrinos as described in (Hayato, 2009). However, in order to account for the large mass of tau lepton, the kinematic effect of the tau lepton mass is considered in the calculation. The kinematic effect of tau lepton mass requires that the minimum neutrino energy in the rest frame of the target nucleon is

$$E_{min} = m_\tau[1 + \frac{m_\tau}{2m_N}] = 3.5\,\text{GeV} \tag{4.9}$$

where m_τ is the mass of tau lepton, and m_N is the mass of the target nucleon. Lepton mass corrections are employed in single and coherent pion production based on models in (Berger and Sehgal, 2007; Rein and Sehgal, 2007). In the simulation of DIS interactions, the GRV98 model (Gluck et al., 1998) is used, and a correction from (Bodek and Yang, 2002) is implemented to match the DIS cross section and resonance production cross section smoothly. Fig. 4.6 shows the charged-current tau neutrino cross sections for the three most important channels and the total charged-current cross sections for ν_τ and $\bar{\nu}_\tau$ in NEUT. As shown in the figure, ν_τ has a larger cross section than $\bar{\nu}_\tau$. CCQE dominates at the low energies ($E_\nu < 5$ GeV), while

DIS has a much larger cross section than other channels at high energies (E_ν >10 GeV). At intermediate energies, resonance production is expected to dominate.

4.3.2 Modeling the Polarization of Tau Lepton

The tau leptons produced in the CC tau neutrino interactions are polarized, and the polarization affects the decay particle distributions of the tau lepton. In the τ rest frame, in which z-axis is taken along τ's momentum direction, a spin polarization vector is defined as:

$$\overrightarrow{s} = (s_x, s_y, s_z) = \frac{P}{2}(\sin\theta_P \cos\phi_P, \sin\theta_P \sin\phi_P, \cos\theta_P) \tag{4.10}$$

where θ_P and ϕ_P are the polar and azimuthal angle of the spin vector in the τ rest frame respectively. The azimuthal angle is measured from the scattering plane where $\phi_P = \pi/2$ is along the $\overrightarrow{p}_\nu \times \overrightarrow{p}_\tau$ direction in the lab frame. P represents the degree of polarization, with P=1 for the fully polarized τ, and P=0 for the unpolarized case. The degree of polarization and the spin direction are functions of energy and direction of outgoing τ. The polarization of tau leptons produced in the neutrino interactions is modeled in the simulation with the predictions from (Hagiwara et al., 2003) for quasi-elastic, resonance production and deep inelastic respectively. Fig. 4.7 shows the polarization vector $\overrightarrow{s}$ of τ^- produced in ν_τ DIS interactions at E_ν=10 GeV on the $p_\tau \cos\theta$-$p_\tau \sin\theta$ plane, where p_τ and θ are the momentum and scattering angle of τ^- in the lab frame.

4.3.3 Simulation of Tau Lepton Decay with Tauola

The tau lepton has a short lifetime of 2.9×10^{-13} s, thus is not directly detected in Super-K. The tau lepton decay has multiple channels, including leptonic decays and hadronic decays. The tau lepton decay channels with branching ratio larger than 1% are presented in Table 4.1 from (Patrignani et al., 2016). Multiple charged particles

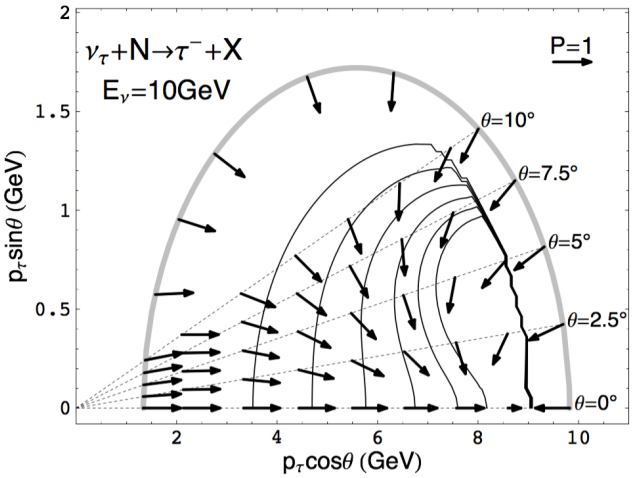

FIGURE 4.7: The contour plot of the DIS τ^- polarization in the plane of $p_\tau \cos\theta$ and $p_\tau \sin\theta$ for ν_τ charged-current DIS process at E_ν=10 GeV. The thick gray line represents the kinematic boundary. The QE scattering contributed along the boundary, and the RES process contributes just inside of the boundary. The length of the arrows shows the degree of polarization, and the direction gives the τ^- spin in the τ^- rest frame. Taken from (Hagiwara et al., 2003).

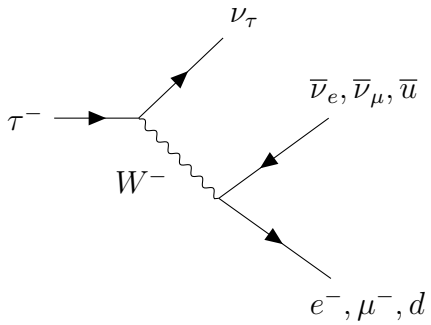

FIGURE 4.8: Feynman diagram of a tau lepton decay.

are produced in most hadronic tau decays. Due to the multiple charged particles and high-energy lepton, the leptonic decays of the tau look very similar to normal CC DIS interactions from ν_μ and ν_e.

The decays of the tau leptons themselves are simulated by the tau lepton decay library, TAUOLA (version 2.6) (Davidson et al., 2012). Secondary particles from TAUOLA simulation are propagated to NEUT and the custom code for further simulation is the same as that used for the simulation of other atmospheric neutrino

Table 4.1: Decay modes of tau leptons with branching ratio larger than 1%. Adapted from (Patrignani et al., 2016).

Decay mode	Branching ratio (%)
$\mu^-\bar{\nu}_\mu\nu_\tau$	17.41 ± 0.04
$e^-\bar{\nu}_e\nu_\tau$	17.83 ± 0.04
$\pi^-\nu_\tau$	10.83 ± 0.06
$\pi^-\pi^0\nu_\tau$	25.52 ± 0.09
$\pi^-2\pi^0\nu_\tau$	9.3 ± 0.11
$\pi^-3\pi^0\nu_\tau$	1.05 ± 0.07
$\pi^-\pi^+\pi^-\nu_\tau$	8.99 ± 0.06
$\pi^-\pi^+\pi^-\pi^0\nu_\tau$	8.99 ± 0.06
$h^-\omega\nu_\tau$	2.00 ± 0.08

interactions.

4.4 Final State Interaction

Hadrons produced inside of nuclei are known to interact with surrounding nucleons, these interactions are known as final state interactions (FSI). Therefore, the FSI of pions, kaons, etas and nucleons in the target are also simulated in NEUT. Pions are the most common hadrons produced at Super-K, and it is important to accurately simulate pion interactions. Pion FSI include four types of interactions: quasi-elastic scattering in which a single pion of the same charge remains after the interaction, charge exchange in which a charged pion is converted into a π^0 or vice versa, pion absorption in which no pions remain after the interaction and pion production in which multiple pions are produced. Pion FSI are simulated by a NEUT cascade model (de Perio, 2011). In the model, pions are propagated classically in finite steps through a nuclear medium described by Woods-Saxon nuclear density profile (Woods and Saxon, 1954). At each step, the probabilities for various interactions are calculated. The model has been tuned based on pion-nucleon and pion-nucleus scattering data. Fig. 4.9 shows the tuned $\pi^+ - {}^{12}C$ scattering cross sections simulated in NEUT compared with experimental data.

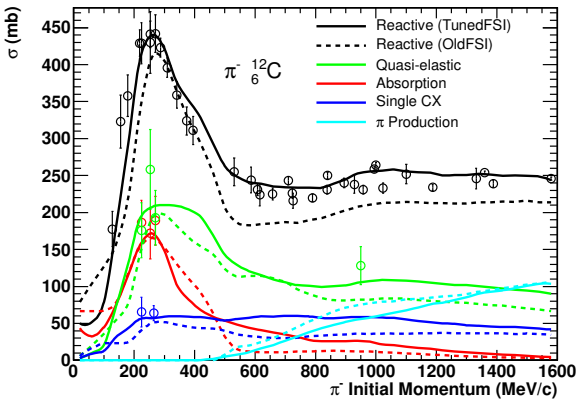

FIGURE 4.9: $\pi^+ - ^{12}C$ scattering cross sections, where the cross sections for each interaction process are shown separately by the colors described in the legend. The data pions are the measurement from $\pi^+ - C$ scattering experiments and the solid lines are the cross sections from the tuned NEUT pion cascade model. The dashed lines are for the previous NEUT pion FSI model. Taken from (de Perio, 2011).

4.5 Detector Simulation

After the simulations of the neutrino interactions and nuclear interactions in NEUT, final state particles are propagated into a custom detector simulation package called SKDETSIM. The simulation tracks the particles, models Cherenkov radiation and photon propagation, and simulates the PMT response. The simulation is based on GEANT3 (Brun et al., 1987).

Hadronic interactions are simulated with GCALOR (Zeitnitz and Gabriel, 1994) except for pions below 500 MeV/c for which the NEUT cascade model is used. Cherenkov radiation is modeled using inputs from the water calibration described in Section 3.6.2. The scattering and absorption of photons in the water are modeled based on the calibration result in Section 3.6.2. Reflection and absorption on different detector surfaces is modeled from calibration measurement. PMT response is modeled using the measured quantum efficiency of each PMT. The charge and time response of the PMTs and the electronics are also modeled based on the calibration measurements.

5

Atmospheric Neutrino Event Reduction and Reconstruction

Super-K records approximately 10^6 events per day. Most of the recorded events are from low background radioactivity surrounding the detector and cosmic ray muons, at a rate of 11 Hz and 3 Hz respectively. Therefore, dedicated reduction algorithms are implemented to select neutrino events from large number of events in Super-K.

Atmospheric neutrino events in Super-K are classified into three types based on the event topology: fully contained (FC), partially contained (PC), and upward-going muon (UPMU), as shown in Fig. 5.1. FC events have the reconstructed neutrino interaction vertex inside the ID, and the secondary particles deposit the energy in ID. PC events have the reconstructed vertex in the ID, but the secondary particles pass through the ID and produce Cherenkov radiation in both ID and OD. UPMU events are muons produced by the neutrinos coming from the opposite side of the Earth and interacting with the rock below the Super-K detector. UPMU events are further classified into upward stopping muons that lose energy and stop in the ID and upward through-going muons that traverse the detector volume. These samples are used in various Super-K atmospheric neutrino analyses. The analysis in this

dissertation only uses FC events. The FC reduction and the updated PC reduction are presented below.

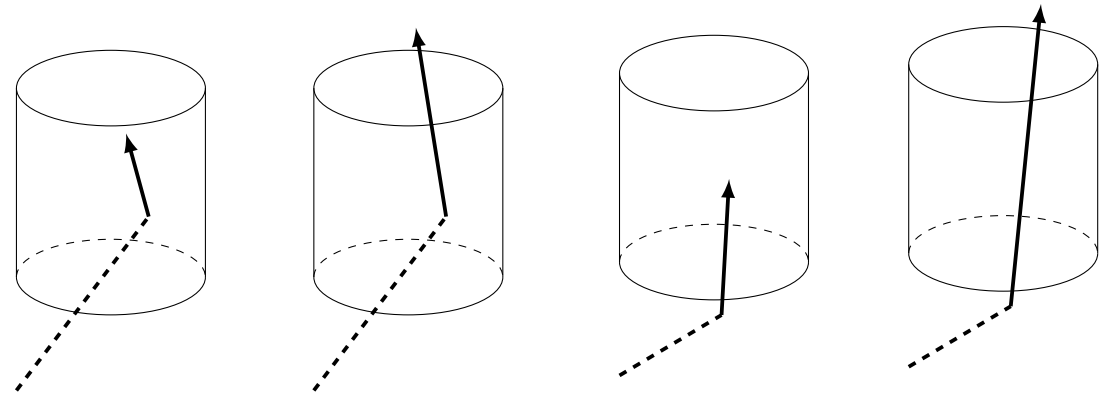

FIGURE 5.1: Schematic view of three types of neutrino events in Super-K.

5.1 Full Contained Sample

The FC reduction is divided into five stages, denoted as FC1-FC5, where events that pass each step are further processed in order to optimize the processing time. The reduction cuts were defined by comparing raw data with expectations from the Super-K atmospheric neutrino simulations, with a requirement of at least 99% efficiency for selecting true high-energy neutrino events at each step and rejection of background at the level of less than 1%.

5.1.1 FC1

The first stage requires very basic cuts:

1a. PE_{300} >200 (100 for SK-II), where PE_{300} is the total charge in the ID collected in a 300 ns wide time window. 200 p.e.s is roughly the charge deposited by a 22 MeV/c electron, which is lower than the 30 MeV energy threshold for

high energy neutrino analyses. This cut rejects most of the background from low-energy radioactivity.

1b. $\mathrm{NHITA}_{800} < 50$ (55 for SK-IV), where NHITA_{800} is the total number of OD tubes hit within a time window (-500 ns, +300 ns) relative to the trigger time. This cut removes most of the cosmic ray muons. The cut value is slightly larger in SK-IV because of the replacement of the OD electronics and changes in the PMT gains.

After the first reduction, the event rate is reduced from 10^6 per day to about 3000 events per day. The efficiency for selecting atmospheric neutrino events with energy more than 30 MeV is estimated by applying the FC1 cuts to the atmospheric neutrino MC and is found to be 100.0%.

5.1.2 FC2

The cuts used in FC2 are defined as

2a. $\mathrm{NHITA}_{800} \leqslant 25$ for events with $\mathrm{PE}_{total} < 100,000$ (50,000 for SK-II). This further removes cosmic ray muons, but allows extremely energetic events originating in the ID.

2b. $\mathrm{PE}_{max}/\mathrm{PE}_{total} < 0.5$, where PE_{max} is the largest number of p.e's observed in a single PMT. This is to remove electrical noise events which have a single PMT containing most of the total charge.

Fig. 5.2 illustrates the effects of two cuts in this step graphically. Following the FC2 reduction, the event rate is reduced to about 500 events per day, and the efficiency of FC2 to select atmospheric neutrino events is estimated to be still 100%.

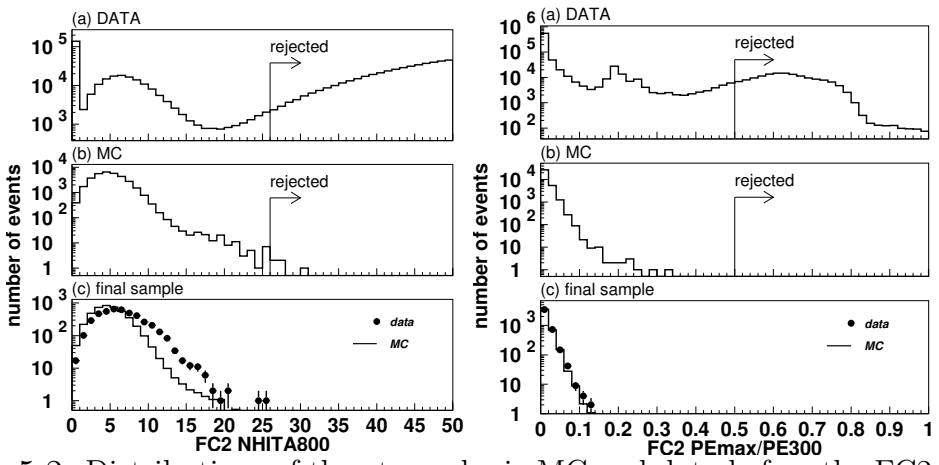

FIGURE 5.2: Distributions of the atmospheric MC and data before the FC2 cuts 2a (left) and 2b (right). MC events are high-energy FC neutrino events in FV, and data represent the events that pass the FC1 reduction. Taken from (Lee, 2012).

5.1.3 FC3

The third reduction has a set of complicated cuts that are designed to remove remaining cosmic ray muons and low-energy radioactivity.

Through-going muon cut

Through-going muons are very energetic and deposit an extremely large amount of charge in the ID. In order to remove these events, a through-going muon fitter is applied on events that have more than 1000 PMTs and collect more than 230 p.e.s. The fitter finds the entering point of the muon in the ID by searching for the earliest hit PMT with neighbor hit PMTs. The exiting point of the muon is defined as the center of the saturated ID PMTs. The goodness of the through-going muon fit is defined as:

$$goodness = \frac{1}{\sum_i \frac{1}{\sigma_i^2}} \times \sum_i \frac{1}{\sigma_i^2} e^{-\frac{(t_i - T_i)^2}{2(1.5\times\sigma_i)^2}}. \quad (5.1)$$

Events that meet the following criteria are classified as through-going muon, and therefore are removed:

3a. goodness>0.75

3b. $NHITA_{in} \geqslant 10$ or $NHITA_{out} \geqslant 10$, where $NHITA_{in}$ ($NHITA_{out}$) is the number of OD hit PMTs located within 8 m from the entrance (exit) point within a 800 ns time window.

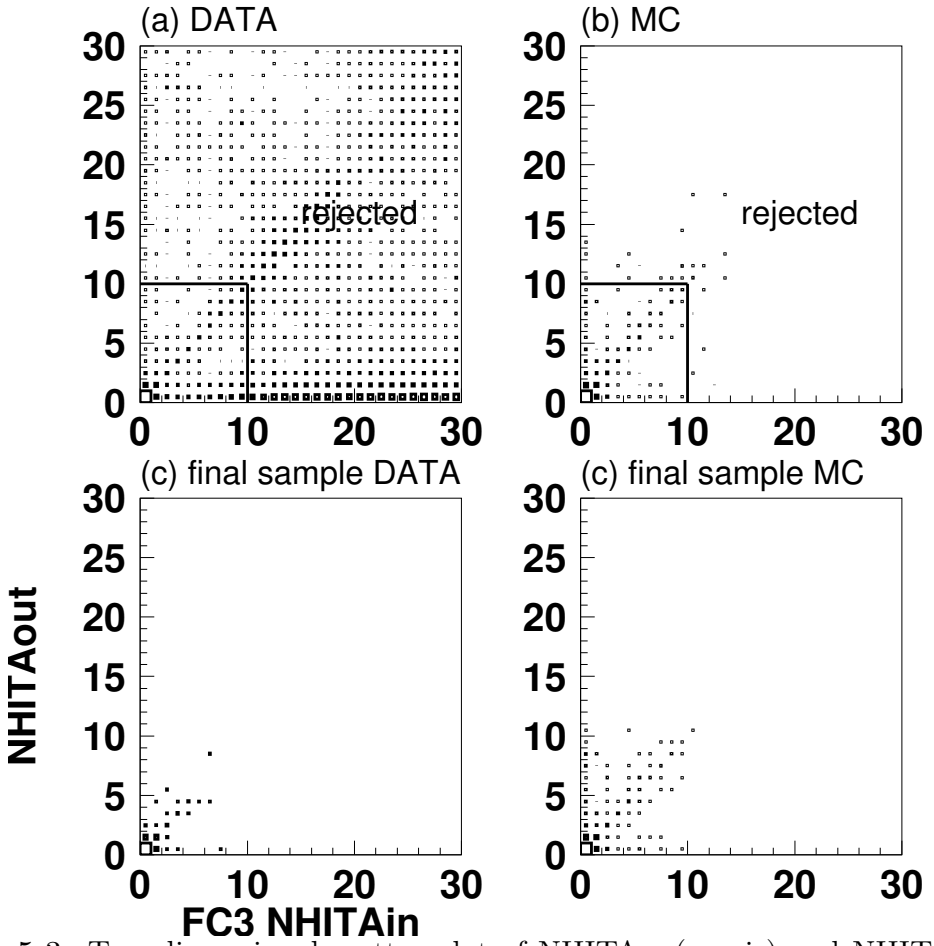

FIGURE 5.3: Two-dimensional scatter plot of NHITA$_{in}$ (x-axis) and NHITA$_{out}$ for through-going muons selection in FC3 reduction for SK-III. (a) shows the data after the FC2 reduction. (b) shows MC events after the FC2 reduction. (c) shows the final sample for data (bottom left) and Monte Carlo (bottom right) events. Cut values are indicated by solid lines. Taken from (Lee, 2012).

Events that satisfy the above criteria are tagged as through-going muons and are rejected. Fig. 5.3 shows the scatter plot of NHITA$_{in}$ and NHITA$_{out}$ that have through-going muon goodness larger than 0.75 for data and MC after the 2nd reduction and the final FC sample.

Additionally, a cut is applied to remove extremely energetic through-going muons which are expected to deposit more energy via pair production and bremsstrahlung than ionization. The energy deposition per unit track length is higher than 2 MeV/cm. Events satisfying the following cut are removed:

3c. $\mathrm{NHITA}_{500} > 400$, where NHITA_{500} is the number of OD hits within 500 ns sliding time window.

Stopping muon cut

The stopping muon selection follows a similar logic as for the through-going muon selection, except there is no exit point. The direction of the muon is found by maximizing the charge seen by the PMTs within a 42-degree opening angle from the entry point. A goodness parameter with the same definition as Equation 5.1 is calculated. The criteria for selecting stopping muon events are defined as:

3d. $\mathrm{NHITA}_{in} \geqslant 10$ (or $\mathrm{NHITA}_{in} \geqslant 5$ if goodness of stopping muon fit $\geqslant 0.5$ for SK-I)

Cable hole cut

On top of the stainless steel structure where PMTs are mounted, there are twelve cable holes for the signal and high voltage supply cables to pass through. There is no OD PMT installed at the positions of these holes. Muons passing through these holes may not be noticed by the OD. In order to compensate for the dead area in the OD, veto counters (2 m$\times$2.5 m plastic scintillation counters) were installed in April, 1997 at four large cable holes. (For the other eight smaller holes without veto counter, software background rejection will be applied in FC5.) Fig. 5.6 shows the positions of the twelve cable holes and the 4 veto counters.

An event is removed if:

3e. cable hole veto counter is hit.

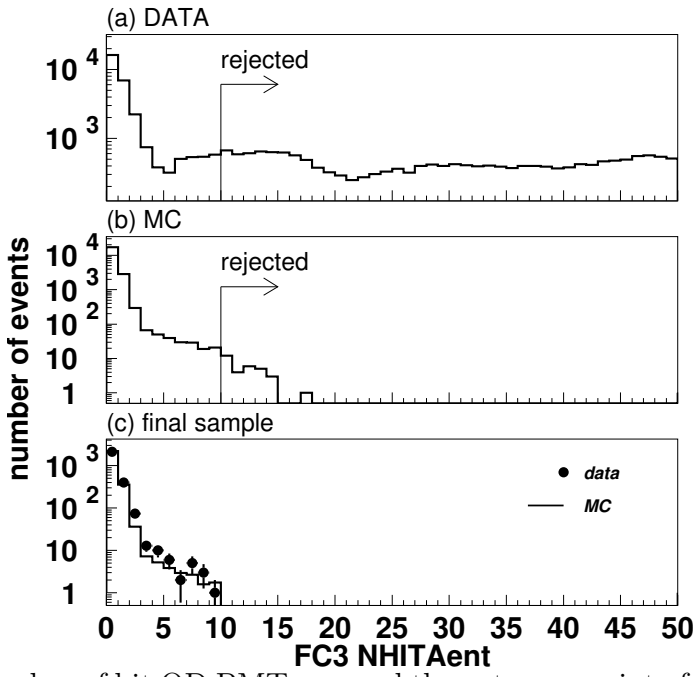

FIGURE 5.4: Number of hit OD PMTs around the entrance point of muons for events in FC3 stopping muon reduction in SK-IV. (a) shows the data after FC2 reduction. (b) shows FC MC events after FC2 reduction. (c) shows the final samples for data and MC after FC reduction. Taken from (Lee, 2012).

3f. L_{veto} <4 m, where L_{veto} is the distance from the cable hole to the event vertex.

In SK-IV, a tighter selection is applied to reject stopping cable hole muons. Events that satisfy the following criteria are removed:

3g. goodness > 0.4;

3h. PE_{total} > 4000;

3i. $\cos(\theta)$ <-0.6, where θ is the muon's zenith angle;

3j. The entry point of is within 2.5 m of the nearest cable hole.

Flasher event cut

A "flasher" is caused by repetitive discharge in the dynode of a PMT, which may also affect nearby PMTs. Flasher events typically have broader hit timing

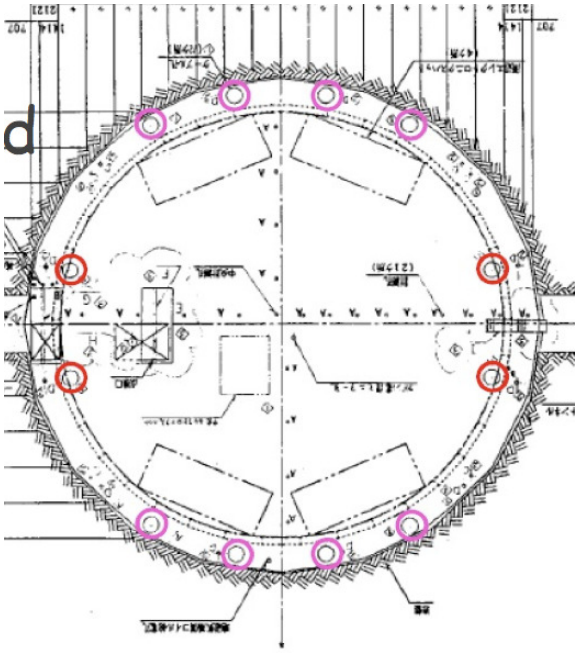

FIGURE 5.5: Schematic view of the positions of the twelve cable holes on the stainless steel support. Four holes in red circles are installed with veto counter. Taken from (Fukuda et al., 2003).

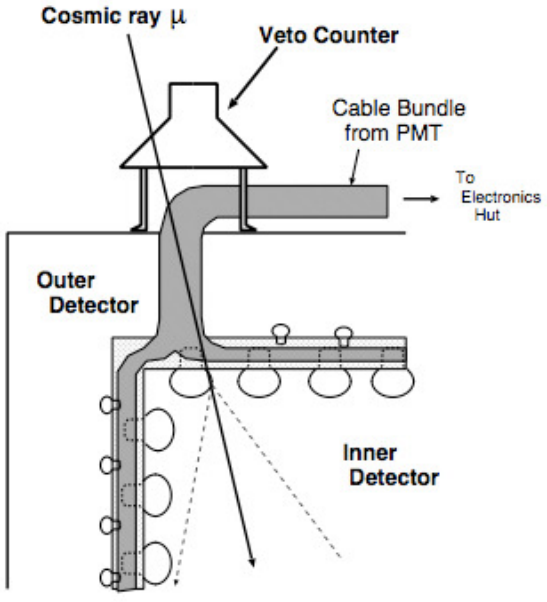

FIGURE 5.6: Schematic view of a cable hole muon and a veto counter. Taken from (Fukuda et al., 2003).

distributions than neutrino events, as shown in Fig. 5.7. Therefore, events that satisfy the following detector-specific criteria are rejected:

3k. (SK-I) $\mathrm{NMIN}_{100} \geqslant 15$, or $\mathrm{NMIN}_{100} > 10$ if $\mathrm{N}_{hit} \leqslant 800$, where NMIN_{100} is the minimum number of ID PMT hits in a 100 nsec time window from 200 ns to 700 ns after the trigger time, and N_{hit} is the total number of ID hits.

3l. (SK-II to IV) $\mathrm{NMIN}_{100} \geqslant 20$.

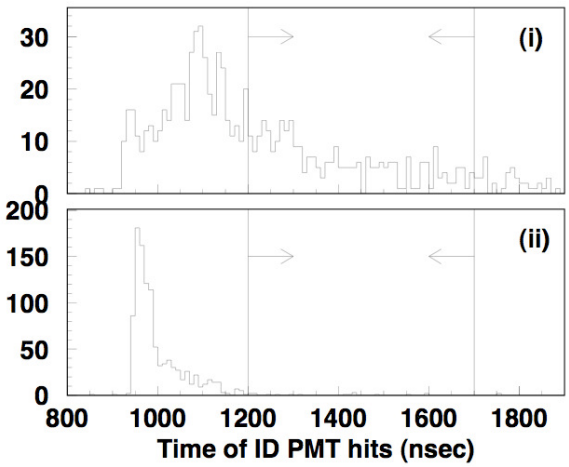

FIGURE 5.7: The timing distribution of a flasher (top) and an atmospheric neutrino MC event (bottom). The arrows indicate the time window for counting NMIN_{100}. Taken from (Lee, 2012).

Fig. 5.8 shows the NMIN_{100} distributions for data and FC MC after FC2 reduction and in the final samples.

Coincidence muons

Sometimes a cosmic ray muon enters in the trigger window of a low energy event. The coincidence avoids the cuts designed to remove low-energy events because of the energy deposition of the muon. Additionally, it avoids the high-energy cuts because the OD activity of the muon is recorded later than the low-energy trigger. In order to remove these event, the following cuts are applied:

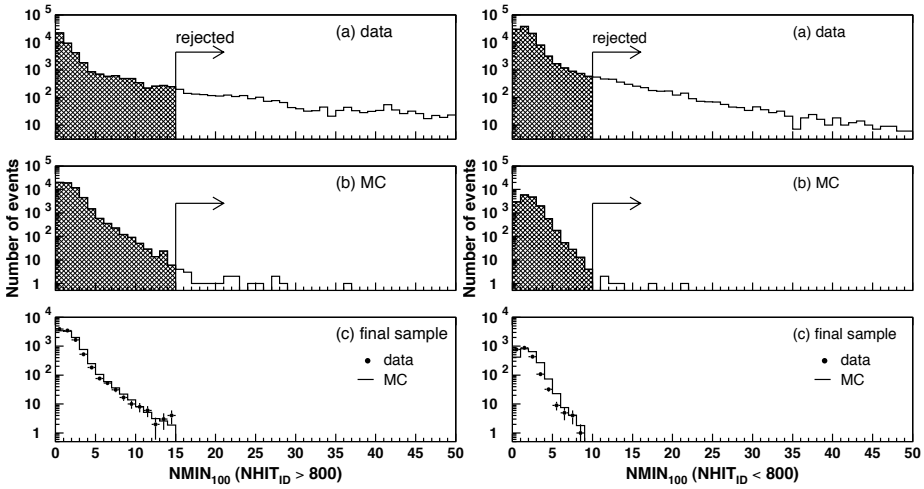

FIGURE 5.8: $NMIN_{100}$ distributions for events with more than 800 hit ID PMTs (left) and less than 800 hit ID PMTs (right). (a) shows the data after the FC 2nd reduction. (b) shows FC Monte Carlo events after the FC 2nd reduction. (c) shows the final samples for data and the Monte Carlo events, in which the number of Monte Carlo events is normalized to that of the data. Selection cuts are indicated by arrows. Taken from (Lee, 2012)

3m. $NHITA_{off} \geqslant 20$, where $NHITA_{20}$ is the number of OD hits between 300 nsec and 800 nsec after the trigger time;

3n. $PE_{off} > 5000$ (2500 for SK-II), where PE_{off} is the total p.e.'s in the ID for the same time window.

Low energy events

A specific cut is applied aiming to reject low-energy events. Events are removed if $NHIT_{50} < 50$ (25 for SK-II), where $NHIT_{50}$ is the number of ID hits within a sliding 50 nsec tie window. The time window uses the residual time that takes into account the time-of-flight of the photons assumed to come from a single vertex. $NHIT_{50}$ corresponds to visible energy of 9 MeV, which is safely lower than the energy threshold of 30 MeV for atmospheric neutrino analyses.

Following the FC3 reduction, the event rate is around 50 events per day. The efficiency of FC3 to select true neutrino events is estimated to be 99.8%.

5.1.4 FC4

The fourth reduction is designed to remove flasher events that were not removed by the above cuts. Flasher events usually emit light in a specific way, and create similar hit patterns across several event timing windows. Therefore, a pattern-matching algorithm is applied to reject them. The ID tank wall is divided into 1450 roughly equal 4 m^2 patches, and the total charge (n_{pe}) in each patch is computed. The correlation between two events (A and B) is computed as:

$$r = \frac{1}{N}\sum_i \frac{(Q_i^A - \langle Q^A \rangle) \times (Q_i^B - \langle Q^B \rangle)}{\sigma_A \times \sigma_B}, \tag{5.2}$$

where N is the number of patches, Q_i is the summed n_{pe} in each patch i, and σ is the standard deviation of the Q_i. If the distance between the PMTs with maximum charge in the two events is smaller than 75 cm, an offset of 0.15 is added to r. Another matching parameter, d_{ks} is also computed by comparing the time distribution of the charge by a Kolmogorov-Smirnov test. These two parameters are combined into a likelihood parameter "Prob". The events with Prob exceeding 3.0 are removed.

The event rate after FC4 reduction is about 32 events per day, with a neutrino efficiency of 99.6%.

5.1.5 FC5

The fifth reduction is designed to reject three specific categories of remaining background: invisible muons, coincidence muons, and long-tail flashers.

Invisible muons Cosmic ray muons with momenta below the Cherenkov threshold will pass the above reduction stages, but their decay electron can still be recorded. These events are rejected by activity in the OD. Events satisfying the following criteria are removed:

5a. $PE_{total} < 1000$ (500 for SK-II);

5b. NHITAC$_{early}$ + NHITAC$_{500}$ $\geqslant$10 if Dist$_{clust}$ < 500 cm; NHITAC$_{early}$ > 9 otherwise, where NHITAC$_{early}$ is the maximum number of OD PMT hits in the cluster within in a 200 nsec sliding time window from -9000 to -200 nsec prior to the primary trigger time, NHITAC$_{500}$ is the hits in the time window of -200 to 300 nsec, and Dist$_{clust}$ is the distance between the two OD clusters.

Coincidence muons

The remaining coincidence muon events are further removed by the following cuts:

1. PE$_{500}$ < 300 p.e.s (150 p.e.s for SK-II), where PE$_{500}$ is the total number of p.e.s recorded in the ID in a fixed time 500 nsec time window from -100 nsec to +400 nsec.

2. PE$_{late}$ $\geqslant$ 20 p.e.s, where PE$_{late}$ is the maximum number of OD hit PMTs in a 200 nsec sliding time window fro +400 nsec to +1600 nsec.

Sub-cable hole muons

Besides the cable hole muon cut in FC3, another cut is introduced in SK-IV to remove cosmic ray muons passing through eight sub-cable holes where veto counters are not installed. The events satisfying the following criteria are rejected:

1. Goodness of stopping muon fit $\geqslant$ 0.4;

2. PE$_{tot}$ > 4000;

3. downward direction ($\cos\theta$ <-0.6);

4. L$_{veto}$ < 2.5 m.

Long-tail flasher

A tighter flasher reduction than in FC3 reduction is applied, which removes events that satisfy the following criteria:

1. $NMIN_{100}$ $\geqslant$6 if goodness of Point-fit<0.4, where $NMIN_{100}$ is the minimum number of ID hit PMTs in a sliding time window from +300 nsec to +800 nsec.

From SK-II, the following cuts at added

2. $NMIN_{100}$ $\leqslant$5 if goodness of Point-fit<0.3.

Following FC5 reduction, FC event rate becomes ∼20 events per day, and the estimated neutrino efficiency is 99.9%.

5.1.6 Final Reduction

In the FC data set after FC1-5 reduction, neutrino events that satisfy the following criteria are selected to be used in analyses:

1. The distance from the reconstructed neutrino event vertex to the ID wall is > 2 m.

2. Number of OD PMTs in the OD cluster is < 16 (10 for SK-II).

3. $E_{vis} > 30$ MeV. E_{vis} is defined as the energy of an electron that would produce the same amount of p.e.s as that in a event.

The cuts are expected to largely remove the remaining background events, such as radioactivity. The event rate after the above cuts is approximately 8 events per day. The neutrino efficiency of these cuts is estimated to be 99.2%. The selection efficiencies and the event rates in each Super-K periods are summarized in Table 5.1.

There is still a tiny portion of background events in the final sample, mostly cosmic-ray muons and flasher events. The final sample is eye-scanned, and the background events are tagged; however they are *not* removed from the analysis, in order to avoid a bias in the data and MC selection. The background contamination is summarized in Table. 5.2.

Table 5.1: Summary of selection efficiencies in each stages and event rates in the final FC samples for each Super-K period.

FC	SK-I	SK-II	SK-III	SK-IV
reduction step	selection efficiency (%)			
1st	100.0	99.97	100.0	100.0
2nd	100.0	99.92	99.98	99.99
3rd	99.93	99.78	99.81	99.82
4th	99.29	99.38	99.30	99.00
5th	99.26	99.30	99.24	98.95
5th (FV)	99.25	99.95	99.62	99.19
	Event rate			
event rate/day	8.21±0.07	8.24±0.10	8.41±0.12	8.09±0.09

Table 5.2: Estimated background contaminations in each Super-K period. Sub-GeV means events with $E_{vis} < 1.3$ GeV and Multi-GeV means events with $E_{vis} > 1.3$ GeV.

	SK-I		SK-II		SK-III		SK-IV	
BG	cosmic ray	flasher	cosmic ray	flasher	cosmic ray	flasher	cosmic ray	flasher
sub-GeV	0.2%	0.1%	0.2%	0.4%	0.3%	0.1%	0.1%	0.1%
multi-GeV	0.3%	0.5%	0.2%	0.2%	0.3%	0.2%	0.1%	0.1%

5.2 Event reconstruction

Following the FC reduction, the remaining events are put through a reconstruction algorithm in order to convert the charge and timing information of the PMTs into physical variables. The reconstruction starts from finding the vertex position of an event using PMT timing information. Following this, a ring-fitting algorithm based on Hough transformations is applied to identify Cherenkov rings. Finally, the particle identification (PID), and momentum, are calculated and decay electrons are searched for. I describe the reconstruction of fully-contained events here following the sequence of the reconstruction stages.

5.2.1 Vertex Fitting

The event vertex is determined in three steps. In the first step, a simple fit called Point-fit is applied. It assumes that the ID PMT hits are emitted from a point source, then uses ID PMT hit residual times relative to that point source to maximize a goodness of fit parameter:

$$G_P = \frac{1}{N}\sum_i \exp\left(-\frac{(t_i - t_0)^2}{2(1.5\times\sigma)^2}\right), \tag{5.3}$$

where N is the total number of ID PMT hits, t_i is the residual time of the ith hit PMT, t_0 is a free parameter to maximize the goodness G_P, and σ is the time resolution equal to 2.5 ns. The point that gives maximum goodness is taken as the event vertex. Then, the overall direction of an event is estimated as the sum of the charge-weighted directions from the reconstructed vertex to each hit PMT.

With the reconstructed vertex, the Cherenkov emission angle of the brightest ring is determined by searching for the edge of the ring. A goodness of fit parameter is defined with the assumed angle of the ring as:

$$Q(\theta_{edge}) = \frac{\int_0^{\theta_{edge}} PE(\theta)d\theta}{\sin\theta_{edge}} \times (\frac{dPE(\theta)}{d\theta})^2 \times \exp\left(-\frac{(\theta_{edge}-\theta_{exp})^2}{2\sigma_\theta^2}\right), \tag{5.4}$$

where PE(θ) is the angular distribution of the observed charge as a function of opening angle, θ, θ_{exp} and σ_θ are the Cherenkov opening angle expected from the charge within the Cherenkov cone and its resolution respectively. The charge in $PE(\theta)$ is corrected for attenuation and PMT angular acceptance. The ring direction and opening angle θ_{edge} are varied to maximize $Q(\theta_{edge})$.

Finally, the vertex direction is determined by a more precise fitter, TDC-fit, that takes into account scattering of light and the track length of the charged particle. Instead of calculating the residual time relative to one assumed vertex, the residual

time is calculated as:

$$t_i = t_i^0 - \frac{1}{c}\left|\vec{X}_i - \vec{O}_i\right| - \frac{n}{c}\left|\vec{P}_i - \vec{X}_i\right|, \text{ for PMTs within the Cherenkov ring edge;} \tag{5.5}$$

$$t_i = t_i^0 - \frac{n}{c}\left|\vec{P}_i - \vec{X}_i\right|, \text{ for PMTs outside the Cherenkov ring edge} \tag{5.6}$$

where $\vec{O}_i$ is the vertex position, $\vec{X}_i$ is the emission point along the particle track that produce hit i, $\vec{P}_i$ is the position of ith PMT, and n is the index of refraction. The goodness parameter is again maximized to determine the vertex.

The vertex reconstruction is evaluated using MC by comparing the reconstructed vertex with the true MC vertex. The resolution for multi-ring samples ranges from 50 to 100 cm.

5.2.2 Ring Counting

After the brightest Cherenkov ring and the vertex has been determined, other ring candidates are searched for using a Hough transform method. Fig. 5.9 illustrates the basic logic of the algorithm. By drawing charge-weighted virtual rings with 42-degree angle around each hit PMT, the direction of the ring is found at the point where most virtual rings overlap.

Ring candidates are evaluated iteratively using a likelihood method. The hypothesis of (N+1) rings is tested against the hypothesis of N rings, up to a maximum of five rings. During this process, previously found rings are kept fixed. The likelihood is defined as:

$$L_N = \sum_i \log\left(P(q^{obs}, \sum_{n=1}^{N} \alpha_n q_{i,n}^{exp})\right), \tag{5.7}$$

where α_n is a weight for ring n that is varied to maximize the likelihood, and P is a Gaussian probability:

$$P(q_i^{obs}, q_i^{exp}) = \frac{1}{\sqrt{2\pi\sigma^2}} \exp\left(-\frac{(q_i^{obs} - q_i^{exp})^2}{2\sigma^2}\right). \tag{5.8}$$

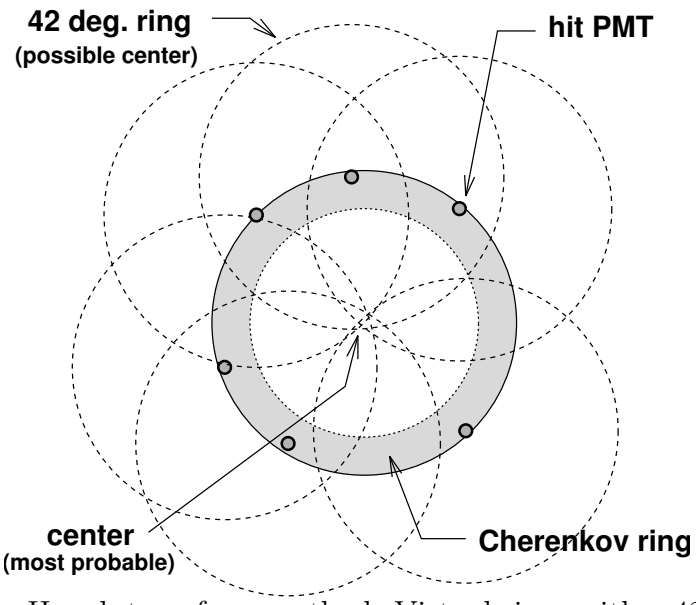

FIGURE 5.9: The Hough transform method. Virtual rings with a 42-degree opening angle are drawn around each hit PMT, and the ring center is found at the point at which most virtual rings overlap.

After finding all rings, particle type and momenta are estimated for each of them. Finally, the FC data are separated into single-ring and multi-ring events by cutting the likelihood distribution at zero. The likelihood distributions for sub-GeV and multi-GeV events are shown separated in Fig. 5.10.

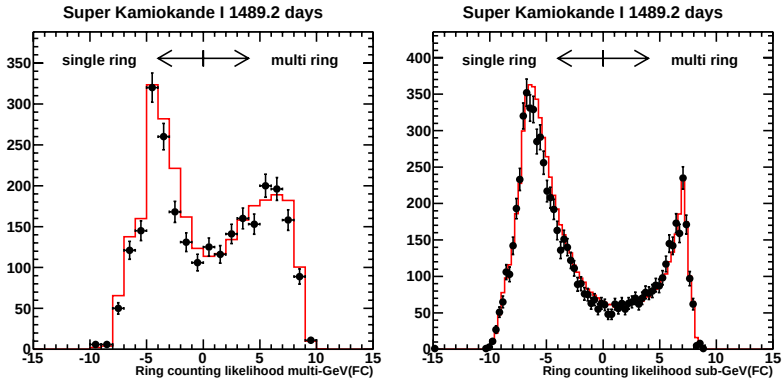

FIGURE 5.10: The ring likelihood distribution for sub-GeV events (left) and multi-GeV events (right) for SK-I. The data is shown in the black dots, and the MC with neutrino oscillations applied at Δm^2=2.1×10^{-3}eV^2 and $\sin^2(2\theta)$=1.0 is shown as the histogram. A cut in the likelihood separates single-ring from multi-ring events.

5.2.3 Particle Identification

Each ring found in ring counting is classified in two broad categories: "e-like" or "μ"-like by particle identification (PID). "e-like" events that are produced by electromagnetic showers and have a diffused ring pattern. High-energy electrons produce electromagnetic showers in the water via bremsstrahlung ($e^{\pm} \rightarrow e^{\pm}\gamma$), and photon pair production ($\gamma \rightarrow e^{-}e^{+}$), and multiple scattering of low energy electrons. High energy photons also produce electromagnetic showers via pair production. Because the cross section of bremsstrahlung is proportional to $1/M^2$, the more massive muons, charged mesons and protons rarely produce electromagnetic showers, especially in the full-contained events.

At typical energies of atmospheric neutrinos, muons interact primarily via ionization, and produce rings with sharp edges. Moreover, Cherenkov rings from these massive charged particles generally have smaller Cherenkov angles. Charged-mesons, particularly pions, also have sharp edges due to the lack of electromagnetic showers. However, the rings they form are usually thinner than those of muons because hadronic interactions can suddenly alter their path. Fig. 5.11 shows examples of e-like and μ-like rings. The particle identification algorithm (PID) works by comparing the observed charge distribution with an expected charge distribution under e-like or μ-like hypothesis, together with the opening angle information. The expected charge distribution for the ith PMT are defined as:

$$q_i^{exp}(e) = \alpha_e \times Q^{exp}(p_e, \theta_i) \times (\frac{R}{r_i})^{1.5} \times \frac{1}{e^{r_i/L}} \times f(\Theta) + q^{scat}, \tag{5.9}$$

$$q_i^{exp}(\mu) = (\alpha_\mu \times \frac{\sin^2\theta_{x_i}}{r_i(sin\theta_{x_i} + r_i \frac{d\theta}{dx}|_{x=x_i})} + q_i^{knock}) \times \frac{1}{e^{r_i/L}} \times f(\Theta) + q^{scat}. \tag{5.10}$$

where $\alpha_{e,\mu}$ are normalization factors, θ_i is the angle between the i^{th} PMT and the ring direction, $f(\Theta)$ is the PMT acceptance as a function of incident angle Θ_i, r_i is the distance between the vertex and the ith PMT, L is the photon attenuation length,

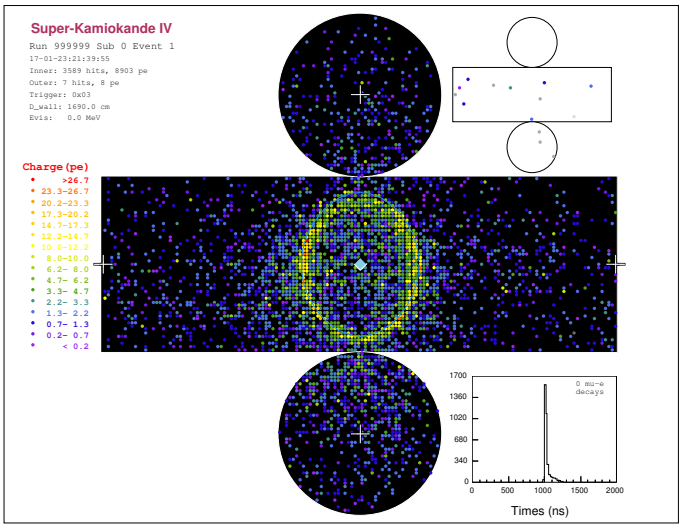

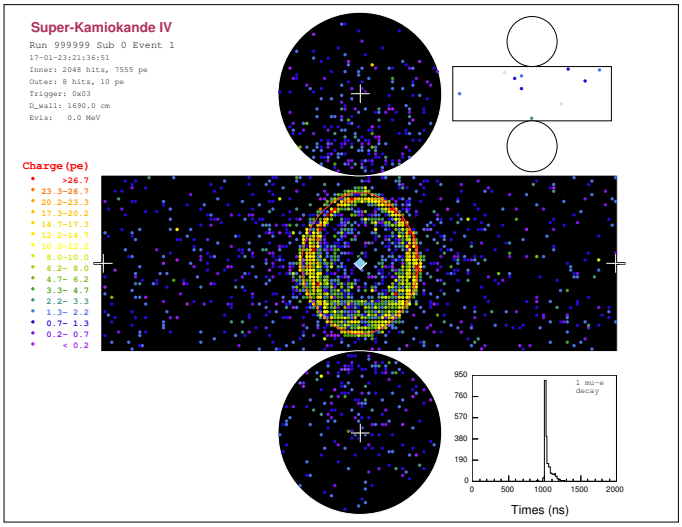

FIGURE 5.11: Simulated e^- and μ^-, both with momentum 1000 MeV/c. The ring pattern is sharper for μ^- and more diffuse for e^-. The color scale indicated the amount of charge deposited on the PMTs. The main display shows the ID, while the small display shows on the top right shows the OD, in which there is negligible activity.

and q_i^{scat} is the expected charge due to scattering for the i^{th} PMT. For the e-like hypothesis, MC simulations are used to estimate $Q^{exp}(p_e, \theta_i)$ at a vertex located at $R = 16.9$ m from the ID wall. The factor of $(R/r_i)^{1.5}$ accounts for the difference in diffusion between the test track length and the actual track length. For the μ-like hypothesis, x_i refers to the estimated point along the muon track from which photons propagate to the i^{th} PMT. The hypothesis also include contribution from "knock-on" electrons (q^{knock}) that are ionized by muons.

A likelihood function is calculated with the observed and expected charge distribution for the n^{th} ring as:

$$L_n(e,\mu) = \prod_{\theta_i < 1.5\times\theta_C} P(q_i^{obs}, q_{i,n}^{exp}(e,\mu) + \sum_{n' \neq n} q_{i,n'}^{exp}), \tag{5.11}$$

where the product is over all the PMTs within the cone with an opening angle of $\theta_c \times 1.5$, P is the Gaussian probability function defined in Equation 5.8, and the sum over n' accounts for light from overlapping rings. The likelihood is maximized by altering the direction and opening angle of each ring in order to optimize the expected charge distributions. The charge distribution likelihood is then converted to a χ^2 parameter,

$$\chi_n^2(e,\mu) = -2\log L_n(e,\mu) + const, \tag{5.12}$$

which is then used to construct a probability parameter:

$$P_n^{pattern} = \exp\left(-\frac{(\chi_n^2(e,\mu) - min(\chi_n^2(e), \chi_n^2(\mu)))^2}{2\sigma_{\chi_n^2}^2}\right), \tag{5.13}$$

where $\sigma_{\chi_n^2} = \sqrt{2N}$ for N PMTs in the likelihood calculation.

For multi-ring events, $P_n^{pattern}(e,\mu)$ is the final PID probability. For single-ring events, a second probability is calculated based on the Cherenkov angle:

$$P^{angle}(e,\mu) = \exp\left(-\frac{(\theta^{obs} - \theta^{exp}(e,\mu))^2}{2\delta\theta^2}\right), \tag{5.14}$$

where θ^{obs} is the reconstructed Cherenkov angle, $\delta\theta$ is the angle fitting error, and $\theta^{exp}(e,\mu)$ is the expected angle based on the reconstructed e/μ-like momentum.

The final PID probability of single-ring events is the product of these two probability estimators:

$$P(e,\mu) = P^{pattern}(e,mu) \times P^{angle}(e,\mu). \tag{5.15}$$

The final PID likelihood is defined as:

$$L_{PID} = \sqrt{-\log P(\mu)} - \sqrt{-\log P(e)}. \tag{5.16}$$

The distributions of the likelihood variable for single-ring events are shown in Fig 5.12. The FC data are separated into e-like and μ-like by cutting the PID variable at zero.

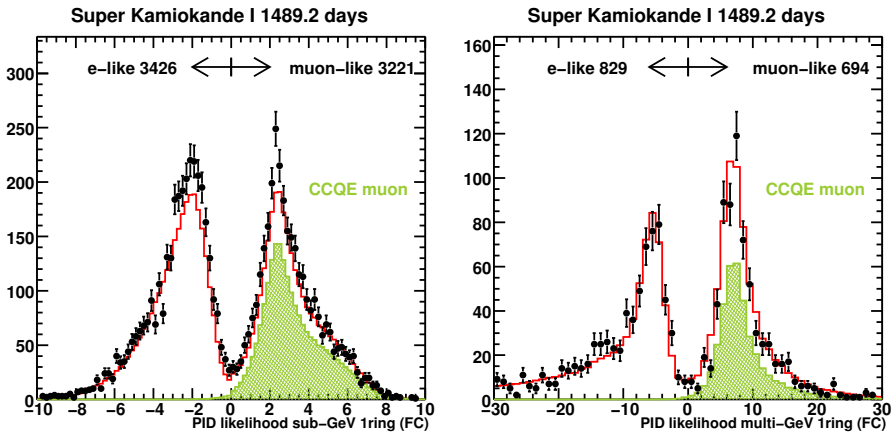

FIGURE 5.12: The distribution of particle identification likelihood for sub-GeV (top) and multi-GeV (bottom) single-ring FC events. The hatched histogram shows the MC contribution due to CC ν_μ interactions, the black dots show the data and the empty histogram shows the total MC with neutrino oscillations applied as in Fig. 5.10

5.2.4 Momentum Reconstruction

The momentum of a ring is determined by the observed p.e.s inside a Cherenkov cone with an opening angle of 70° and the energy scale described in Chapter 3. The

observed p.e.s in hit ID PMTs are first separated into distributions from each ring based on the expected p.e. distribution as:

$$q_{i,n}^{obs} = q_i^{obs} \times \frac{q_{i,n}^{exp}}{\sum_{n'} q_{i,n'}^{exp}}, \tag{5.17}$$

where $q_{i,n}^{obs}$ is the fraction charge from the n^{th} ring in the i^{th} PMT, q_i^{obs} ($q_{i,n}^{exp}$) is the observed (expected) p.e.s in the i^{th} PMT. The sum of observed charge from a ring is used to determine its momentum. In order to avoid charge from decay electron, the charge is restricted to a (-50, 250) ns time window relative to the time-of-flight subtracted timing peak. After taking account of light attenuation, light scattering, angular acceptance and PMT gain, the charge of a ring is calculated as:

$$RTOT = \frac{G_{MC}}{G_{DATA}}(\alpha \times \sum_i (q_i^{obs} \times e^{r_i/L} \times \frac{\cos\Theta_i}{f(\Theta_i)}) - \sum_i S_i), \tag{5.18}$$

where $\frac{G_{MC}}{G_{DATA}}$ is the relative PMT gain for MC and data, α is a normalization factor, r_i is the distance from the i^{th} PMT to the event vertex, L is the water attenuation length, $f(\Theta)$ is the acceptance of the PMT for incident angle Θ, S_i is the expected charge for the i^{th} PMT due to scattered photons.

5.3 Decay Electron Search

Muons that stop in the detector decay into electrons that may be observed. Decay electrons provide a relative independent information of event from the Cherenkov rings produced by the primary particles. They are searched for in a 20 μs time window after the event trigger. Decay electron candidates are divided into primary or "in-gate" events or sub-events, depending on their time. In SK-I-III, the search criteria for primary events are:

- 0.1 μs<t< 0.8 μs;

- $\mathrm{NHIT}_{30} \geqslant 60$ (30 for SK-II).

where t is the time after the event trigger, and NHIT_{30} is the number of hits in a 30 ns time window. For sub-events, the requirements are defined similarly as:

- 1.2 μs<t< 20 μs;
- $\mathrm{NHIT}_{30} \geqslant 40$ (20 for SK-II).

Additionally, both primary event and sub-event are required to have at least 50 hit ID PMTs (25 for SK-II), and the vertex goodness (Equation 5.3) greater than 0.5.

The decay electron tagging efficiency is estimated with MC. The efficiency is 80% for μ^+ and 63% for μ^- in SK-I-III. Due to the improvement of electronics in SK-IV, the time between 0.8 μs and 1.2 μs is included in the search. Therefore, the efficiency has increased to 96% for μ^+ and 80% for μ^- in SK-IV.

5.4 Summary of Reduction and Reconstruction

The data and MC are passed through the same reduction and reconstruction algorithms. The reduction selects the fully-contained atmospheric neutrino events in the fiducial volume with an efficiency of more than 99. The FC events in the fiducial volume are estimated to contain less than 1% background events. A measurement of the physical quantities of an event including vertex, the number of Cherenkov rings, momentum, particle identification, and the number of decay electrons, is automatically performed by the reconstruction algorithms with good quality. The fully-contained events in fiducial volume is divided based on the observed energy to sub-GeV, below 1.33 GeV, and multi-GeV, above 1.33 GeV. The multi-GeV events are used in this analysis. The selection efficiencies for this cut of energy are 86% for the ν_τ CC signal and 23% for the background respectively.

6

Atmospheric Tau Neutrino Appearance in Super-K

Super-K is credited for the discovery of neutrino oscillation by measuring a deficit in atmospheric muon neutrinos. In three-flavor neutrino oscillations, the deficit is explained by the change of muon neutrinos to tau neutrinos. An unambiguous measurement of tau appearance would be a direct evidence for three-flavor neutrino oscillations. The details of atmospheric tau neutrino appearance and the technique to measure it are presented in this chapter.

6.1 Atmospheric Tau Neutrino Appearance from Neutrino Oscillations

In three-flavor neutrino oscillations, tau neutrinos are expected to appear in the atmospheric neutrinos in the propagation of electron neutrinos and muon neutrinos. The probabilities of tau neutrino appearance from muon neutrino or electron neutrino in vacuum are calculated approximately as:

$$P(\nu_\mu \to \nu_\tau) = \cos^2\theta_{13}\sin^2(2\theta_{23})\sin^2(1.27\Delta m^2_{23}\frac{L}{E}) \tag{6.1a}$$

$$P(\nu_e \to \nu_\tau) = \sin^2(2\theta_{13})\cos^2(\theta_{23})\sin^2(1.27\Delta m^2_{23}\frac{L}{E}) \tag{6.1b}$$

Because neutrinos coming from below travel through the Earth, the oscillation probabilities are also altered by the matter effect. Instead of using the tau appearance probabilities in vacuum in Eq 4, a custom code by Wendell et al. (Wendell et al., 2012) is used to calculate the oscillation probabilties, which takes into account the effect of neutrino types, path lengths, neutrino energies and matter effect. The oscillation parameters used are $\sin^2 2\theta_{23} = 1.0$, $\Delta m^2_{23} = 2.1 \times 10^{-3} eV^2$ (Abe et al., 2013), $\Delta m^2_{21} = 7.6 \times 10^{-5} eV^2$ (Barger et al., 1980), $\sin^2 2\theta_{13} = 0.099$ (An et al., 2012; Ahn et al., 2012), $\delta_{CP} = 0$. The matter effect model from (Barger et al., 1980) is included in the calculation of oscillation probabilities. Fig. 6.1b presents the tau neutrino appearance probabilities from muon neutrinos and electron neutrinos in three-flavor neutrino oscillation under the assumption of normal hierarchy. Given a neutrino energy and a neutrino path length, the probability of a muon neutrino changing flavor to a tau neutrino is larger than that of electron neutrino. In addition, muon neutrinos have a larger flux than electron neutrinos (shown in Fig. 4.3). Therefore, tau neutrino appearance is dominantly from muon neutrino oscillation in atmospheric neutrinos.

By oscillating the electron neutrinos and muon neutrinos in the Honda flux prediction to tau neutrinos, we can calculate the expected atmospheric tau neutrino flux from neutrino oscillations at Super-K as

$$\Phi_{\nu_\tau}(E_\nu) = \int_{4\pi} \sum_{l}^{e,\mu} \Phi_{\nu_l}(E_\nu, \theta_z, \phi_A) O^{\nu_l \to \nu_\tau}(E_\nu, \theta_z, \phi_A) d\Omega \tag{6.2}$$

where $\Phi^{\nu_l}(E_\nu, \theta_z, \phi_A)$ is the differential flux as a function of neutrino direction $(\theta_z, \phi_z)$and neutrino energy (E_ν) for electron neutrinos or muon neutrinos from Honda model, $O^{\nu_l \to \nu_\tau}(E_\nu, \theta_z, \phi_A)$ is the probability of electron or muon neutrino changing flavor to tau neutrino as a function of neutrino direction and neutrino energy from Prob3++ (Wendell et al., 2012). Fig. 6.2 shows the expected atmospheric tau neutrino fluxes

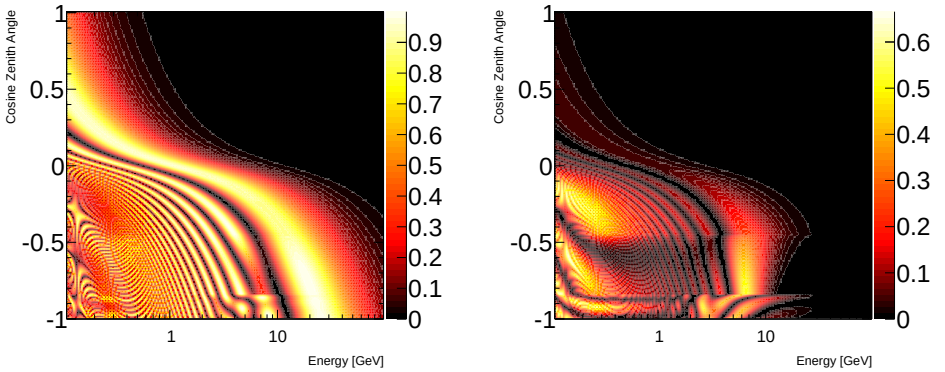

(a) Probability of muon neutrino changing flavor to tau neutrino as a function of neutrino energy and zenith angle.

(b) Probability of electron neutrino changing flavor to tau neutrino as a function of neutrino energy and zenith angle.

FIGURE 6.1: Probability of tau neutrino appearance from muon neutrinos (left) and electron neutrinos (right) as a function of neutrino energy and zenith angle.

from neutrino oscillations at Super-K integrated over neutrino directions.

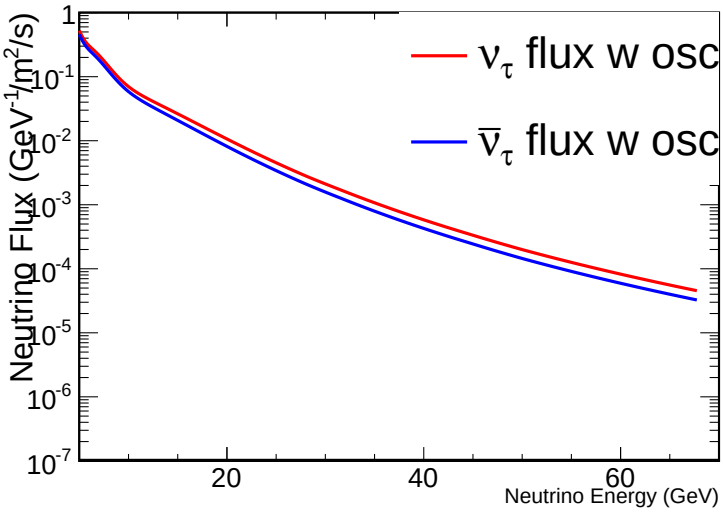

FIGURE 6.2: Flux of atmospheric ν_τ (red) and $\bar{\nu}_\tau$ (blue) from neutrino oscillations as a function of neutrino energy at Super-Kamiokande for the three-flavor oscillation parameters given in the text.

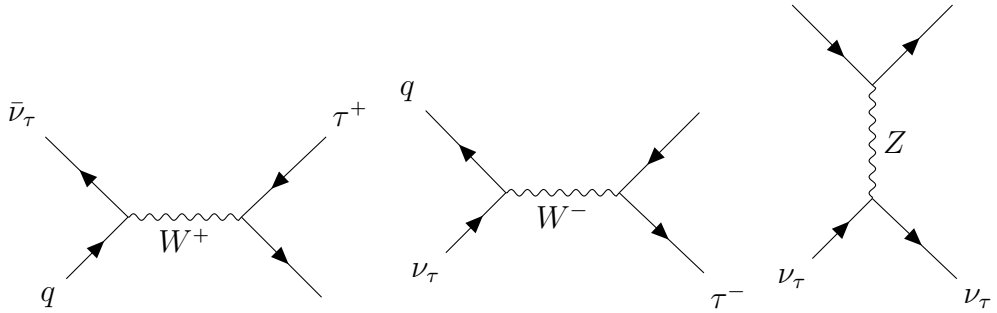

FIGURE 6.3: Feynman diagrams of weak interactions that include a tau neutrino.

6.2 Charged-current Tau Neutrino Events in Super-Kamiokande

Because the neutral-current interaction is flavor blind, it is not possible to distinguish the flavor of a neutrino in neutral-current interactions. However, a charged lepton of the same flavor as the neutrino is produced in the charged-current interactions. The detection of the charged lepton is an unambiguous confirmation of the neutrino flavor. Definite proof the appearance of tau neutrinos requires detection of tau leptons produced in charged-current tau neutrino interactions.

$$\nu_\tau + N \rightarrow \tau^- + N^{'} + \ldots \tag{6.3}$$

A charged-current tau neutrino interaction produces a tau lepton, which has a mass of 1.77 GeV/c^2 (Patrignani et al., 2016). The relatively large mass of the tau lepton greatly suppresses the cross section of charged-current tau neutrino cross section at low energies and results in an energy threshold of 3.5 GeV. The charged-current tau neutrino cross sections have been calculated by several groups (Jeong and Reno, 2010; Levy, 2009). In this study, we use the NEUT simulation package (Hayato, 2009) to model the neutrino cross section. Charged-current tau neutrino interactions are classified into three categories in NEUT: quasi-elastic charged-current interactions, charged-current resonant interactions and deep inelastic interactions.

By folding the flux with the cross sections, we can calculate the expected tau neu-

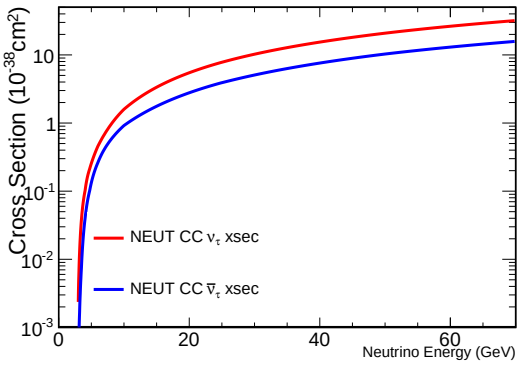

FIGURE 6.4: Total charged-current cross section as a function of neutrino energy for ν_τ (red) and $\bar{\nu}_\tau$ (blue) for neutrino energy between 3.5 GeV and 70 GeV in NEUT.

trino events in Super-Kamiokande. The charged-current tau neutrino cross sections suppressed by large tau lepton mass results in a low tau neutrino interaction rate, especially at typical atmospheric neutrino energies. Moreover, the tau neutrino flux from neutrino oscillations is smaller than that of electron neutrinos or muon neutrinos. Therefore, tau events are rare compared with the electron and muon neutrino events, which will be background in this analysis.

Tau leptons are also difficult to detect because of the extremely short lifetime of the tau lepton. The tau lepton decay has multiple channels, including leptonic decays and hadronic decays. The tau lepton decay channels with branching ratio larger than 1% are presented in Table 4.1 from (Patrignani et al., 2016). Leptonic decays of tau look similar to normal CC DIS interactions from ν_μ and ν_e. Multiple charged particles are produced in most hadronic tau decays. For this reason, the analysis is developed to select hadronic tau decays.

6.3 A Neural Network Algorithm for Tau Neutrino Identification

As described in Sec. 6.2, tau leptons produced in CC ν_τ interactions decay quickly to secondary particles, and the dominant hadronic decays produce extra pions. Because of the short lifetime of tau lepton, it is not possible to directly detect tau leptons in

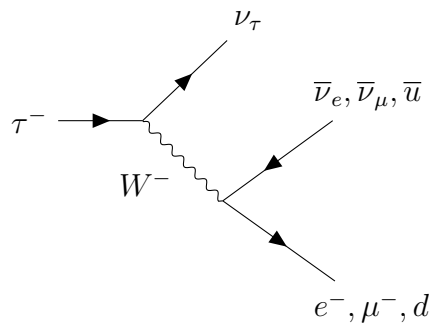

FIGURE 6.5: Feynman diagram of a tau lepton decay.

Super-K. The extra pions from the hadronic decays of the tau allow the separation of the signal from ν_μ and ν_e and NC background statistically. Fig. 6.6 compares the simulations of signal and background events in Super-K for example events. It is noted that the signal event has multiple rings produced by charged particles in water compared with a single ring in the background event. However, deep-inelastic neutrino interactions can also produce multiple charged particles in the detector that result in multi-ring patterns. Fig. 6.7 shows an example of background event that has a deep-inelastic interaction. The existence of deep-inelastic ν_μ/ν_e interactions results in the difficulty of identifying tau signal events. The signal events cannot be identified using a single variable in the standard Super-K reconstruction. The signatures of hadronic tau decays are reflected in several different reconstructed variables. In order to make use of multiple variables simultaneously in tau identification, a neural network is used in the analysis to look for extra pions from decays of heavy particles. The neural network, configured with TMVA package (Hocker et al., 2007) has seven input nodes, one hidden layer, and one output node.

6.3.1 Input Variables to the Neural Network

The seven input variables to the network are

- The log base 10 of the total visible energy (Evis) of the event.

  Evis is defined as the energy of a showering electron that produces the same

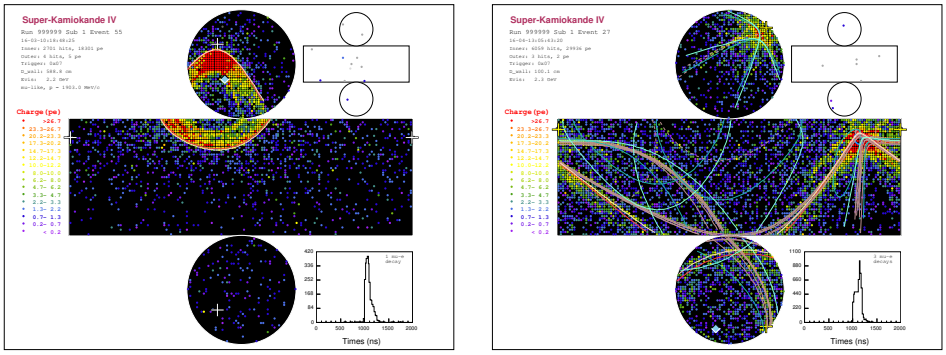

FIGURE 6.6: Simulation of a background (left) event with 2.2 GeV visible energy and a CC ν_τ event (right) with 2.3 GeV visible energy in Super-K, which produces multiple rings in the ID.

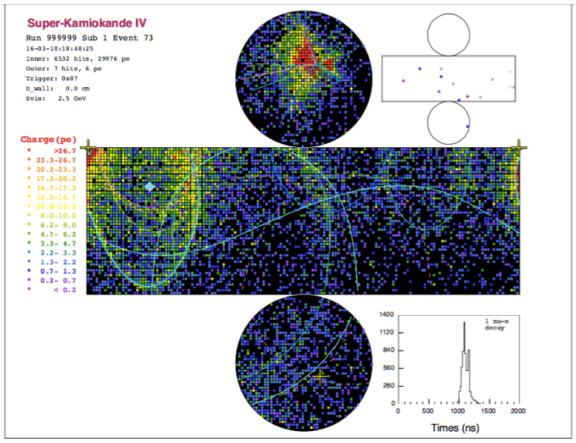

FIGURE 6.7: Simulation of a background event that has a deep-inelastic interaction, which produces multiple rings in the detector.

amount of observed Cherenkov light. Due to the energy threshold of CC ν_τ interactions and the large mass of tau lepton, the signal events are expected to have higher average visible energy than background events. The signal distribution peaks around 4 GeV in Fig. 6.8. By contrast, the background Evis spectrum falls with increasing Evis.

- The particle identification of the ring with maximum energy.

  Tau leptons decay quickly to daughter particles after production through lep-

tonic decays and hadronic decays. Except for the leptonic decay to a muon, most decay channels have at least one showering particle. A showering particle has a small value in the definition of particle identification likelihood, compared with a large value for a non-showering particle. The particle identification of the most energetic ring for signal has a distribution mostly in the negative (showering) region, while the background has a broad distribution in both negative and positive regions.

- The number of decay electron candidates in the event.

  Naively, we expect more pion decay electrons in signal events from the tau decays which are produced in hadronic tau decays. The variable does not depend on ring reconstruction, so it is relatively independent of most other variables.

- The maximum distance between the primary interaction point and any decay electron from a pion or muon decay.

  Energetic muons can travel a long distance in water. Therefore, CC ν_μ background involving a high energy neutrino is expected to have a large distance between the primary interaction point and the decay electron from the muon. In comparison, the pions from hadronic tau decay are expected to have smaller momentum, resulting in a smaller value of the variable.

- The clustered sphericity of the event in the center of mass system.

  Sphericity is a measure of how spherical an object is. A perfectly isotropic object has sphericity 1, while a perfectly one-directional object has sphericity 0. By defining a sphericity tensor, sphericity can be deduced.

$$S^{\alpha\beta} = \frac{\sum_i p_i^\alpha p_i^\beta}{\sum_i p_i^2} \tag{6.4}$$

where α,β= 1, 2, 3 are the three cartesian directions of the momentum vectors of the object, the sum is over the bins in geodesic space. Sphericity can be constructed by finding the eigenvalues, $\lambda_1 > \lambda_2 > \lambda_3$, of the tensor.

$$S = \frac{3}{2}(\lambda_2 + \lambda_3) \tag{6.5}$$

The hadronic decay of heavy tau lepton is more isotropic than a typical ν_μ or ν_e background. The spectrum of sphericity is centered near 1 for signal, while the spectrum has an almost flat distribution between 0.1 and 0.8. The background has a significant portion of events with large sphericity because of the high percentage of DIS at high neutrino energies.

- The number of possible Cherenkov ring fragments.

  A Hough transformation method is used to search for possible ring candidates in Super-K (Abe et al., 2013). By Hough transformation, the observed photoelectrons are mapped to a circle centered on the hit PMT. By accumulating the mapped circles, we can find peaks in the Hough space that are identified as centers of possible ring candidates. We expect more rings in signal because of the multiple charged particles and pions in hadronic tau decay.

- The fraction of total number of photoelectrons in the event carried by the first ring.

  This variable is the only one that has a different definition from that used in (Abe et al., 2013). A new variable is calculated with the charge in PMTs and the reconstructed vertex and direction of the event as

$$rfrac = \frac{\sum_{\theta_i<48^\circ} q_i}{\sum q_i} \tag{6.6}$$

  where θ_i is the angle between the reconstructed direction of the first ring and the direction of the reconstructed vertex to a PMT. The variable calculates

the ratio of charge within 48° of the direction of first ring in the event. The variable is expected to be smaller for the signal because the energy is carried by multiple particles in the tau hadronic decay. The variable is useful in the selection of deep inelastic neutral-current background from the charged-current background because energies are typically more equally divided into multiple particles than the charged-current background.

Because the oscillation-induced tau events come from below, the downward sample is expected to have no tau events. Therefore, the data and MC are compared in the downward-going sample to validate the agreement. Fig. 6.8 demonstrates the agreement between data and MC in the downward sample, along with the expected tau signal, for the seven variables.

6.3.2 Training and Testing the Neural Network

500 years of MC simulations for signal and background are used in the analysis. The MC samples are divided into three parts, one used to train the neural network, one used to test the neural network performance and one used in the analysis of data. Tau neutrinos from oscillations are expected to mostly come from below because of the path lengths in the earth. Because of this, the oscillation weight described in Sec. 2 will encode the up-down asymmetry to the signal MC that only upward-going events are selected. To select events based on event topology above and to avoid encoding up-down biases into the neural network, the training sample is weighted by the energy, as shown in Fig. 6.9, to cancel the up-down asymmetry in the oscillated MC. In this way, the upward and downward samples are treated the same in the training process, while the overall weight is still correct. The weights of the downward signal simulation are not set to zero, thereby preserving signal MC statistics.

The neural network is trained to classify a tau-like event with a NN output close to 1, and non-tau-like events have a NN output close to 0.

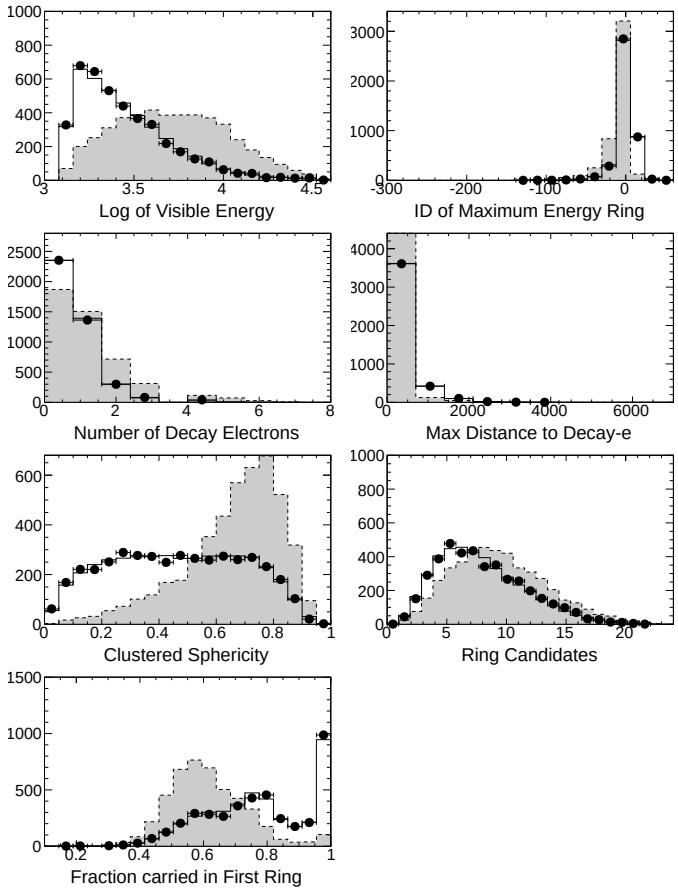

FIGURE 6.8: The input variables to the neural network for the downward MC (black histogram) and data (black dots), along with tau MC (gray shaded histogram).

Table 6.1: MC sample sizes for each stage of the MLP. The same statistics are used for SKI-IV.

	trainning	testing	analysis
Signal	∼25,000	1500	∼6,600 (100 yr.)
Background	32559	1500	∼82,000 (100 yr.)

Fig. 6.10 shows the NN output for background and signal simulations. The spectrum of NN for signal is clearly separated from the background. The trained NN is found to efficiently separate the CC tau signals from other background neutrino events. When selecting tau-like events from the events passing preselection cuts requiring the NN out greater than 0.5, 76% of signal events and only 28% of background remain. In the tau-like background, NC makes up 20% of the background. It

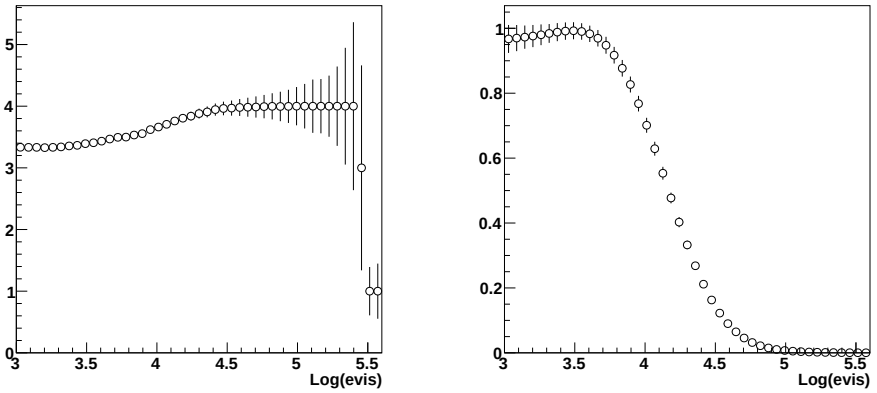

(a) Energy weights for background in the training sample.

(b) Energy weights for tau signal in the training sample.

FIGURE 6.9: Energy weights for the training sample.

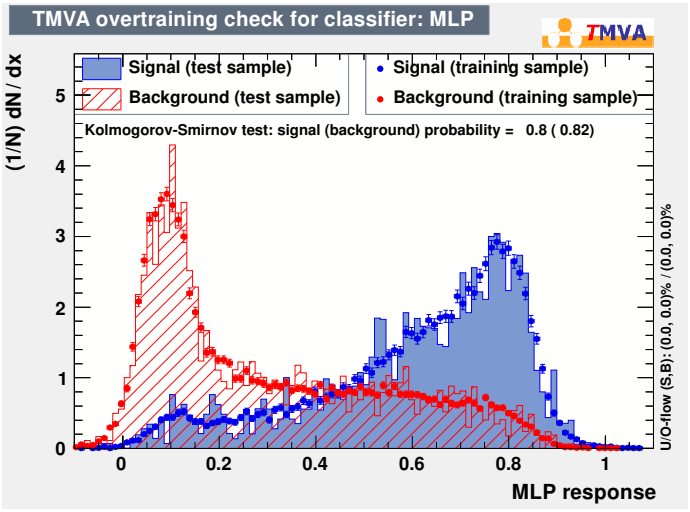

FIGURE 6.10: Neural network output of training (filled histogram) and test (dots) sample for background (red) and signal (blue) simulations.

is noted that multi-pion/DIS comprises 69% of the background. The neural network is configured to identify hadronic tau decays which typically have multiple pions, so the neural network also learns to idenfity multiple pion or DIS events. Table 6.2 summarizes the breakdown of the interaction modes in different samples.

By varying a cut on NN output, the efficiency of signal and background can be changed. The background efficiency is anti-correlated with the signal efficiency,

Table 6.2: The breakdown of interaction modes of both background and expected signal for the SK-I period. By cutting the NN output at 0.5, each mode is separated into tau-like and non-tau-like.

Interaction Mode	NN < 0.5	NN>0.5	All
CC ν_e	818.1	428.4	1246.5
CC ν_μ	1187.2	216.6	1403.8
CC ν_τ	12.5	39.4	51.9
NC	77.0	161.6	238.5

which is shown in Fig. 6.11. The efficiency of signal and background by cutting NN output is only plotted to assess the performance of the neural network in selecting tau events. No actual cut is performed in the analysis itself.

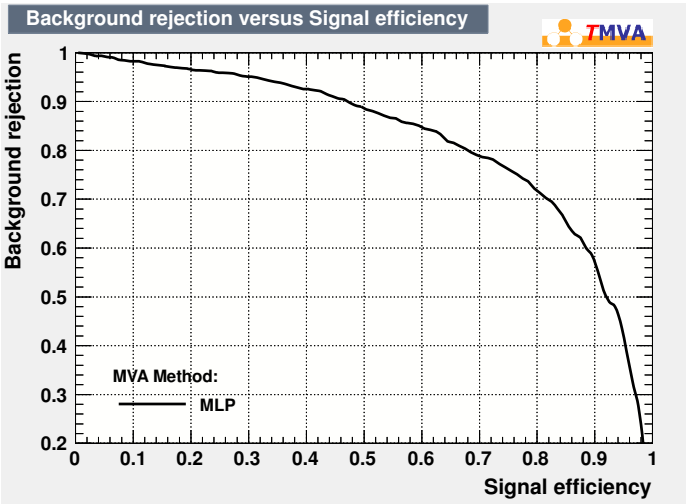

FIGURE 6.11: Efficiency of signal and background rejection by cutting the NN output in SK-IV.

Atmospheric tau neutrinos are expected in Super-K due to the neutrino oscillations. However, the detection of tau neutrinos is challenging because charged-current tau neutrino cross sections are suppressed by the relative large mass of the tau and the short lifetime of tau. A neural network algorithm has been developed to identify the events that have hadronic tau decays in Super-K, which shows good separation of charged-current tau neutrino events from other atmospheric neutrino events. The algorithm will be used in the following analyses.

7

Search for Tau Neutrino Appearance

In this chapter, we describe the measurement of tau neutrino appearance. The data are fitted against the PDFs built from MC simulations to measure a normalization factor which characterizes the tau appearance signal.

7.1 Fit the Tau and Background Normalization

In order to extract maximum information from the sample, the analysis uses a 2-dimensional unbinned likelihood fit. Using the neural network output and the reconstructed zenith angle of the events, two-dimensional particle distribution functions (PDFs) are built for background and tau signal. Fig. 7.1 is an example of the 2D distributions for oscillated signal on the left and background on the right. The horizontal axis of the plots is the cosine of the reconstructed zenith angle that is determined by the energy-weighted sum of the ring directions in the event. The vertical axis is the NN output, in which tau-like events have a value close to 1 and non-tau-like events have a value close to 0. The signal events (left panel) are primarily tau-like and come from below ($\cos(\theta)$ near -1), while the background events are more non-tau-like and come from all directions. The amount of signal and back-

ground events can be adjusted by varying the normalization of the distributions.

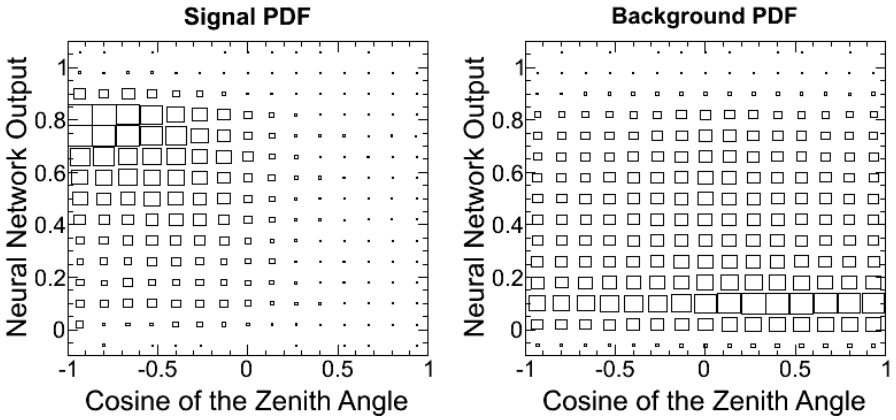

FIGURE 7.1: 2-dimensional probability distribution likelihood as a function of zenith angle and neural network output for tau (left) and background (right) built with MC.

DIS background events typically produce multiple pions as in the hadronic tau decays, thus are given high scores by the neural network tau identification. Therefore, DIS background makes up a large component of the tau-like background. Fig. 7.2 shows the DIS and non-DIS component in the background simulation.

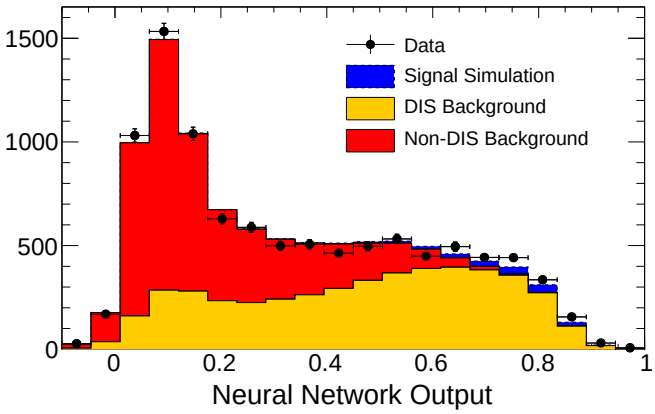

FIGURE 7.2: The breakdown of background simulation into DIS (orange) and Non-DIS (red) as a function of neural network output.

The average neutrino energy in the DIS interactions in our sample is 14 GeV. The DIS neutrino cross section in this region is not known to better than 10%.

In addition, the Bodek-Yang corrections (Bodek and Yang, 2002) implemented in our simulation of neutrino interactions tend to suppress DIS cross section at higher energies by about 5%. Because of the large portion of DIS component and the uncertainties of the interaction, we simultaneously fit the tau normalization with the DIS normalization with this uncertainty taken into account. The DIS error is introduced into the fit as a 10% Gaussian error constraint. The fit of the data is done to the sum of the signal and background PDFs varying the normalization,

$$Data = \alpha \times Signal + \beta \times (BG_{NonDIS} + \gamma \times BG_{DIS}), \tag{7.1}$$

where α, β and γ are the normalization of signal, non-DIS background and DIS background respectively.

Separate PDFs are produced for each Super-K run period for both signal and background. The data sets are fit both individually for each run period and jointly. Because of the low statistics of data events in the 2D distribution, we performed an unbinned likelihood fit with RooFit (Verkerke and Kirkby, 2003). The likelihood in the joint fit is constructed as

$$L(\alpha, \beta, \gamma) = \prod_{SK\,run}^{I-IV} \prod_{event\,i} f(NN, cos\theta; \alpha, \beta, \gamma) \frac{1}{0.1 \times \sqrt{2\pi}} e^{\frac{-(\gamma-1)^2}{2\times 0.1^2}} \tag{7.2}$$

where $f(NN, cos\theta; \alpha, \beta, \gamma)$ is the normalized probability density function (PDF) constructed with the likelihood from simulation as shown in Fig. 7.1. The likelihood is maximized by varying relative normalization of the three distributions, equivalent to minimizing

$$-\log[L(\alpha, \beta, \gamma)] = -\sum_{SK period} \sum_{event\,i} \log[f(NN, cos\theta; \alpha, \beta, \gamma)]. \tag{7.3}$$

A sensitivity study for the joint fit of all Super-K run periods is performed with toy MC generated with the signal and background PDFs, with α, β and γ set to be equal

to 1 in the study. 1,000 sets of toy MC were generated, and fit to extract the three parameters. The distribution of fit tau normalization is shown in Fig. 7.3. The tau normalization from the toy MC study has a Gaussian distribution centered at 1. The tau normalizations in the fit of toy MC are fitted with a Gaussian function, and the σ of the Gaussian fit is 0.24.

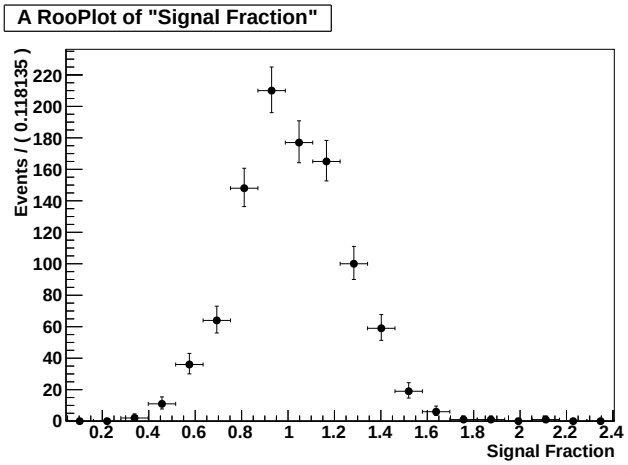

FIGURE 7.3: Tau normalization fit results with 2D unbinned likelihood fit of toy MC generated with $\alpha = 1$. The distribution has a σ of 0.24 with a Gaussian fit.

The data sets are fit individually and jointly for SK-I through SK-IV, and fit results are summarized in Table 7.1, and are compared with the results from (Abe et al., 2013). The tau normalization in the joint fit is 1.37 with statistical uncertainty of 0.23.

Table 7.1: Data fit results of tau normalization, background normalization and DIS background normalization in each Super-K period.

	α	α in (Abe et al., 2013)	β	γ
SK-I	1.25±0.42	1.27±0.49	0.89	1.11
SK-II	1.65±0.54	1.47±0.62	0.87	1.18
SK-III	1.99±0.70	2.16±0.78	0.86	1.09
SK-IV	1.57±0.35	-	0.88	1.11
Total	1.37±0.22	1.42±0.35	0.86	1.18

The statistical uncertainty is 16% in the data fit, better than 24% of the fit results of the toy MC study. The smaller uncertainty is due to the fitting of a tau

normalization to a value larger than 1 in the data fit. Another set of toy MC is generated with $\alpha = 1.37$, $\beta = 1$ and $\gamma = 1$. The tau normalization is fit in the new study, and the distribution of tau normalizations is shown in Fig. 7.4, which has a statistical error of 0.26. The statistical error in the new MC study is similar to that in the data fit.

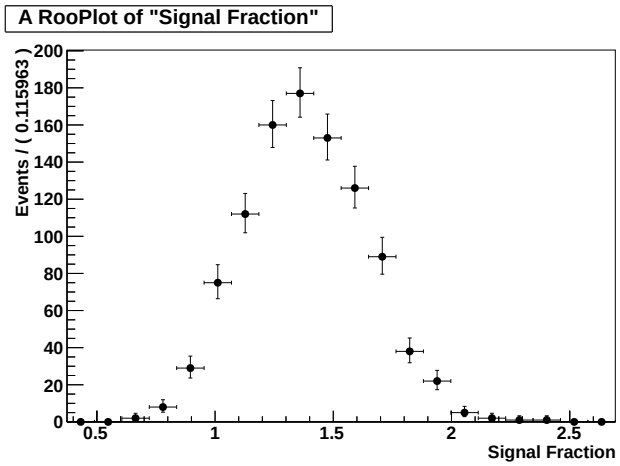

FIGURE 7.4: Fit of tau normalization in toy MC study with tau normalizations set to 1.37 in the toy MC generation. The distribution is centered at 1.37, and the fit of the distribution with a Gaussian function found a σ of 0.26.

To examine the results of the combined fit graphically, binned projections in zenith for both tau-like (NN output >0.5) and non-tau-like (NN output < 0.5) events, and the projections in NN output for both upward-going ($\cos(\theta) > 0.1$) and downward-going ($\cos(\theta) < 0.1$) events are shown in Fig. 7.5. The 2D PDFs of signal and background are projected into 1D and have been rescaled to the fitted normalization values. Good agreements are seen in all distributions. As expected, the tau neutrino signal shows up in the upward-going direction. The PDFs and data from all Super-K periods are combined in these plots.

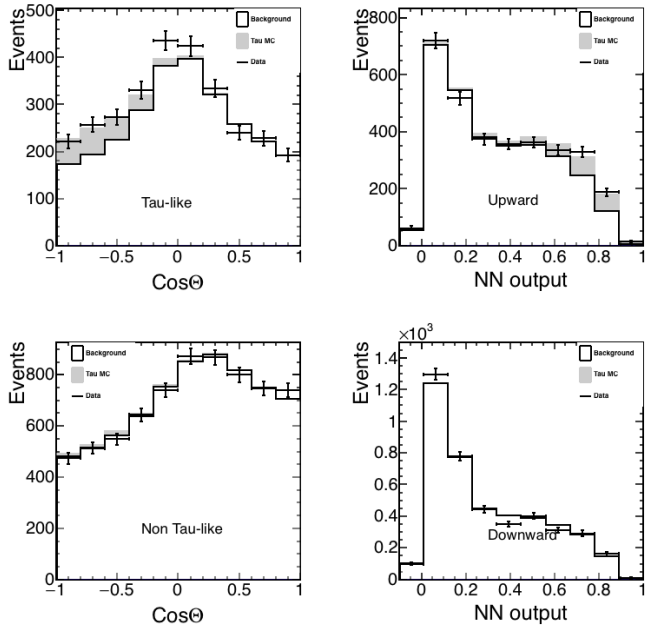

FIGURE 7.5: Fit results showing the projections in NN output and zenith angle distribution for tau-like (NN > 0.5), upward-going ($\cos(\theta) > 0.1$), non-tau-like (NN < 0.5) and downward-going ($\cos(\theta) < 0.1$) events for both the two-dimensional PDFs and data. The PDFs have been rescaled by the fit results. The PDFs and data sets have been combined from SK-I through SK-IV. The fitted tau signal is shown in gray.

7.2 Systematic Errors

A subset of systematic uncertainties in atmospheric neutrinos is taken into account. In total, there are 56 systematic uncertainties, 18 for the atmospheric neutrino flux, 18 for neutrino interactions, 15 for detector response and reconstruction and 5 oscillation parameter uncertainties. Out of the 56 uncertainties, 40 are common among SK-I through SK-IV, while the other 16 are dependent on Super-K run period. A brief description of the systematic uncertainties is presented below.

Atmospheric Neutrino Flux

1. **Absolute normalization**

   The uncertainty of the absolute flux normalization is given by Honda flux model (Honda et al., 2015). It is an energy-dependent error as shown in Fig.

7.6, where scaling factors for below and above 1 GeV independently scale the flux according to the function shown. Additionally, 5% normalization error on multi-GeV events is considered in order to account for the differences above 10 GeV between the Honda flux model (Honda et al., 2015) and other flux models such as FLUKA (Battistoni et al., 2003) and Bartol (Gaisser, 2013).

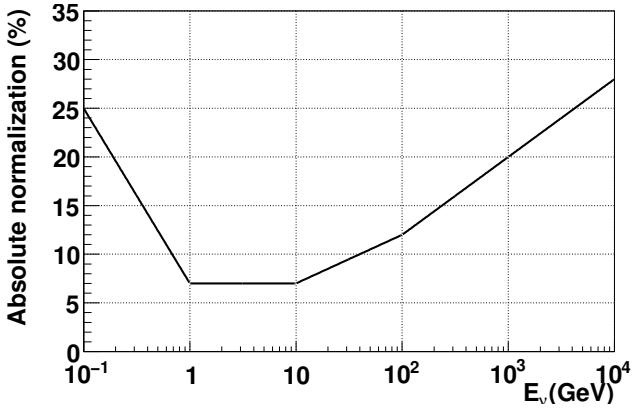

FIGURE 7.6: Uncertainty on the absolute flux normalization as a function of neutrino energy.

2. **Flux Ratios**

The uncertainties on the various flux ratios are estimated by comparing the Honda flux (Honda et al., 2015) to the FLUKA (Battistoni et al., 2003) and Bartol (Gaisser, 2013) flux models. The flavor ratio $(\nu_\mu + \bar{\nu}_\mu)/(\nu_e + \bar{\nu}_e)$ in FLUKA and Bartol model normalized by Honda flux is shown in Fig. 7.7. The uncertainty is estimated to be 2% for $E_\nu < 1$ GeV, 3% for 1 GeV $< E_\nu <$10 GeV, 5% for 10 GeV$< E_\nu < 30$ GeV, then linearly increasing as a function of $\log_{10} E_\nu$ to 30% at 1TeV.

The uncertainty on the anti-neutrino to neutrino ratio comes from π^+/π^- and K^+/K^- ratio in hadronic interaction of the flux calculation. For the $\bar{\nu}_e/\nu_e$ ratio, it is estimated to be 5% for $E_\nu < 10$ GeV, 8% for 10 GeV $< E_\nu <$100 GeV, then linearly increasing as a function of $\log_{10} E_\nu$ to 30% at 1 TeV. For the

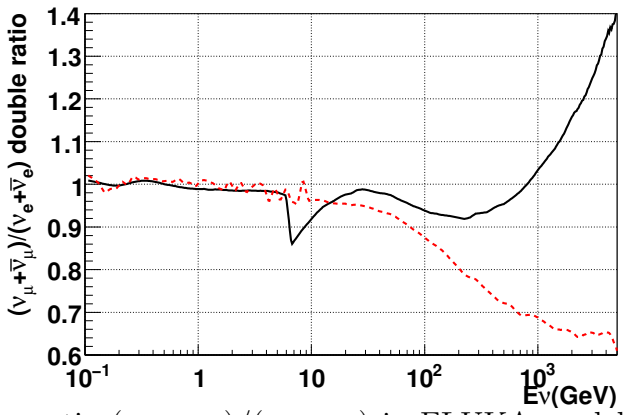

FIGURE 7.7: Flavor ratio $(\nu_\mu + \bar{\nu}_\mu)/(\nu_e + \bar{\nu}_e)$ in FLUKA model (solid) and Bartol model (dashed) normalized by Honda flux model.

$\bar{\nu}_\mu/\nu_\mu$ ratio, it is estimated to be 2% for $E_\nu < 1$ GeV, 6% for 1 GeV $< E_\nu <$50 GeV, then linearly increasing as a function of $\log_{10} E_\nu$ to 60% at 1TeV. The comparison of $\bar{\nu}/\nu$ ratios between Honda flux and other models is shown in Fig. 7.8.

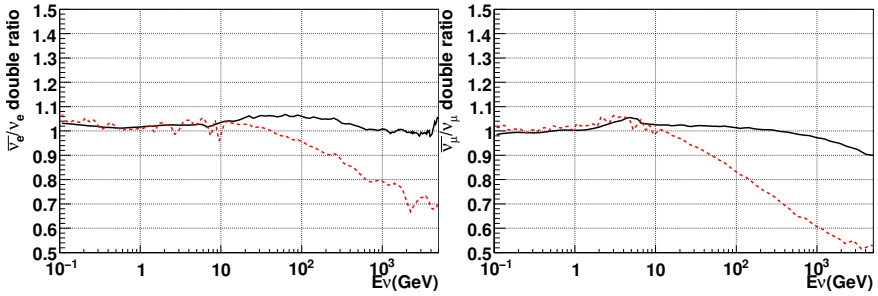

FIGURE 7.8: Anti-neutrino/neutrino ratio normalized by ratio in Honda flux model for $\overline{\nu}_e/\nu_e$ (left) and $\overline{\nu}_\mu/\nu_\mu$ (right) for FLUKA (solid) and Bartol (dashed) models.

The uncertainty on up/down ratio is due to the geomagnetic field. The uncertainty on horizontal/vertical ratio is mainly caused by the three-dimensional calculation method in different flux models for neutrino energy below 3 GeV. For neutrino energy above 3 GeV, it is caused by the difference in the calculated the K/π ratio in the hadronic interactions in the atmosphere. Both uncertainties are estimated by comparing the zenith angle distributions using

the three flux models.

3. K/π **Ratio**

   Atmospheric neutrinos below 10 GeV are mainly produced by pion decays. However, kaon contributions become important as the energy increases. The SPY experiment measured the K/π production ratio with an accuracy of 3% in proton interactions with beryllium for K and π momentum ranging from 7 GeV/c to 135 GeV/c (Ambrosini et al., 1998). Based on this measurement and the correlation between hadron momentum and neutrino energy, the uncertainty on neutrino flux due to K/π ratio is estimated to be 5% for E_ν below 100 GeV, linearly increasing to 20% at E_ν =1 TeV, and 20% for E_ν above 1 TeV.

4. **Solar Activity**

   Primary cosmic rays are affected by the solar activity that periodically changes in a 11-year cycle. The variation of neutrino flux caused by a $\pm$ 1 year variation in the solar cycle is assigned as an uncertainty on the flux, which is 20% for SK-I, 50% for SK-II, 20% for SK-III, and 10% for SK-IV.

5. **Neutrino Path Length**

   The production height of atmospheric neutrinos depends on the density of the atmosphere, and the uncertainty affects the oscillation probability calculation. For upward-going events, the uncertainty produces a negligible effect. For events near or above the horizon, it is treated as a systematic error. A 10% uncertainty on the atmosphere density structure is given by comparing the US-standard 76 (NOAA and Force, 1976) and MSISE-90 (Hedin, 1991) models for the atmosphere, and the resulting change in the production heights of atmospheric neutrinos is propagated to the calculation of neutrino oscilla-

tions. Fig. 7.9 compares the neutrino path length as a function of zenith angle calculated with the atmosphere density in Honda model and the atmosphere density compressed by 10%.

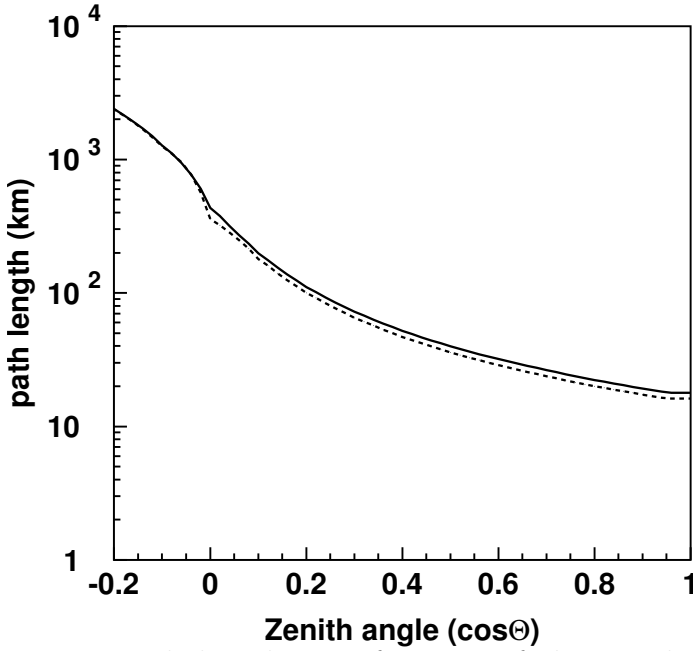

FIGURE 7.9: Neutrino path length as a function of the zenith angle calculated with the atmosphere density in Honda model (solid) and the atmosphere density compressed by 10% (dashed). Taken from (Lee, 2012)

6. **Matter Effect**

Although the matter density structure of the Earth is well measured by (Dziewonski and Anderson, 1981), there is an uncertainty on the chemical composition of the Earth core. The electron density that depends on the chemical composition of the Earth core affects the oscillation probability calculation. Therefore, the uncertainty needs to be taken into account. The Earth core is assumed to consist of mostly heavy elements such as iron, which has a electron density about 6.8% less than that of light elements. The electron density in the Earth core is estimated to be 6.8% smaller and is considered during the calculation of oscillation probabilities.

Neutrino Interactions

1. **CCQE Cross Section**

   The cross sections of charged-current quasi-elastic scattering (CCQE) is calculated based on the Smith-Moniz CCQE model (Smith and Moniz, 1972) with a Relativistic Fermi Gas (RFG) nuclear model. The differences of the model from Nieves model (Nieves et al., 2004) are assigned as the uncertainties of the total cross section as well as the cross section ratios $\bar{\nu}/\nu$ and $(\bar{\nu}_\mu + \nu_\mu)/(\bar{\nu}_e + \nu_e)$.

2. **Axial Mass**

   The Super-K neutrino interaction MC has been generated at axial mass M_A=1.2 GeV. A 10 % uncertainty on the axial mass is assumed in the analysis.

3. **MEC**

   The meson exchange current models (MEC) have large uncertainties, and their cross sections have not been explicitly measured. 100% uncertainty is assigned to the total cross section of the MEC process.

4. **Single Meson Production**

   The uncertainty on the single meson production cross section is estimated to be 20% by comparing the model calculation with the experimental data of $\nu_\mu + p \rightarrow \mu^- + p + \pi^+$ measurement. Because of the lack of measurement of $\nu_\mu + p \rightarrow \mu^- + p + \pi^0$, the uncertainty on its cross section is estimated by comparing the base model in NEUT to the model from (Hernandez et al., 2008). The comparison of the theoretical cross sections is shown in the left panel of Fig. 7.10. The double ratio of the $\bar{\nu}/\nu$ cross sections, shown in the right panel of Fig. 7.10, is also taken as an systematic uncertainty in the single meson production. The ratio between the π^0 production to the charged pion production is estimated to be 40% and is taken as the systematic error.

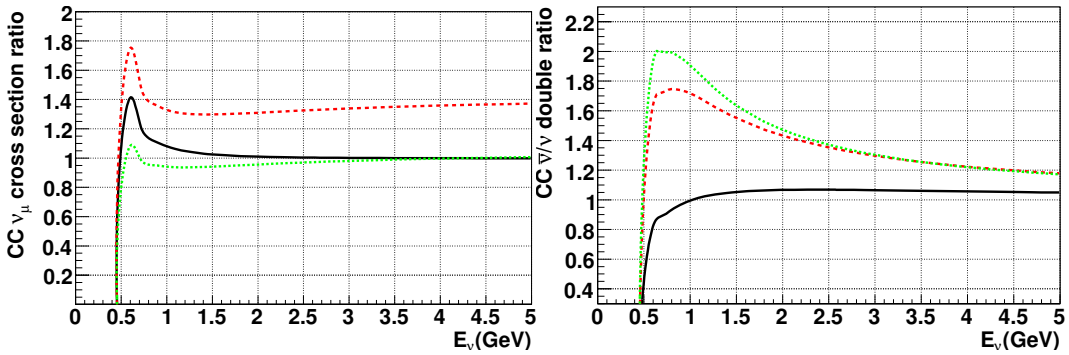

FIGURE 7.10: The Hernandez model normalized by the base model in NEUT for $\nu_\mu p \rightarrow \mu^- p\pi^+$ (solid line), $\nu_\mu n \rightarrow \mu^- p\pi^0$ (dashed line) and $\nu_\mu n \rightarrow \mu^- p\pi^+$ (dotted line) are shown in for the theoretical cross sections (left) and the double ratio for $\bar{\nu}/\nu$ ratio (right). Figure is taken from (Lee, 2012).

The uncertainties on the parameters that characterize the Graczyk-Sobczyk form factor (Graczyk and Sobczyk, 2008) were given by bubble chamber experiments data (Wilkinson et al., 2014).

5. **Deep Inelastic Scattering Cross Section**

   The theoretical calculation of DIS cross section agrees with experimental measurements better than 5% for energies above 10 GeV, but the discrepancy is larger in low energy region (<10 GeV). A 10% uncertainty is assigned to the cross section. Moreover, the application of Bodek-Yang correction tends to suppress the DIS cross section by about 5%. An additional uncertainty is taken as the difference between the base model of GRV98 with the Bodek-Yang correction with CKMT model (Capella et al., 1994).

   Also, the uncertainty on the Q^2 spectrum of the DIS interaction is given by the difference between the GRV98 model with and without the Bodek-Yang correction. Separate uncertainties are assigned to regions of W<13 GeV/c^2 and W>13 GeV/c^2, where W is the invariant mass.

6. **Coherent Pion Production**

For CC ν_e and NC coherent pion production, 50% uncertainty is assigned by comparing the difference between the SciBooNE measurement (Nakajima, 2011) and the Rein and Sehgal model. As SciBooNE had observed no evidence of CC ν_μ coherent pion production, 100% uncertainty is assigned to its cross section.

7. **NC/CC Ratio**

   The uncertainty on NC/CC ratio is estimated to be 20%.

8. **Nuclear Effect in ^{16}O Nucleus** The uncertainty on pion final state interactions is estimated by comparing the NEUT simulation with external experiment data (de Perio, 2011). The cross sections of these final state interactions are varied with a weighing method while keeping the difference between the reweighted simulation from the experiment data less than 1σ, as shown in Fig. 7.11. The uncertainty on the nuclear effect in ^{16}O nucleus is given by the difference between the minimum weight and maximum weight on each simulated event.

Detector Response and Reconstruction

1. **FC Reduction**

   The uncertainty on FC reduction efficiency is estimated to be 0.2% for SK-I, 0.2% for SK-II, 0.8% for SK-III and 0.3% for SK-IV by comparing the distributions of each cut variable in data and MC. Background contamination in each run period is described in Section 5.1.

2. **FC/PC separation**

   NHITAC, defined as the number of hits in the OD, is used to separate FC and PC events, and the uncertainty on the separation is estimated by the difference of NHITAC distribution between the data and MC.

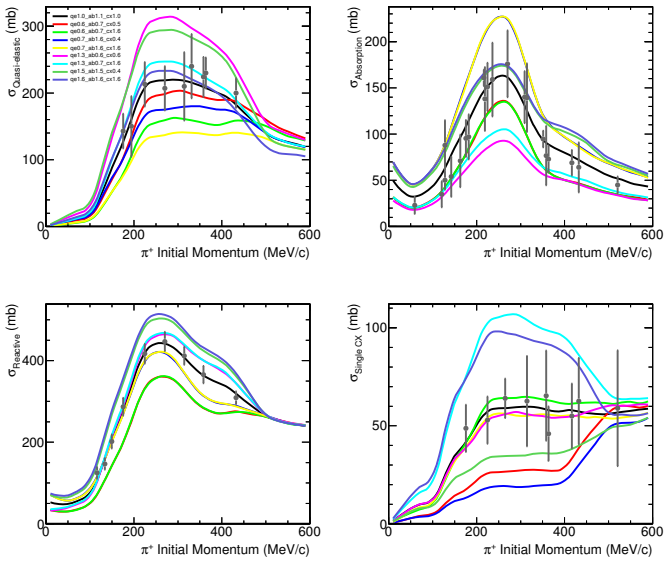

FIGURE 7.11: Re-weighted simulation of π^+ scattering on carbon target with NEUT and experimental data in: quasi-elastic channel (top left), absorption channel (top right), total reaction channel (bottom left) and single charge exchange channel (bottom right). Taken from (Lee, 2012).

3. **Fiducial Volume**

   The uncertainty on the fiducial volume is estimated to be 2%, corresponding to the change in fiducial volume with a inward/outward shift of the vertex position by $\sim$ 10 cm near the fiducial boundary.

4. **Ring Counting**

   The ring separation error is considered by examining the differences in the distributions of ring-counting likelihood between the data and MC.

5. **Particle Identification**

   Particle identification errors are estimated similarly by comparing the distributions of e/μ likelihood ratio between the data and MC. The errors are estimated separately for single-ring and multi-ring events.

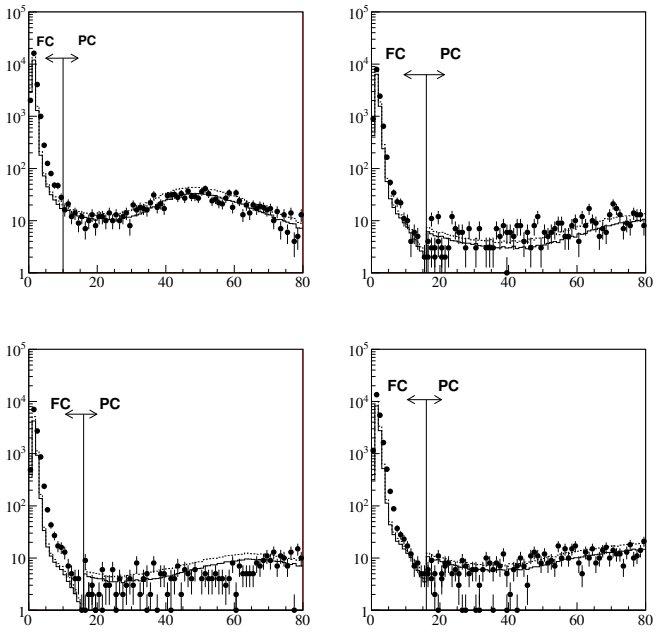

FIGURE 7.12: NHITAC distributions for FC and PC final samples for SK-I (top left), SK-II (top right), SK-III (bottom left) and SK-IV (bottom right). Data are shown by dots with error bar, MC events assuming no oscillation are shown with dashed lines and MC with $\nu_\mu \to \nu_\tau$ 2-flavor oscillation with ($\sin^2 2\theta$, Δm^2) = (1.00, 2.5×10^{-3} eV^2) are shown with solid lines.

6. **Energy Calibration**

   Energy scale errors are described in Section 3.6. The error on the absolute energy scale is estimated to be 1.1% for SK-I, 1.7% for SK-II, 2.7% for SK-III, and 2.3% for SK-IV. The up/down asymmetry of the energy scale is also evaluated from the momentum of decay electrons with different directions and 0.3% uncertainty is assigned.

7. **Decay Electron Tagging**

   The uncertainty on decay electron detection efficiency is estimated to be 1.5% for SK-I to SK-III and 0.8% for SK-IV. In addition, π^+ decay probability uncertainty is taken into account, which ranges between 3% and 13% depending

on the π^+ momentum.

Oscillation Parameters

1. $\sin^2(\theta_{23})$ and Δm^2_{23} are varied within 1σ limits of a combined SK-I+SK-II+SK-III atmospheric oscillation result assuming normal mass hierarchy (Abe et al., 2013). The Δm^2_{32} is varied between 1.92×10^{-3} and 2.22×10^{-3} eV^2, $\sin^2 2\theta_{23}$ is varied between 0.93 and 1.0.

2. The $\sin^2(\theta_{13})$ values are varied within our combined Daya Bay (An et al., 2012) and RENO (Ahn et al., 2012) results of $\sin^2 2\theta_{13} = 0.099 \pm 0.014$.

7.2.1 Individually Estimate Systematic Uncertainties

The systematic errors in the atmospheric neutrino analysis (Wendell et al., 2010) are reevaluated, and 28 systematic errors are included in this method. The systematic errors are updated regularly. The values of systematic errors that are common in four Super-K run periods are summarized in Table 7.2. Table 7.3 shows the systematic errors that are dependent on Super-K run periods.

Table 7.2: Systematic errors used in tau neutrino appearance search that are common to all Super-K run periods. 1σ size of the systematic error is shown as a percentage.

Systematic error			σ(%)
Flux normalization	$E_\nu > 1$GeV		7
$\bar{\nu}_e/\nu_e$ ratio			
	1 GeV $< E_\nu < 10GeV$		3
	$E_\nu > 10GeV$		5
$\bar{\nu}_\mu/\nu_\mu$ ratio			
	1 GeV $< E_\nu < 10GeV$		5
	$E_\nu > 10GeV$		8
$\bar{\nu_\mu}/\nu_e$ ratio			
	1 GeV $< E_\nu < 10GeV$		6
	$E_\nu > 10GeV$		6
Up/down ratio			
	Multi-GeV	e-like	0.7
		μ-like	0.2

	Multi-ring Sub-GeV	μ-like	0.2
	Multi-ring Multi-GeV	e-like	2.8
		μ-like	1.5
horizontal/vertical ratio			
	Multi-GeV	e-like	0.7
		μ-like	0.2
	Multi-ring Sub-GeV	μ-like	0.2
	Multi-ring Multi-GeV	e-like	2.8
		μ-like	1.5
K/π ratio in flux			10
Neutrino path length			10
sample by sample normalization	FC Multi-GeV		5
MA in QE and single π			10
CCQE cross section			1.0
Single meson production cross section			20
DIS model difference			1.0
DIS cross section			5
Coherent π production			100
NC/CC ratio			20
Nuclear effect in pion spectrum			30
CCQE $\nu/\bar{\nu}$ ratio for ν_e			10
CCQE cross section μ/e ratio			10
$\pi^0/\pi^{\pm}$ ratio			40
single pion production $\bar{\nu}/\nu$ratio			10
Hadron simulation			10

The effect of an individual systematic error on expected signal and background is calculated by reweighting every event in simulations after shifting the systematic error value from the central value by $+1\sigma$/-1σ. The neural network is re-trained with the reweighted MC, and the data are re-classified with the new network. The PDFs are updated with distributions of the reweighted and reclassified MC. The unbinned likelihood fit is repeated with the reprocessed data and new PDFs. The difference of the refitted tau normalization with systematic error shift from the tau normalization with systematic errors at the central value is calculated as the uncertainty from this systematic error term. By iterating the process for each systematic error one at a time, the systematic uncertainties of tau normalization are estimated for

Table 7.3: Systematic errors used in tau neutrino appearance search that are independent between Super-K run periods. 1σ size of the systematic error is shown as a percentage.

Systematic error	SK-I	SK-II	SK-III	SK-IV
solar activity	20	50	20	10
FC reduction	0.2	0.2	0.8	0.3
Multi-GeV e-like BG	0.1	0.1	0.4	0.1
Multi-GeV mu-like BG	0.1	0.1	0.2	0.8
PID for single-ring e-like	0.2	0.2	0.3	0.4
PID for single-ring mu-like	0.2	0.3	0.3	0.4
PID for multi-ring e-like	6.5	9.7	4.5	3.3
PID for multi-ring mu-like	2.9	3.8	2.7	1.6
Energy calibration	1.1	1.7	2.7	2.3
up/down symmetry for energy calibration	0.6	0.6	1.3	0.3
fiducial volume	2	2	2	2

each systematic error for both plus 1σ and minus 1σ. The central value of the tau normalization is taken as the fit result without changing systematic errors, which does not change in the estimation of systematic errors. The changes in fitted tau normalization after shifting the systematic errors are summarized in Table 7.4.

Table 7.4: Change in fitted tau normalization after shifting systematic error by $+1\sigma/-1\sigma$.

Systematic Error	$+1\sigma$ (%)	-1σ (%)
$\nu/\bar{\nu}$ ratio for $E_\nu > 1$GeV	2.5	-2.6
$\nu_e/\bar{\nu}_e$ ratio for $E_\nu > 1$GeV	0.2	-0.1
$\nu_\mu/\bar{\nu}_\mu$ ratio for $E_\nu > 1$GeV	1.2	-1.1
up/down ratio	3.3	-3.3
horizontal/vertical ratio	-4.8	4.8
K/π ratio	1.9	-1.9
neutrino path length	0.1	-0.1
absolute neutrino E>1GeV	7.7	-9.0
relative norm	4.7	-5.1
axial mass	4.8	-5.7
CCQE cross section	-1.9	1.8
single meson	3.3	-3.8
DIS model difference	-7.1	6.2
coherent pi	1.0	-1.0
NC/CC ratio	2.5	-2.9

nuclear pi spectrum	0	0
CC ν_τ cross section	-25.0	25.0
FC reduction	0.3	-0.3
hadron simulation	0.01	-0.01
non ν_e background	0.01	-0.01
non ν background	0.1	-0.1
PID 1 ring	0.1	-0.1
PID multi-ring	2.4	-2.7
energy calibration	2.0	-1.9
up/down energy calibration	2.3	-2.2
solar activity	1.0	0.8
CCQE $\nu/\bar{\nu}$ ratio	0.8	-0.8
CCQE ν_μ/ν_e ratio	-0.3	0.3
$\pi/\pi^\pm$ ratio	-2.8	2.7
$\bar{\nu}/\nu$ 1 pi ratio	-0.4	0.5
$\nu/\bar{\nu}$ ration $1GeV < E < 10GeV$	0.6	-0.7
$\nu_e/\bar{\nu}_e$ ration $1GeV < E < 10GeV$	0.0	0.3

The systematic errors are divided into two sets. The first set includes the systematic errors used to quote the error on the expected number of tau events, which does not affect the significance of the measured tau normalization. The tau cross section error, which is 25% error, is the largest in this set. The error on the tau cross section was estimated by comparing the charged-current tau neutrino cross sections in NEUT with several other theoretical models, especially the difference between NEUT and cross section model by (Hagiwara et al., 2003). Detector biases on selection and fitting are also included in this set, but are small compared to the tau cross section uncertainty.

The second set of errors would affect the observed signal but not the background, or the significance of the tau normalization in the fit. The five errors in this set are all expressed as ratios: upward to downward neutrino flux, horizontal to vertical neutrino flux, kaon to pion originated neutrino flux, NC to CC cross section and the upward to downward detector energy scale difference. The dominant error on the signal is the horizontal/vertical ratio changing the fitted number of tau events of

about $\pm 5\%$.

The systematic errors of the oscillation parameters are also included in the errors which can change the measured results and significance. In this study, they are varied within the 1σ limit of a combined SK-I+SK-II+SK-III atmospheric oscillation analysis result assuming the normal hierarchy (Abe et al., 2013). The Δm^2_{32} is varied between 1.92×10^{-3} and 2.22×10^{-3} eV^2, $\sin^2 2\theta_{23}$ is varied between 0.93 and 1.0. The θ_{13} value is varied within the world average result of $\sin^2(2\theta_{13}) = 0.099 \pm 0.14$ in (Patrignani et al., 2016). Due to the small uncertainty of θ_{13}, the variation in θ_{13} around this central value results in less than 1% change in the fit result. However, the use of non-zero θ_{13} value results in a 14% reduction of the fitted tau normalization because three-flavor oscillations produce high energy upward-going electron neutrino in the expected background thus reducing the needed number of tau neutrinos to explain the signal region. Varying the value of δ_{cp} results in less than 1% change in the fitted number of tau events. Therefore, the value of δ_{cp} is set to zero in this analysis, and the uncertainty is neglected.

Table 7.5: Summary of errors of oscillation parameters.

Systematic uncertainties of ν_τ events	+%	-%
Δm^2_{32}	2.4	-4.5
$\sin^2(2\theta_{23})$	-	-4.6
$\sin^2(2\theta_{13})$	0.5	-0.7

The systematic errors are summarized in Table 7.6. Combining the systematic errors on the observed tau events, the measured value of tau normalization is $1.37 \pm 0.23^{+0.13}_{-0.11}$. The expected number of tau events in the fiducial volume is 230.9 with combined systematic errors of $(+28.7 - 29.1\%)$. After rescaling the MC by the fitting factors and corrections for efficiency, the observed number of tau events fit for the entire running period is calculated to be $316.3 \pm 53.1^{+30.0}_{-25.4}$.

The observed number of tau events is converted to the significance level for reject-

Table 7.6: Summary of systematic errors for both the expected and measured number of ν_τ events. The errors for each category have been added in quadrature.

Systematic uncertainties of ν_τ events	+%	-%
Super-K atmospheric ν oscillation errors		
28 error term (expected events)	14.0	14.9
5 error terms (observed events)	7.0	7.1
Tau neutrino cross section (expected events)	25.0	25.0
Oscillation parameters (observed events)	6.5	2.4

ing the non-tau-appearance hypothesis. The measured signal normalization with a normalization of zero corresponds to the hypothesis of no-tau-appearance. A normalized asymmetric Gaussian function centered at 1.37 is constructed with the combined error of measured tau normalization as shown in Fig. 7.13. A p value calculated as the integral of the function below 0 is calculated to be 1.1×10^{-8}, corresponding to a significance level of 5.1σ.

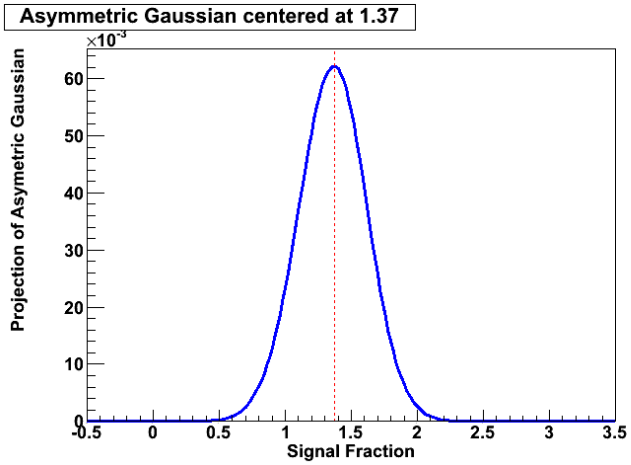

FIGURE 7.13: An asymmetric Gaussian function is constructed with the fitted tau normalization and it uncertainty. The significance of tau appearance is calculated by integrating the negative part of the function.

If the inverted hierarchy is chosen in calculating the oscillation probabilities instead of the normal hierarchy, the expected number of θ_{13}-induced upward-going electron neutrino background is reduced, resulting in a higher fitted value (1.56) and corresponding to a higher significance.

7.2.2 Simultaneous Fitting of the Tau Normalization and Systematic Errors

In the above method, the tau normalization is fit with the systematic errors at the central value, and the systematic errors are estimated individually and added in quadrature. The correlation between signal and systematic errors and correlation within systematic errors are thus neglected in the fit. To address the problem, a new fit method is developed to simultaneously fit the tau normalization and the systematic errors. This new method is more accurate and conservative. The fit method is also based on RooFit. The systematic errors in Super-K atmospheric neutrino analysis (Abe et al., 2013) are taken into account in the fit. PDFs for signal and background are built as described in the above subsection for each run period, but the DIS component is not built separately. PDFs for systematic errors are built out of two-dimensional histograms prepared from the MC simulation and the three-flavor oscillation software (Osc3++) (Wendell et al., 2010). Osc3++ has a function to calculate the change of event distribution for a 1σ change in an individual systematic error. Using the function, we calculate the change of the two-dimensional event distribution of zenith angle and neural network output for each systematic error. Assuming the systematic coefficients have a linear effect on the bin content in the two-dimensional distribution, the PDF of each systematic error is calculated as the difference of distributions between $\pm\sigma$.

$$PDF_i = \frac{(PDF_{BG}(+\sigma_i) + PDF_{\tau}(+\sigma_i)) - (PDF_{BG}(-\sigma_i) + PDF_{\tau}(-\sigma_i))}{2}, \quad (7.4)$$

where $PDF_{BG(\tau)}(\pm\sigma_i)$ is the two-dimensional event distribution for signal (background) after shifting the systematic error by $+1\sigma/-1\sigma$. An example of two-dimensional distribution for 1σ change is shown in Fig. 7.14. The data are fitted to the summation of background PDF, signal PDF and systematic PDFs varying the

normalizations.

$$Data = PDG_{BG} + \alpha \times PDF_{tau} + \sum \epsilon_i \times PDF_i, \tag{7.5}$$

Instead of only fitting one signal normalization and two background normalizations,

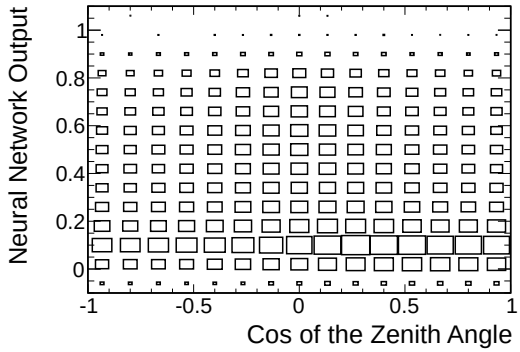

FIGURE 7.14: An example histogram of the PDF of K/π ratio uncertainty for SK-I background. The vertical axis is the output of the NN; the horizontal axis is the cosine of the event zenith distribution.

the new method includes coefficients of all systematic errors and normalization of signal distribution into the fit. An unbinned likelihood fit of data is done to the sum of the signal, background and systematic uncertainty PDFs by varying the overall normalizations. The likelihood is a function of tau normalizations and magnitudes of systematic errors where the magnitude of every systematic error has a Gaussian error constraint.

$$L(\alpha, \epsilon_0, \epsilon_1, \ldots, \epsilon_m) = \prod_{SK}^{I-IV} \prod_{run\ event\ i} f(NN, cos\theta; \alpha, \epsilon_0, \epsilon_1, \ldots, \epsilon_m) \prod_{0}^{m} \frac{1}{\sqrt{2\pi}} e^{-\epsilon_i^2/2}, \tag{7.6}$$

where $\epsilon_0, \epsilon_1, \ldots, \epsilon_m$ are the magnitudes of the m systematic errors and PDF_i is the PDF for each systematic error built with the MC simulations.

All the systematic errors from atmospheric neutrino oscillations, except the uncertainty of CC tau neutrino cross section, are taken into account in the fit. The tau cross section uncertainty is excluded because it affects the overall normalization

of tau events, which acts the same as α in the fit. The uncertainties of oscillation parameters can also change the measured results and significance, which are fitted together. $\sin^2(2\theta_{23})$ and Δm^2_{23} are varied between 1σ limits of Super-K result (Abe et al., 2013), and $\sin^2(2\theta_{13})$ is varied between 1σ limit of reactor neutrino measurements (Beringer et al., 2012).

Toy MC is generated with the PDFs, and the fit of tau normalization in the toy MC is shown in Fig. 7.15. The fraction of toy MC with negative fitted tau normalization is calculated to be 3.6×10^{-4}.

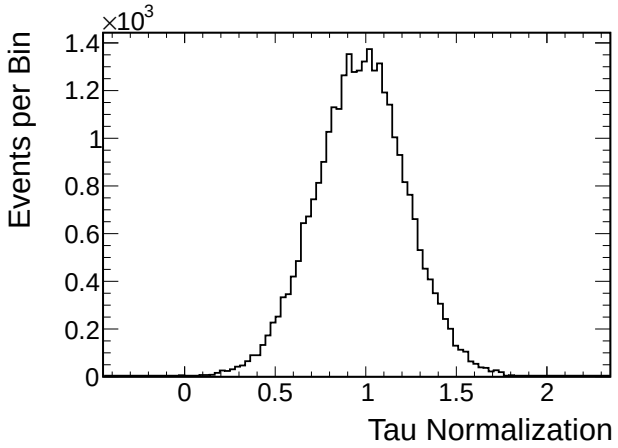

FIGURE 7.15: Tau normalization in toy MC generated and fitted with all atmospheric neutrino analysis systematic errors, which is centered at 1.0 and has a p value of 3.6×10^{-4}.

However, some of the systematic errors cause tiny or even no change in the event distributions after shifting the systematic error, meaning that these systematic errors have a small effect in this fit. An example of two-dimensional distribution for such a systematic error is shown in Fig. 7.16, in which the fractional change in the two-dimensional event distribution is less than 0.1%. To exclude these negligible systematic errors in the fit, the systematic errors for this analysis are selected by cutting on the maximum fractional change in any bin of the two-dimensional histograms. A series of toy MC's are generated by varying the cut value, and the tau

normalization is fit in the toy MC's. By requiring the significance level for rejecting no-tau-appearance to be the same as the result without cutting on the systematic errors in the toy MC, we can select the maximum cut value to remove unrelated systematic errors. Fig. 7.17 demonstrates the distribution of fitted tau normalizations in the toy MC after selecting the systematic errors with the maximum cut value of 2.5%. The p value in the distribution is 4.4×10^{-4}, corresponding to a significance level of 3.3σ. The significance level of rejecting no-tau-appearance in the toy MC changes to 3.8σ (p=6.0×10^{-5}) when selecting the systematic error with a cut value of 3%. Therefore, the systematic errors used in the analysis are selected by requiring that the maximum fractional change in the bins of two-dimensional histograms not be less than 2.5%. The fitted tau normalization in the toy MC generated and fitted with selected systematic errors and uncertainties of oscillation parameters is shown in Fig. 7.17.

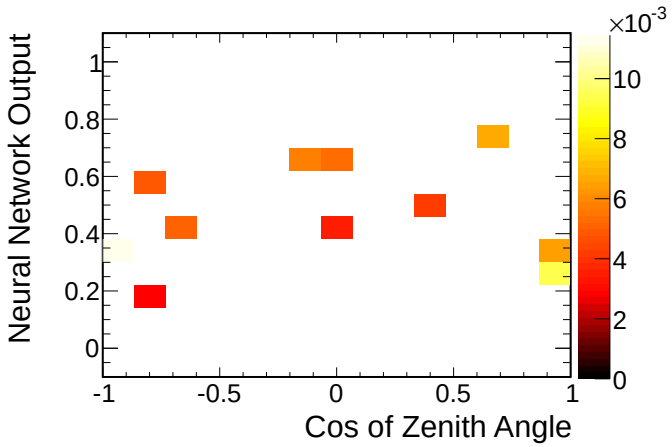

FIGURE 7.16: Histograms of the PDFs for uncertainty on absolute normalization of neutrino flux below 1 GeV that causes small change in event distributions in SK-I. The color demonstrates the change of events number in the bin after shifting the systematic error by 1σ.

The fit is performed jointly with all data periods being fit at the same time. Relative to the expectation of unity, the tau normalization is fitted to be 1.47$\pm$ 0.32 (stat+syst) in the joint fit, corresponding to a 4.6σ rejection of the no-tau-appearance

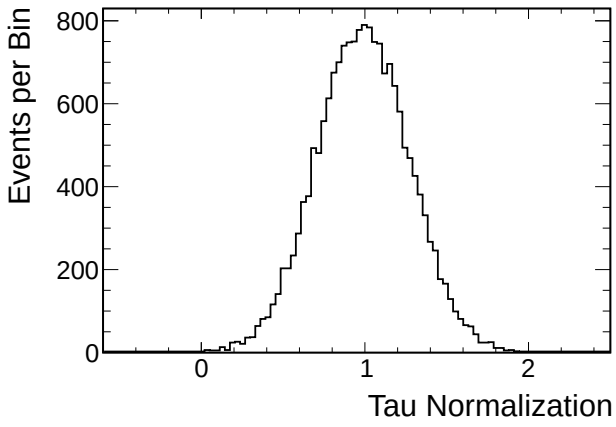

FIGURE 7.17: Tau normalization in toy MC generated and fitted with selected atmospheric neutrino analysis systematic errors, which is centered at 1.0 and has a p value of 4.4×10^{-4}.

hypothesis. This result is less significant than that of the quadratic summation of systematic errors because of the more conservative method of simultaneous fitting tau normalization and systematic errors. The fitted values and sizes of systematic errors in the analysis are summarized in Table 7.7 for the systematic errors common in Super-K run periods and Table 7.8 for systematic errors independent between Super-K runs. Fig. 7.18a illustrates the distribution of the values of fitted systematic errors. In order to evaluate the fitted systematic errors, we use a variable defined as

$$E_{cor} = \frac{E_{fit} - E_{input}}{s_{fit} - s_{input}}, \tag{7.7}$$

where E_{cor} is the value of systematic error after correction. E_{fit} (E_{input}) is the value of the systematic error in the fit (input) and s_{fit} (s_{input}) is the 1σ size of the systematic error in the fit (input). The corrected errors are shown in Fig. 7.18b.

The results of the final combined fit are examined graphically by plotting the binned projections of the fitted results. Fig. 7.19 demonstrates the projection in zenith angle for both tau-like (NN output > 0.5) and non-tau-like (NN output <0.5) events, along with the projections in NN output for both upward-going ($\cos(\theta) > 0.1$)

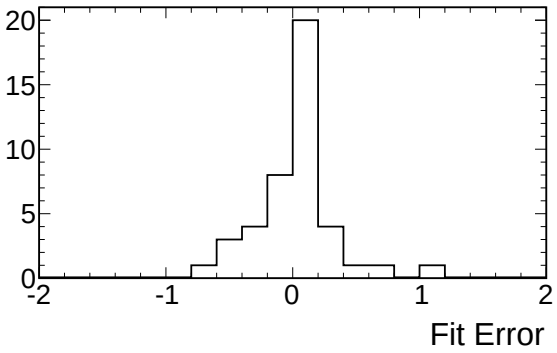

(a) Distribution of the fitted values of systematic error from the fit.

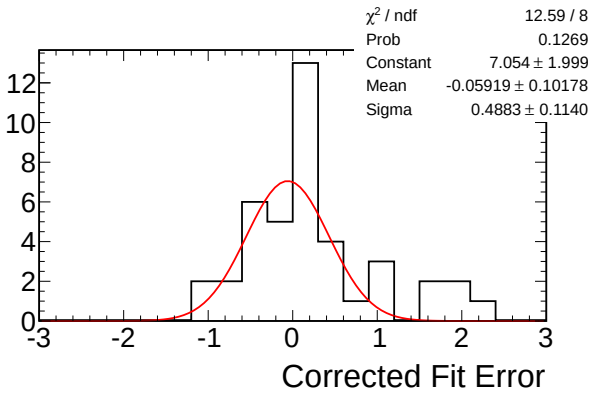

(b) Distribution of the variable defined in Equation 7.7. The distribution is expected to have a Gaussian distribution with a width of 1.

FIGURE 7.18: Fitted values of systematic error in simultaneous fit of tau normalization and systematic errors.

Table 7.7: Fit results for common systematic errors in all Super-K run periods in simultaneous fit of tau normalization and systematic errors.

Systematic error	fit mean	fitted uncertainty
CCQE $\nu/\bar{\nu}$ ratio	6.8×10^{-4}	0.98
CCQE cross section ratio	0.10	0.48
DIS model difference	-0.51	0.37
DIS cross section	0.20	0.47
K/π ratio	0.01	0.66
NC/CC ratio	0.22	0.44
Flux normalization ($E_\nu > 1$GeV)	-0.04	0.48
coherent π cross section	-0.03	0.59
DIS q^2 dependence for low W	1.03	0.49
DIS q^2 dependence for high W	-0.27	0.45
1π CAaa5 error	-0.41	0.43
1π axial coupling	-0.68	0.35
1π background scale factor	-0.23	0.59
horizontal/vertical ratio	0.01	0.57
Δm^2_{23} error	-0.14	0.59
matter effect	0.003	0.70
meson exchange on/off	0.05	0.44
$\nu/\bar{\nu}$ ratio ($E_\nu > 10GeV$)	0.03	0.7
$\bar{\nu}_e/\nu_e$ ratio ($E_\nu > 10GeV$)	0.008	0.7
neutrino path length	-3.8×10^{-4}	1.36
single-pion $\bar{\nu}/\nu$ ratio	0.002	0.04
$\bar{\nu}_\mu/\nu_\mu$ ratio ($E_\nu > 10$ GeV)	0.09	0.69
single pion $\pi^0/\pi^\pm$ ratio	0.15	0.43
sample by sample normalization FC multi-GeV	-0.07	0.4
$\sin^2(\theta_{23})$	0.19	0.66
single meson cross section	-0.17	0.68
$\sin^2(2\theta_{13})$	0.02	0.98

Table 7.8: Fit result of systematic errors that are independent between Super-K run periods in the simultaneous fit tau normalization and systematic errors.

Systematic error	SK-I		SK-II		SK-III		SK-IV	
	Mean	uncertainty	Mean	uncertainty	Mean	uncertainty	Mean	uncertainty
1-ring e-like background	0.01	1.35	0.01	1.30	0.31	1.29	-0.04	1.34
multi-ring e-like background	0.32	0.83	0.66	0.88	0.33	1.07	0.26	0.70
ring separation	0.01	1.19	-0.41	1.24	-0.08	1.35	-0.36	1.30
multi-ring PID	0.18	0.81	0.52	0.67	-0.26	1.1	0.1	0.98

and downward-going ($\cos(\theta)$ <0.1) events. In these plots, the signal PDFs have been rescaled to the fitted normalization values, and PDFs of systematic errors for signal and background have been rescaled by the fitted magnitudes of systematic errors and added to signal and background respectively. The fitted tau signal is shown in gray. All distributions have good agreement between data and MC simulations. In these plots, the PDFs and data from all of the run periods are combined.

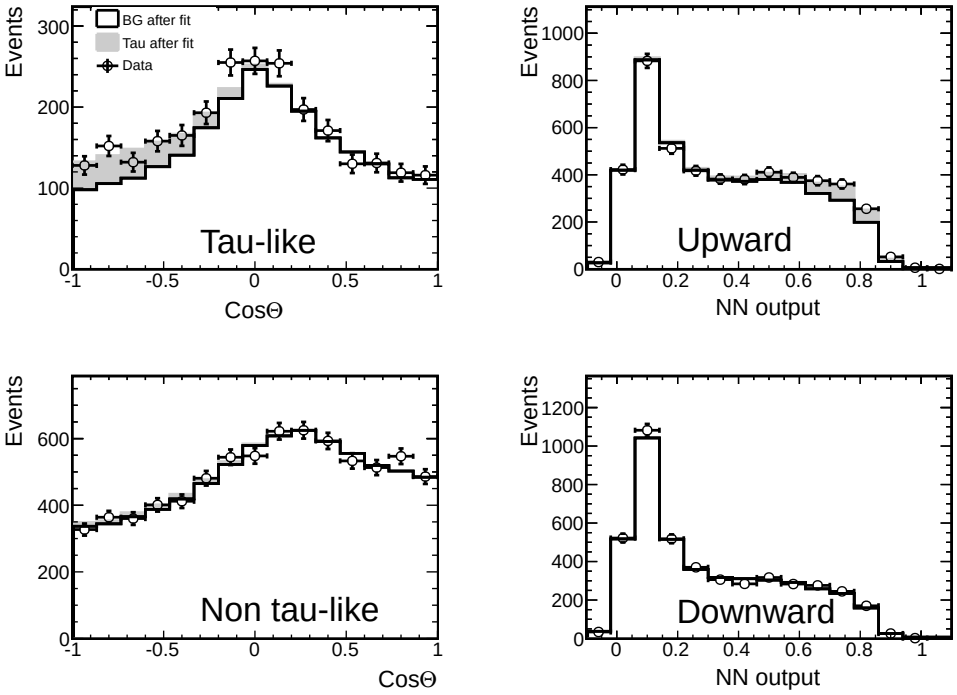

FIGURE 7.19: Fit results showing projections in the NN output and zenith angle distribution for tau-like (NN>0.5), upward-going [$\cos(\theta)$ >0.1], non-tau-like (NN <0.5) and downward-going [$\cos(\theta)$ <0.1] events for both the two-dimensional PDFs and data. The PDFs and data sets have been combined from SK-I through SK-IV. The fitted tau signal is shown in gray.

A significance level of 3.3σ is expected for the nominal expected signal, which is smaller than the measured result. The larger significance of the measurement is due to the fact that more signal was measured than expected. Another set of toy MC is generated with 1.47 times the expected signal, and the fitted tau normalization in the toy MC is shown in Fig. 7.20. The significance level has increased with more signal

than nominally expected. Because of the enormous amount of computing required to generate toy MC for the p value calculation, the significance level is determined by fitting the distribution of fitted tau normalizations in the toy MC by a Gaussian function. The fitted Gaussian function in centered at 1.47 with a width of 0.30, corresponding to a significance level of 4.9σ, which is in relative good agreement with the measured result.

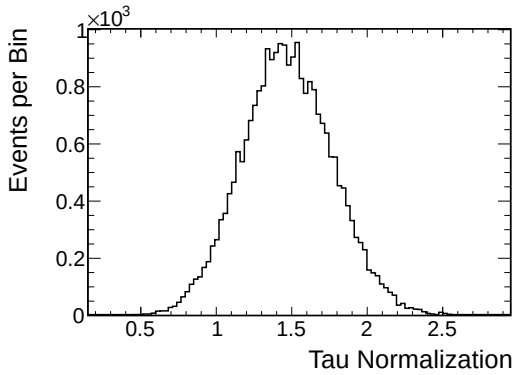

FIGURE 7.20: Distribution of the fitted tau normalization in toy MC generated with 1.47 times of the nominal expected tau events.

The fit is repeated with inverted hierarchy when calculating the oscillation probabilities, resulting in a reduction in the expected number of θ_{13}-induced upward-going electron neutrino. Under the assumption of inverted hierarchy, the fit results in a higher fitted value (1.57 ± 0.31) and a correspondingly higher significance (5.0σ).

8

Charged-current Tau Neutrino Cross Section Measurement

In this chapter, we describe the measurement of charged-current tau neutrino cross sections using atmospheric tau neutrino events in Super-K. The result is compared to the measurement of the DONUT experiment.

8.1 Charged-current Tau Neutrino Cross Section Measurement

In the tau neutrino search, we developed a neural network algorithm to identify tau events and measure the number of tau events in Super-K. By scaling the theoretical cross section in the MC simulations to match the data, we can measure the inclusive charged-current tau neutrino cross section in water.

$$\sigma_{measured} = S_\tau \times \langle \sigma_{theory} \rangle, \tag{8.1}$$

where S_τ is the factor that is used to scale the theoretical cross section to match simulations and data. $\langle \sigma_{theory} \rangle$ is the theoretical cross sections used in MC simulations. We have already fitted a normalization factor to match data and MC simulation with a two-dimensional unbinned likelihood fit in the last section, which can be used to

scale the theoretical cross section. The scale factor can be also obtained by counting the number of tau events in the data to be compared with the expected number of tau events in the MC simulations, which is basically an alternative one-dimensional fit of data against MC. The two methods will be discussed and compared in the following subsections.

8.1.1 Charged-current Tau Neutrino Cross Section Measurement Based on Two-dimensional Fit of Tau Normalization

In the tau neutrino search, the normalization of tau events is fitted to be 1.47±0.32 with systematic errors taken into account. This normalization matches the data and MC simulations by scaling up the overall normalization of two-dimensional tau distributions. Therefore, the normalization factor can also be converted to a charge-current tau neutrino cross section by scaling the theoretical cross sections in the MC simulation with the factor,

$$\sigma_{measured} = (1.47 \pm 0.32) \times \langle \sigma_{theory} \rangle, \tag{8.2}$$

Here, $\langle \sigma_{theory} \rangle$ is a flux-averaged theoretical charged-current tau neutrino cross sections included in NEUT. To calculate it, we need to convolute the differential tau neutrino cross sections as a function of neutrino energy with the energy spectrum of atmospheric tau neutrinos from neutrino oscillations, which have been discussed in Sec. 3 and Sec. 2 respectively. $\langle \sigma_{theory} \rangle$ is calculated as follows:

$$\langle \sigma_{theory} \rangle = \frac{\sum_{\nu_\tau, \bar{\nu}_\tau} \int \frac{d\Phi(E_\nu)}{dE_\nu} \sigma(E_\nu) dE_\nu}{\sum_{\nu_\tau, \bar{\nu}_\tau} \int \frac{d\Phi(E_\nu)}{dE_\nu} dE_\nu}, \tag{8.3}$$

where $\frac{d\Phi(E_\nu)}{dE_\nu}$ is the differential flux of tau neutrinos as a function of neutrino energy, $\sigma(E_\nu)$ is the differential charged-current tau neutrino cross sections used in NEUT simulation. $\frac{d\Phi(E_\nu)}{dE_\nu}$ has been obtained from integrating the Honda flux over directions in Sec. 2, and $\sigma(E_\nu)$ is extracted from NEUT simulation. To calculate $\langle \sigma_{theory} \rangle$, we

need to choose the energy range of the integral in Eq. 8.3, which is the neutrino energy range of interest in our measurement. Fig. 8.1a shows the energy spectrum of tau events in MC simulation in SK-I through SK-IV after weighting by oscillation probabilities and live time. In the MC simulations, tau events have an energy range spanning from 3.5 GeV, the threshold energy of charged-current tau neutrino interactions, to energies more than 60 GeV. However, it is noted that tau events with energy more than 60 GeV are rare. The number of tau events is integrated for events with energy more than a specific value in simulation to determine the maximum energy of expected tau events. Fig. 8.1b shows the integral of the tau neutrino events with energies more than the energy value in the horizontal axis. The integral of events becomes less than 1 at the energy value of 67 GeV, meaning that less than one tau event is expected with more than 67 GeV energy after selection. The neutrino energy region of interest in the analysis is between 3.5 GeV and 67 GeV. The upper edge of the energy region is rounded to 70 GeV.

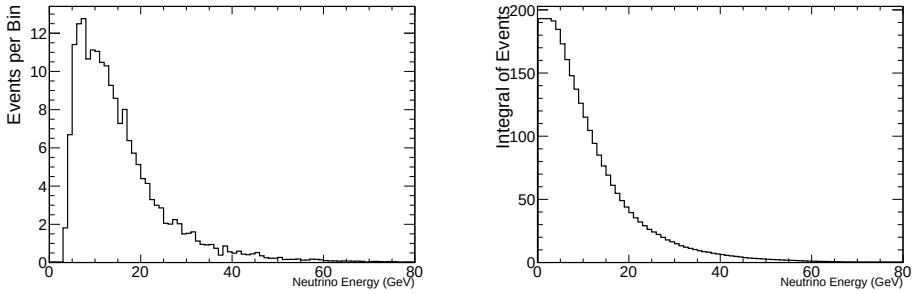

(a) Energy spectrum of expected tau events for 5326 days of live time.

(b) Integral of events shown in the left plot as a function of minimum energy.

FIGURE 8.1: Energy spectrum of tau neutrino events after selection in SK-I through SK-IV simulation after weighting by oscillation probabilities and live time (left), and integral of number of events in the left plot with energy above the energy value in the bin (right).

Given the theoretical cross section and tau neutrino energy spectrum by oscillating the electron and muon neutrinos to tau neutrinos, the flux-averaged theoretical

charged-current tau neutrino cross section is calculated between 3.5 GeV and 70 GeV to be 0.64×10^{-38}cm^2. Fig. 8.2 shows the theoretical charged-current tau neutrino cross sections in NEUT and tau neutrino fluxes as a function of neutrino energy by oscillation electron and muon neutrinos in Honda model prediction to tau neutrinos. The flux-averaged charged-current tau neutrino cross section is shown by the gray dashed line.

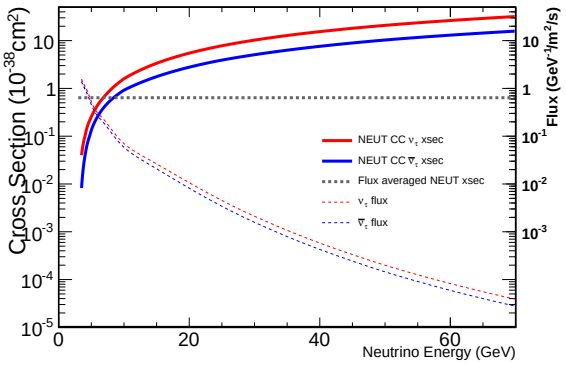

FIGURE 8.2: Theoretical charged-current tau neutrino cross sections (solid lines) as a function of neutrino energy for ν_τ (blue) and $\bar{\nu}_\tau$ (red), atmospheric tau neutrino flux (dashed lines) from neutrino oscillations by oscillating the electron and muons neutrinos in HONDA model prediction to tau neutrinos for ν_τ (blue) and $\bar{\nu}_\tau$ (red) and flux-averaged tau neutrino cross section (gray dashed line).

Based on Eq. 8.2, the flux-averaged charged current tau neutrino cross section is measured to be $(0.94 \pm 0.20) \times 10^{-38}$cm^2. The measured cross section is shown together with the theoretical cross sections and the MC simulations in Fig. 8.3. The center and range of the energy axis (10^{+25}_{-5} GeV) is calculated from the 90% range of the MC simulations after selection in Sec. 4, and the uncertainty on the cross section axis ($0.94\pm0.20\times10^{-38}$cm^2) is from the uncertainty in the fit of tau normalization.

8.1.2 Comparing the Number of Measured Tau Events with Expectation

Instead of using the tau normalization in the two-dimensional fit, S_τ in Eq. 8.1 can also be calculated from comparing the observed tau events with the expected tau

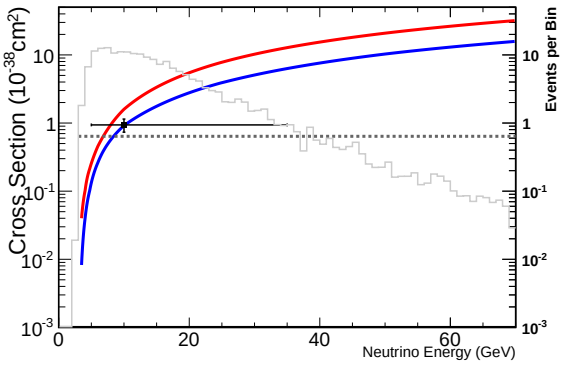

FIGURE 8.3: Measured flux-averaged charged-current tau neutrino cross section (black), together with theoretical differential cross sections (ν_τ in blue and $\bar{\nu}_\tau$ in red), flux-averaged theoretical cross section (dashed gray) and tau events after selection in MC simulations (gray histogram).

events as follows

$$S_\tau = \frac{N_{tot}^{obs} - N_{BG}^{exp}}{N_\tau^{exp}} \tag{8.4}$$

where N_{tot}^{obs} is the total number of events in the sample after selection, N_{BG}^{exp} is the number of background events in the MC simulations after selection, and N_τ^{exp} is the number of tau events in the MC simulations after selection.

The samples used in the tau appearance search have pre-selections, and the tau neutrino concentration is only 1.8% in the MC after pre-selections. The statistical and systematic uncertainties arising from the background are overwhelmingly larger than N_τ^{exp}, resulting in large statistical and systematic errors in the measured S_τ. Therefore, multiple cuts are applied on the sample used in the tau neutrino search to enrich the tau signal.

- Cosine of zenith angle is less than -0.2. Tau neutrinos are expected mostly in the upward-going sample, while background events show up in all directions. The cut removes more than half of the background, but keeps most of the tau signal events.

- Neural network output larger than 0.54 (0.54 is the bin edge closest to 0.5 in the two-dimensional PDF histograms). As shown in Fig. 6.10, tau events tend to have neural network value close to 1 with background events having values close to 0. The cut further increases the tau purity in the sample.

Table 8.1 summarizes the number of events and signal and background efficiency, tau purity and number of events passing the cuts in the data. The cuts applied are efficient in rejecting background, while retaining high signal efficiency. After the cuts, the expected tau concentration increases to 13.6%.

Table 8.1: Number of background, tau signal and data passing the event selection in each Super-K period.

	Tau	Tau efficiency	BG	BG efficiency	Tau purity	Data
Multi-GeV, FCFV	193.5	-	10320.0	-	1.8%	9884
and CosTheta<-0.2	167.2	86.4%	3305.9	32.0%	4.8%	3262
and NN>0.54	118.5	61.2%	752.1	7.3%	13.6%	937

In order to obtain the information about change in expected events due to the systematic errors, the cuts are applied on the two-dimensional event distributions for the systematic errors built in Sec 6.3. The change in N_{BG}^{exp} and N_{τ}^{exp} after shifting one systematic error can be determined by counting the number of events in the distributions after the cuts, which are summarized in Table 8.2 and 8.3.

Since the fitted results of the systematic errors are mostly different from the central value in Table 7.7 and 7.8, the expected number of signal and background are calculated with the changes taken into account as follows

$$N_{\tau}^{exp} = N_{\tau}^{0} + \sum_{i} \Delta N_{\tau}^{i} \times \sigma_{i}^{fit}, \tag{8.5a}$$

$$N_{BG}^{exp} = N_{BG}^{0} + \sum_{i} \Delta N_{BG}^{i} \times \sigma_{i}^{fit}, \tag{8.5b}$$

Table 8.2: Change in N_τ^{exp} and N_{BG}^{exp} after shifting one systematic error by 1σ for common systematic errors in all Super-K run periods after selection cuts.

Systematic error	ΔN_τ^{exp}	ΔN_{BG}^{exp}
CCQE $\nu/\bar{\nu}$ ratio	0.13 (0.0)	0.12 (0.0)
CCQE cross section ratio	1.8 (1.2)	0 (0.0)
DIS model difference	105.0 (27.7)	1.9 (0.1)
DIS cross section	32.6 (15.5)	3.8 (2.4)
K/π ratio	6.4 (3.7)	1.5 (0.9)
NC/CC ratio	47.3 (20.3)	0.0 (0.0)
Flux normalization ($E_\nu > 1$GeV)	57.4 (29.2)	8.7 (5.1)
coherent π cross section	2.6 (1.4)	0.02 (0.0)
DIS q^2 dependence for low W	35.6 (22.9)	9.7 (7.0)
DIS q^2 dependence for high W	7.7 (2.8)	0.7 (0.1)
1π CAaa5 error	6.6 (3.2)	1.3 (0.5)
1π axial coupling	12.7 (5.5)	3.1 (1.1)
1π background scale factor	4.3 (1.9)	0.4 (0.10
horizontal/vertical ratio	2.2 (0.8)	0.9 (0.6)
Δm^2_{23} error	2.2 (2.9)	1.7 (2.0)
matter effect	0.5 (0.1)	0.1 (0.0)
meson exchange on/off	3.3 (2.5)	0.0 (0.0)
$\nu/\bar{\nu}$ ratio ($E_\nu > 10GeV$)	2.6 (1.3)	2.4 (1.7)
$\bar{\nu}_e/\nu_e$ ratio ($E_\nu > 10GeV$)	2.7 (2.5)	0 (0)
neutrino path length	0.12 (0.0)	0.1 (0.0)
single-pion $\bar{\nu}/\nu$ ratio	1.9 (0.5)	0.2 (0.0)
$\bar{\nu}_\mu/\nu_\mu$ ratio ($E_\nu > 10$ GeV)	3.5 (2.9)	1.4 (1.0)
single pion $\pi^0/\pi^\pm$ ratio	4.1 (2.7)	1.3 (0.5)
sample by sample normalization FC multi-GeV	37.5 (17.8)	5.3 (3.0)
$\sin^2(\theta_{23})$	13.0 (5.6)	0.1 (0.0)
single meson cross section	3.7 (0.8)	0.6 (0.3)
$\sin^2(2\theta_{13})$	1.7 (1.2)	0.03 (0.1)

Table 8.3: Change in N_τ^{exp} and N_{BG}^{exp} after shifting one systematic error by 1σ for systematic errors that are independent between Super-K run periods.

Systematic error	SK-I		SK-II		SK-III		SK-IV	
	ΔN_τ^{exp}	ΔN_{BG}^{exp}	ΔN_τ^{exp}	ΔN_{BG}^{exp}	ΔN_τ^{exp}	ΔN_{BG}^{exp}	ΔN_τ^{exp}	ΔN_{BG}^{exp}
1-ring e-like BG	0.4 (0.3)	0.0 (0.0)	0.5 (0.3)	0.0 (0.0)	0.3 (0.3)	0.0 (0.0)	0.8 (0.7)	0.0 (0.0)
multi-ring e-like BG	9.3 (3.8)	0.0 (0.0)	4.8 (3.5)	0.0 (0.0)	3.1 (1.3)	0.0 (0.0)	15.8 (6.6)	0.0 (0.0)
ring separation	3.1 (0.6)	0.5 (0.3)	1.1 (0.5)	0.1 (0.1)	0.4 (0.1)	0.1 (0.0)	1.2 (0.4)	0.3 (0.2)
multi-ring PID	9.3 (3.9)	1.5 (0.8)	7.5 (3.5)	1.0 (0.5)	2.4 (1.0)	0.4 (0.2)	8.6 (3.7)	1.4 (0.8)

where N_τ^{exp} (N_{BG}^{exp}) is the expected signal (background), N_τ^0 is the signal (background) before adding the effect of systematic errors, as shown in Table 8.1, ΔN_τ^i (ΔN_{BG}^i) is the change of signal (background) after shifting the i'th systematic error by 1σ and σ_i^{fit} is the fitted value of the i'th systematic error shown in Table 7.7 and 7.8. The expected signal is shown in Fig. 8.4, along with data after subtracting expected background from it. The number of expected tau events is 126.0 (81.3), while the number of background events is 748.0 after the cuts in Table 8.1 and adding the effect of systematic errors.

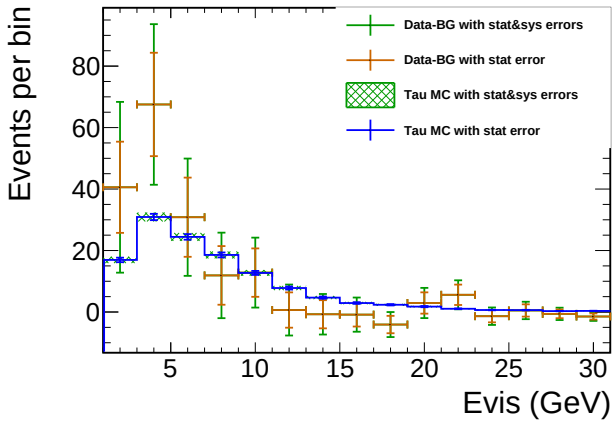

FIGURE 8.4: Visible energy of events passing the cuts in Table 8.1. Expected background is subtracted from data, shown in dots, with statistical uncertainties from data (orange) and systematic uncertainties from background simulations. Expected tau events are shown in the blue histogram, with statistical (blue) and systematic (shaded green) uncertainties.

A set of toy MC experiments is produced to estimate the statistical and systematic uncertainties of the measured S_τ. We assigned statistical and systematic uncertainties to signal and background events separately from Table 8.2 and 8.3. The fitted sizes of the systematic errors from Table 7.7 and 7.8 are introduced to constrain the systematic errors in the toy MC experiments.

$$\epsilon_i = Gaus(0, \sigma_i^{fit}), \tag{8.6a}$$

$$N'_\tau = N^{exp}_\tau + \sum_i \epsilon_i \times \Delta N^i_\tau, \quad N'_{BG} = N^{exp}_{BG} + \sum_i \epsilon_i \times \Delta N^i_{BG}, \tag{8.6b}$$

$$S_\tau = \frac{Gaus(N^{obs}, \sqrt{Gaus(N^{obs})} - N'_{BG}}{N'_\tau}, \tag{8.6c}$$

where ϵ_i is the value of systematic error randomly generated with a Gaussian function centered at 0 with a width of the fitted error size of that systematic error, and N'_τ (N'_{BG}) is the number of expected signal (background) including the changes caused by systematic errors. The number of events in the observation is randomized with a Gaussian function. By forcing σ_i to be 0, we can estimate the statistical uncertainty of S_τ. The distribution of S_τ in the toy MC experiments is shown in Fig. 8.5.

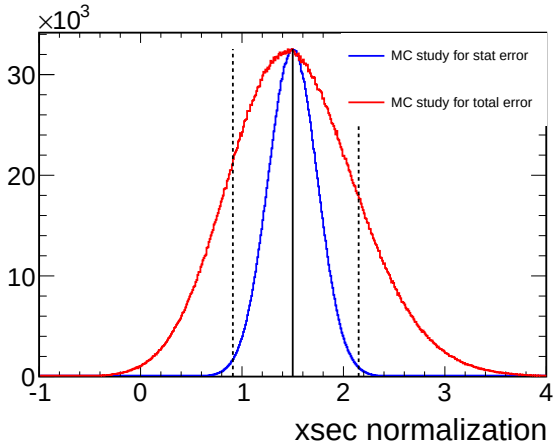

FIGURE 8.5: S_τ distribution in toy MC experiments generated with expected signal, background and data after selections. The solid black line shows the central value of S_τ as 1.5. The dashed line denotes the boundaries of 68% C.L. region, which is 0.91-2.15.

By multiplying S_τ with the flux-averaged theoretical charged current tau neutrino cross section, we obtain the measured cross section as $0.96^{+0.42}_{-0.38} \times 10^{-38}\text{cm}^2$, to be compared with the previous result of $0.94 \pm 0.20 \times 10^{-38}\text{cm}^2$. The different uncertainties of two methods are basically due to the difference between the one-dimensional fit and two-dimensional fit.

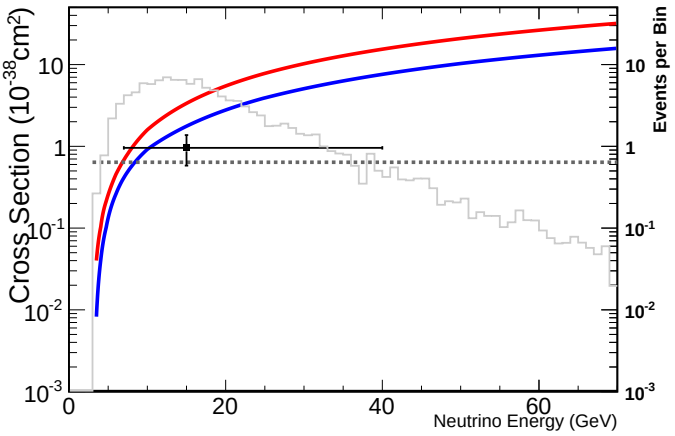

FIGURE 8.6: Flux-averaged tau neutrino cross section between 3 GeV and 70 GeV.

We expect that multidimensional fits have better sensitivity because more data and information are used. The tau normalization is fitted with a single dimensional fit, with only the zenith angle information used in the fit. The distribution of fitted tau normalization in a set of toy MC is shown in Fig. 8.7, which has a width of 0.46 in a Gaussian fit. It is noted that the width is much larger than 0.24 in the two-dimensional fit.

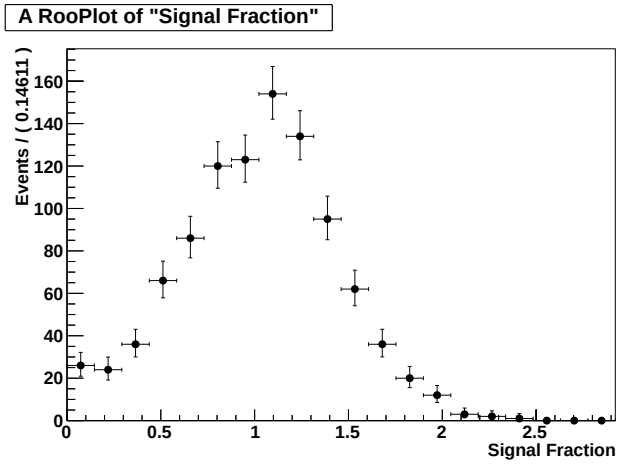

FIGURE 8.7: Tau normalization in toy MC generated and fitted with one-dimensional PDFs.

Due to the better sensitivity of the full two-dimensional fit, we report $0.94 \pm 0.20 \times 10^{-38}$cm^2

as the final result of the cross section study.

8.2 Comparisons with Previously Reported Results

8.2.1 Flux-averaged Tau Neutrino Cross Section

Because of the difficulties in tau neutrino production and detection, charged-current tau neutrino cross sections have not been well measured. DONUT is the only experiment that previously measured the charged-current DIS tau neutrino cross section. They used 9 observed charged-current tau neutrino events with an estimated background of 1.5 events. 800 GeV protons from Fermilab Tevatron were used to produce neutrino beam by colliding with a beam dump, and tau neutrinos were produced via decays of charmed mesons. The mean energies of the detected tau neutrino interactions were calculated to be 111 GeV (Kodama et al., 2001), in which deep inelastic interactions are dominant. Assuming that the DIS charged-current tau neutrino cross section has a linear dependence on neutrino energy, DONUT measured the slope of the energy dependence of the cross section including the kinematic effect of tau lepton mass from the standard model calculation.

$$\sigma(E) = \sigma_{const} \cdot E \cdot K(E) \tag{8.7}$$

where $\sigma(E)$ is the charged-current deep inelastic cross section as a function of neutrino energy, σ_{const} is the slope that is to be measured, and $K(E)$ is the kinematic effect of the tau lepton mass from standard model calculation (shown in Fig. 8.8). σ_{const} is measured to be $(0.39 \pm 0.13 \pm 0.13) \times 10^{-38}\text{cm}^2\text{GeV}^{-1}$ (Kodama et al., 2001) in the final DONUT result. DONUT are incapable of distinguishing the charge of the τ lepton. Therefore, the measurement result is an average of ν_τ and $\bar{\nu}_\tau$ cross sections assuming equal number of ν_τ and $\bar{\nu}_\tau$ in the neutrino flux (Kodama et al., 2001). The ν_τ flux is larger than the $\bar{\nu}_\tau$ flux, which are used to reweight the DONUT cross sections.

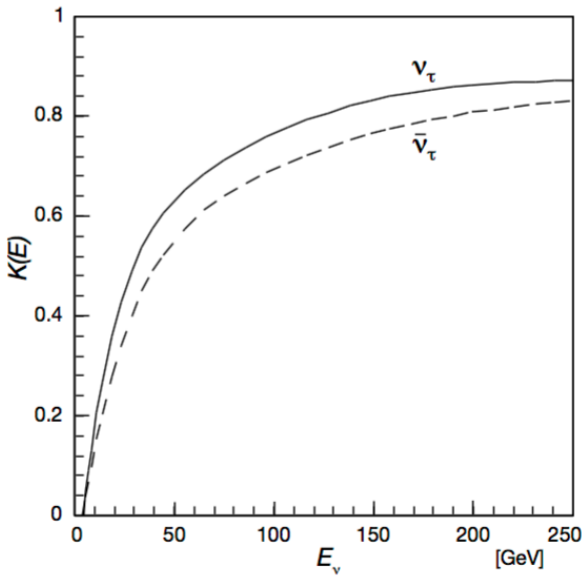

FIGURE 8.8: Suppression of tau neutrino cross section relative to electron and muon neutrinos due to the tau lepton mass. Taken from (Kodama et al., 2001).

In order to compare the Super-K measurement with the DONUT measurement, the DONUT cross section result is reweighted by the Super-K tau neutrino flux. $\sigma(E)$ is calculated for neutrino energy between 3.5 GeV and 70 GeV from σ_{const}, $K(E)$ and the ratio of cross sections between ν_μ and $\bar{\nu}_\mu$ in (Patrignani et al., 2016). $\sigma(E)$ and $\langle\sigma\rangle$ are shown in Fig. 8.9. The flux-weighted charged-current tau neutrino DIS cross section is $(0.37 \pm 0.18) \times 10^{-38}\text{cm}^2$, to be compared with $(0.94 \pm 0.20) \times 10^{-38}\text{cm}^2$ in the Super-K measurement. Our result is larger than the reweighted DONUT cross section because of the difference in neutrino energies. DONUT measured the DIS cross section with a neutrino beam that has a much higher average energy than that of tau neutrinos at Super-K. CCQE and CC coherent production is negligible in the DONUT measurement. However, tau neutrinos at Super-K have a large component of neutrinos below 10 GeV, where CCQE and CC coherent production cross sections make a significant contribution to the final result.

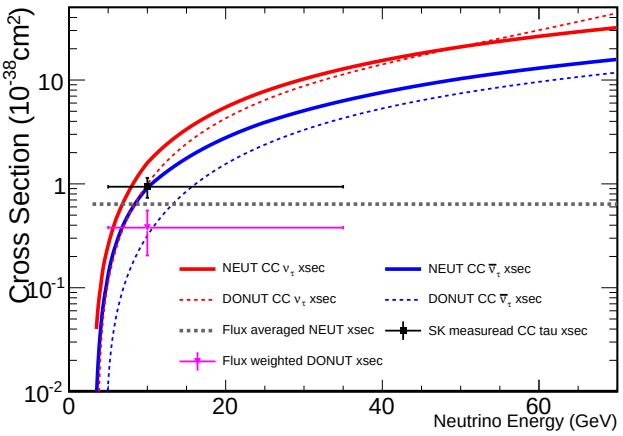

FIGURE 8.9: Comparison of the Super-K measured flux-averaged CC tau neutrino cross section with DONUT result reweighted by the Super-K tau neutrino flux. DONUT cross section digitized from (Kodama et al., 2008), and weighted by the tau neutrino from at Super-Kamiokande, $< \sigma >= (0.37 \pm 0.18) \times 10^{-38}\text{cm}^2$.

8.2.2 Comparison of σ/E with DONUT Result

Instead of measuring a flux-average cross section, we can also measure σ/E, as for the DONUT result. The theoretical value of σ/E for ν_τ and $\bar{\nu}_\tau$ can be calculated with the NEUT model, which is a function of energy. Using the same method of scaling MC to match data, we can calculate the value of σ/E at energies between 3.5 GeV and 70 GeV in our measurement. Because ν_τ and $\bar{\nu}_\tau$ have different cross sections ($\sigma_{\nu_\tau}/E = 0.455\times10^{-38}\text{cm}^2\text{GeV}^{-1}$, $\sigma_{\nu_{\bar{\tau}}}/E$=$0.226\times10^{-38}\text{cm}^2\text{GeV}^{-1}$) and fluxes in our measurement, the measured σ/E has to be weighted by their fluxes. The measured σ/E at 70 GeV is $0.51\pm0.11\times10^{-38}\text{cm}^2\text{GeV}^{-1}$.

In order to compare our result with DONUT result, the DONUT cross section as a function of energy is calculated based on Equation 8.7. The kinematic function used in the DONUT cross section is digitized, and the value at 70 GeV is taken to calculate σ/E (E=70 GeV) to be $0.364\times10^{-38}\text{cm}^2\text{GeV}^{-1}$ for ν_τ and $0.164\times10^{-38}\text{cm}^2\text{GeV}^{-1}$ for $\bar{\nu}_\tau$. The σ/E weighted by Super-K tau neutrino fluxes is $0.27\pm0.13\times10^{-38}\text{cm}^2\text{GeV}^{-1}$. Our σ/E result is more consistent with the DONUT result than the flux-averaged

cross section because CC DIS is dominant at 70 GeV.

9

Three-flavor Oscillation Analysis with Tau Identification

In spite of the dominant effect of $\nu_\mu \rightarrow \nu_\tau$ oscillation in atmospheric neutrinos, sub-dominant effects are expected in atmospheric neutrino oscillations. The non-zero θ_{13} from reactor neutrino experiment measurements implies that ν_μ oscillates into ν_e. The oscillation has a considerable effect on atmospheric neutrino oscillations when matter effects are involved. A full three-flavor oscillation analysis could extract information about the neutrino mass hierarchy from Super-K atmospheric neutrino data by measuring the resonance of electron neutrinos in the multi-GeV region. Unfortunately, the tau neutrino appearance shows up in the same upward-going multi-GeV sample, which looks similar to electron neutrino in Super-K reconstruction. The CC tau events are an important background that is not well constrained due to the large uncertainty on its cross section. The tau identification tools developed for the tau neutrino appearance search have the capability to separate tau events from other events statistically, thus reducing this background. The tool has been incorporated into the full three-flavor neutrino oscillation analysis, and is capable of improving the sensitivity to the neutrino mass hierarchy by constraining the tau background.

9.1 Three-flavor Atmospheric Neutrino Oscillation

9.1.1 Electron Neutrino Resonance Induced by Matter Effect

ν_e oscillation is a sub-dominant effect in atmospheric neutrino oscillations. It includes ν_e disappearance and ν_e appearance from ν_μ. The oscillation probabilities in vacuum can be expressed as:

$$\begin{aligned} P(\nu_e \to \nu_e) =& 1 - \sin^2(2\theta_{13}) \sin^2(\frac{1.27\Delta m^2_{23} L}{E}) \\ P(\nu_\mu \leftrightarrow \nu_e) =& \sin^2(\theta_{23}) \sin^2(2\theta_{13}) \sin^2(\frac{1.27\Delta m^2_{23} L}{E}) \end{aligned} \tag{9.1}$$

As discussed in Section 1.4.4, the matter effect plays an important role in ν_e oscillations. Given a non-zero θ_{13}, the matter effect results in a resonance in the ν_e ($\bar{\nu}_e$) appearance in the normal hierarchy (inverted hierarchy). Fig. 9.1 illustrates the probabilities of $\nu_\mu \to \nu_e$ and $\bar{\nu}_\mu \to \bar{\nu}_e$ under the assumptions of the normal hierarchy or inverted hierarchy. If the mass hierarchy turns out to be normal, there is expected to be a resonance of ν_e appearance in the upward-going multi-GeV region neutrinos but not in antineutrinos, and vice versa. Therefore, a definite measurement of the difference between electron neutrinos and antineutrinos in this region could determine the mass hierarchy.

9.1.2 Oscillation Analysis Framework

In order to measure the oscillation parameters including the mass hierarchy, Super-K performs a full three-flavor oscillation analysis (Wendell et al., 2010; Abe et al., 2011b). The analysis framework is designed to compare the data against the MC for different oscillation models. A particular oscillation model specifies a value for each oscillation parameter, and the MC is oscillated based on that model. A model's compatibility with the data is defined as a goodness of fit statistic between the two. A set of oscillation models forms a grid in the parameter space, and the analysis

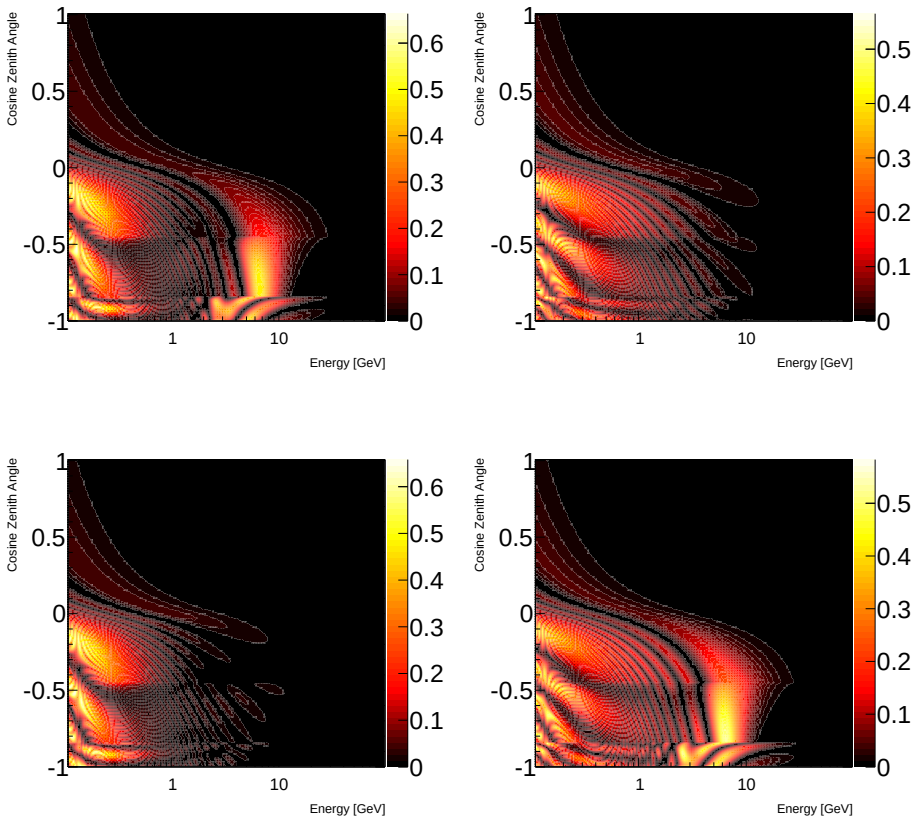

FIGURE 9.1: Probabilities of $\nu_\mu \rightarrow \nu_e$ (left) and $\bar{\nu}_\mu \rightarrow \nu_e$ under the assumption of the normal hierarchy (top) and inverted hierarchy (bottom). It is noted that resonance in the upward multi-GeV region shows up in different neutrino types under the assumptions of the normal or inverted hierarchy. Oscillation probabilities are calculated assuming the oscillation parameters: $\Delta m^2_{12} = 7.6 \times 10^{-5} eV^2$, $\Delta m^2_{32} = 2.4 \times 10^{-3} eV^2$, $\sin^2\theta_{12} = 0.3$, $\sin^2\theta_{23} = 0.5$, $\sin^2\theta_{13} = 0.0238$ and $\delta_{CP} = 0$.

performs a search over the grid for the best agreement with the data.

All data samples including FC, PC and UPMU are used in the analysis. In order to best extract the information from the data, the MC and data are divided into subsamples. The details of the event separation is described in (Lee, 2012). The subsamples are further binned in energy and cosine of reconstructed zenith angle of the event, as shown in Fig. 9.2.

Super-K performs a full three-flavor neutrino oscillation analysis with the atmospheric neutrino sample, in which the sub-leading effects are taken into account. In

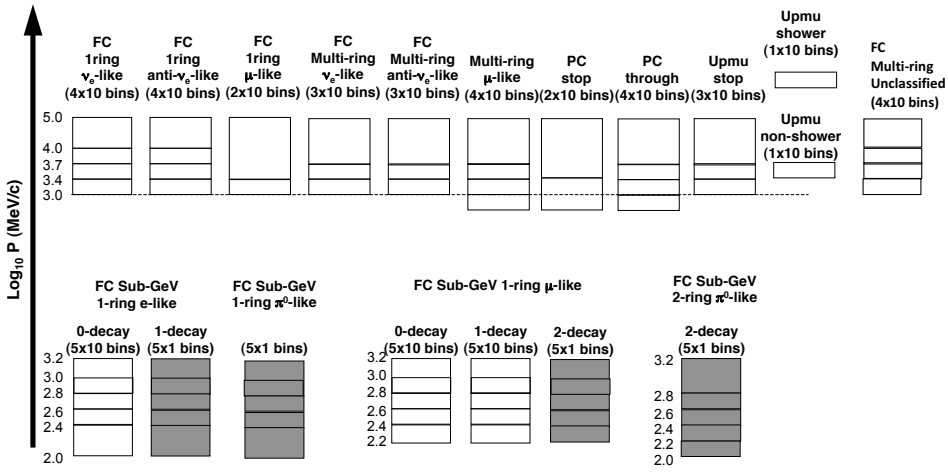

FIGURE 9.2: Definition of the binning scheme in the three-flavor oscillation analysis. 410 bins in FC, 60 bins in PC, 50 bins in UPMU. White boxes indicate that momentum bin is uniformly divided into 10 zenith angle bins between -1 and 1 for FC and PC, between -1 and 0 for UPMU. Shaded boxes indicate that the momentum bin is not further divided into zenith angle bins.

order to examine the compatibility between the data and the oscillation parameters, data are compared the MC expectation using a pull χ^2 method based on Poisson probability distribution. The binned likelihood is defined as

$$L(N^{exp}, N^{obs}) = \prod_{i=1}^{n} \frac{e^{-N_i^{exp}} N_i^{exp N_i^{obs}}}{N_i^{obs}!}, \tag{9.2}$$

where N_i^{obs} (N_i^{exp}) is the number of observed (expected) events in the ith bin. χ^2 is defined as the log likelihood ratio

$$\chi^2 = -2 \ln \frac{L(N^{exp}, N^{obs})}{L(N^{obs}, N^{obs})} = 2 \sum_{i=1}^{n} (N_i^{exp} - N_i^{obs} + N_i^{obs} \ln \frac{N_i^{obs}}{N_i^{exp}}). \tag{9.3}$$

The effect of systematic errors are included into the bin with the pull method (Wendell et al., 2010) by replacing N_i^{exp} with

$$N_i^{exp} \rightarrow N_i^{exp}(1 + \sum_{j}^{m} f_{ij} \epsilon_j), \tag{9.4}$$

where ϵ_j is a variation corresponding to the j^{th} systematic uncertainty, f_{ij} is the fractional change of the event rate in the ith bin due to a change of 1σ in the jth systematic uncertainty, the sum is over all the systematic uncertainties considered in the oscillation analysis (Wendell et al., 2010). For each systematic uncertainty, the quantity ϵ_j/σ_j is assumed to follow Gaussian distribution, where σ_j is the 1σ value of the jth systematic uncertainty. Therefore, an additional term is added to the χ^2 to constrain the size of systematic uncertainties in the fit. The final form of χ^2 is defined as

$$\chi^2 = 2\sum_{i=1}^{n}[(N_i^{exp}(1+\sum_j f_{ij}\epsilon_j) - N_i^{obs}) + N_i^{obs}\ln\frac{N_i^{obs}}{N_i^{exp}(1+\sum_j f_{ij\epsilon_j})}] + \sum_j(\frac{\epsilon_j}{\sigma_j})^2. \quad (9.5)$$

The fit varies the systematic uncertainties to minimize χ^2 for a given MC expectation.

In the analysis, θ_{23}, Δm^2_{23}, and δ_{cp} are fitted simultaneously, while θ_{13} is constrained to the recent reactor neutrino measurements. The best-fit information for this fit is summarized in Table. 1. One-dimensional $\Delta\chi^2$ distributions for the oscillation parameters are shown in Fig. 5. Normal hierarchy (NH) is preferred, $\chi^2_{NH} - \chi^2_{IH} = -4.3$, by Super-K atmospheric neutrino data. Toy Monte Carlo samples were generated with the assumption of either normal or inverted hierarchy to test the significance of the preference. The probability of having $\Delta\chi^2$ smaller than -4.3 is 0.45 in the NH assumption, and is between 0.007 ($\sin^2(\theta_{23})$=0.4) and 0.031 ($\sin^2(\theta_{23})$=0.6) in the IH assumption. The best fit information of this fit is also summarized in Table. 1.

Table 9.1: Summary of best-fit information for fits assuming the normal or inverted hierarchy with the Super-K neutrino data only (517 d.o.f.).

Fit	Δ^2_{min}	δ_{CP}	$\sin^2\theta_{23}$	$\Delta m^2_{23,13}[eV^2]$
SK NH	571.7	4.19	0.59	2.5×10^{-3}
SK IH	576.0	4.19	0.58	2.5×10^{-3}

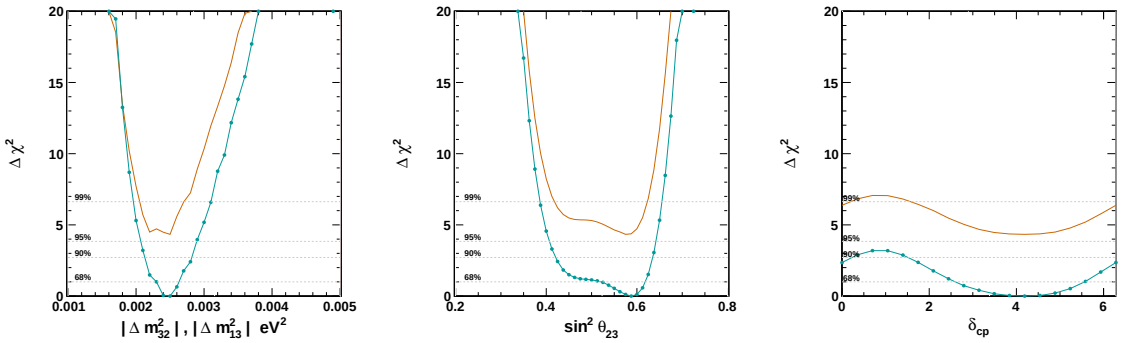

FIGURE 9.3: Constraints on neutrino oscillation parameters from the SKI-IV atmospheric neutrino data. The orange line denotes the result in the IH assumption, which has been offset from the NH result, shown in blue, by the difference of their $\Delta\chi^2$.

9.2 Constraining the Tau Background with Tau Identification

In the standard Super-K reconstruction and analysis, tau events are not separated from other event categories. Due to the dominant hadronic decay channels, the tau events are mostly categorized into e-like samples in the reconstruction and analysis samples. Moreover, the tau appearance shows up in the same region as the electron neutrino appearance induced by θ_{13} and matter effect, which becomes an important background in the three-flavor neutrino oscillation analysis. Fig. 9.4 shows the MC expectations under the assumption of the normal or inverted hierarchy and the tau events in four e-like samples in the three-flavor oscillation analysis. It is noted that the tau appearance shows up in the same region as the electron neutrino appearance resonance, and the two have comparable magnitude. In addition, the charged-current tau neutrino cross sections are known not better than 25%, leading to a large uncertainty in the tau background in the analysis.

We have shown the capability of identifying the tau events with a neural network algorithm in Section 6.3. It is possible to use the tau identification tools in the three-flavor oscillation analysis. In order to use tau identification, the multi-GeV events in the MC simulations and data are processed with the trained neural network, in

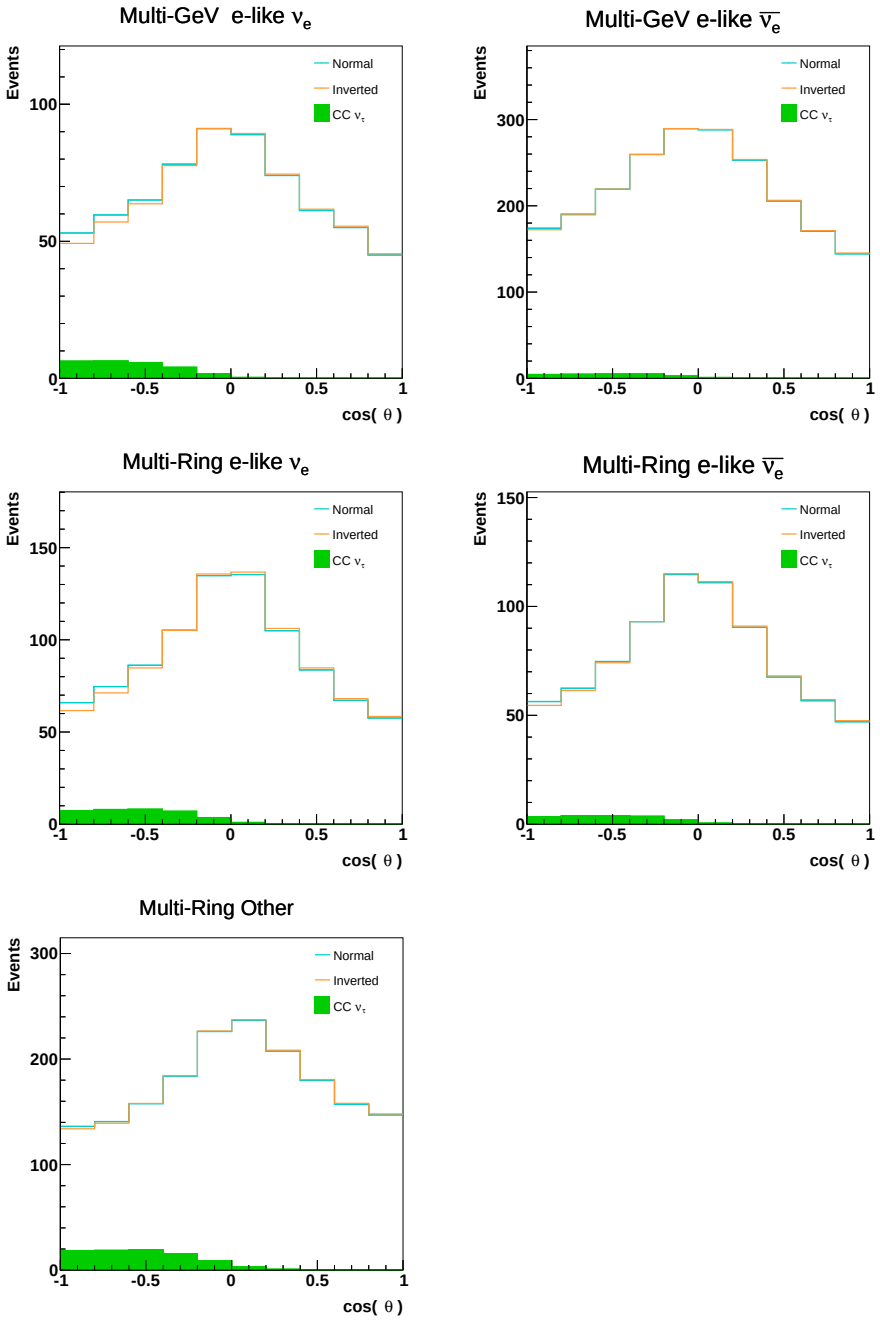

FIGURE 9.4: Zenith angle distribution of five samples that include electron appearance signal in the Super-K three-flavor neutrino oscillation analysis. The MC expected under the assumption of the normal (inverted) hierarchy is shown in blue (orange) histogram, without taking tau events into account. The tau events are shown in the green filled histogram.

which each event is given the neural network output of the tau appearance search.

In the modified three-flavor oscillation analysis, the existing bins for the samples that are expected to have electron neutrino appearance, such as multi-GeV/multi-ring e-like $\nu_e/\bar{\nu}_e$ samples, and the multi-ring unclassified sample, are further divided into two bins based on the tau neutral network output. As shown in Fig. 9.5, one bin in the multi-GeV e-like ν_e sample is divided into two bins at the neural network output value of 0.25. The bin with NN output less than 0.25 has almost no tau events, while the other bin has almost all the tau events.

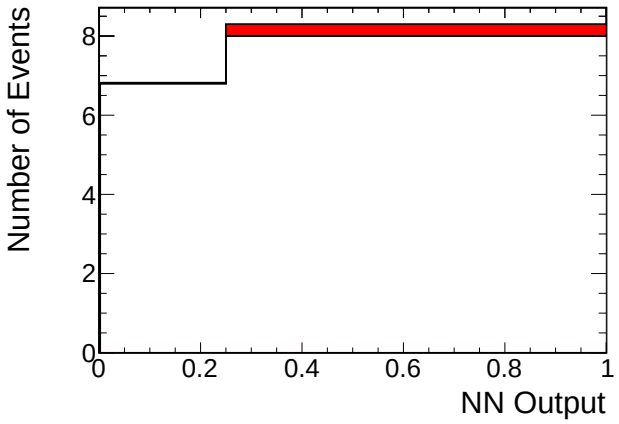

FIGURE 9.5: Distribution of neural network output for events with $3.0 < \log E_{vis} < 3.4$ and $< -1 \cos\theta <$-0.8 in the multi-GeV e-like ν_e sample, corresponding to one bin the standard three-flavor oscillation analysis. The simulations are scaled to the live time of 5326 days in SK-I through SK-IV. The ν_e and ν_μ events are shown in the black histogram, while the tau events are shown in red filled histogram on top of the other events. The single bin is divided into two bins at the neural network equal to 0.25.

A sensitivity study was performed to study the effect of using the tau identification in the oscillation analysis. The study was carried out with SK-I, SK-II, SK-III, and SK-IV MC scaled to the data live time. As in the standard three-flavor oscillation analysis, Δm^2_{32}, $\sin^2\theta_{23}$ and δ_{CP} are free parameters and fitted in the study. Fig. 9.6 shows the $\Delta\chi^2$ as a function of $\sin^2\theta_{23}$ between the normal and inverted hierarchies under the assumption of true normal or inverted hierarchy. The incor-

poration of tau identification in the analysis on average improves the sensitivity to mass hierarchy by $\sim 10\%$.

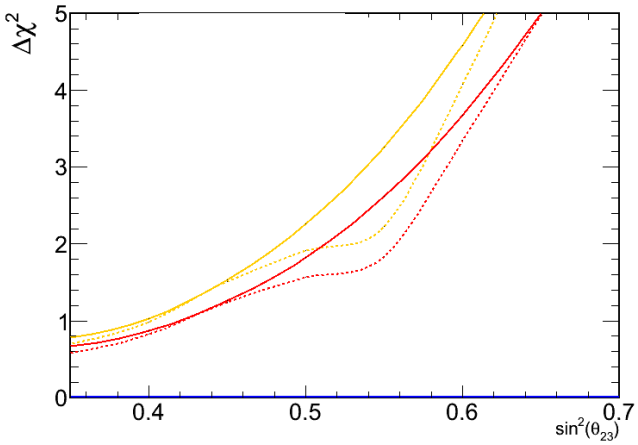

FIGURE 9.6: $\Delta\chi^2$ distribution as a function of $\sin^2\theta_{23}$ for standard binning (red) and with additional binning in neural network output (yellow). Under the assumption of true (inverted) normal hierarchy, the $\Delta\chi^2$ between normal and inverted hierarchies is shown in solid (dashed) lines.

As shown in this section, we have developed a framework to use the tau identification to constrain tau background in the oscillation analysis. The use of tau identification improves the sensitivity to mass hierarchy by $\sim 10\%$. The method is new being incorporated into the Super-K three-flavor oscillation analysis.

10

Conclusion

Super-Kamiokande has collected atmospheric neutrino data for more than 20 years. This dissertation describes the result of a search for atmospheric tau neutrino appearance using 5,326 days of atmospheric neutrino data. Under the assumption of the normal mass hierarchy, Super-K measured the tau normalization at 1.47 ± 0.32 (stat+sys), relative to the expectation of unity for nominal oscillation parameters and assumed charged-current tau neutrino cross section. This result excludes the hypothesis of no tau appearance with a significance of 4.6σ. The result is direct proof of three-flavor neutrino oscillation.

Super-K measured 338.1 ± 72.7 charged-current tau neutrino interactions fully contained in Super-Kamiokande. This charged-current tau neutrino interaction sample is larger than that of the DONUT experiment and the OPERA experiment, which measured 9 and 5 charged-current tau neutrino interactions respectively. Using this large sample, the charged-current tau neutrino cross section is measured by scaling the theoretical cross section in the Super-K simulation to match the measured charged-current tau neutrino interactions. A flux-averaged cross section is measured to be $(0.94 \pm 0.20) \times 10^{-38}$ cm^2 for neutrino energy between 3.5 GeV and 70 GeV,

compared with the flux-averaged theoretical cross section of $0.64 \times 10^{-38}\text{cm}^2$. The measured cross section is consistent with the Standard Model prediction within 1.5 σ, and is only the second reported measurement of this cross section.

An event-by-event tau identification is achieved using tools developed for the search for atmospheric tau neutrino appearance. The tau identification has been implemented in the Super-K three-flavor oscillation analysis. A Monte Carlo study has shown that the sensitivity to the mass hierarchy is improved by $\sim$10% with the tau identification implemented in the analysis.

Appendix A

Ratio of Charge in the Most Energetic Ring

In Ref. (Abe et al., 2013), the fraction of the charge carried by the most energetic ring is defined as

$$rfrac^* = \frac{RTOT_0}{Evis} \tag{A.1}$$

where $RTOT_0$ is the momentum of the most energetic ring in the reconstruction. However, the data and MC do not agree well in this variable in SK-II. The MC on average has a larger value than data, as shown in Fig. A.1. The ratio of the mean value of the variable in data and MC is 0.95. To correct the discrepancy, (Abe et al., 2013) introduced a normalization factor of 0.95 for SK-II MC to reduce the variable of each event.

In this analysis, a newly-defined variable is used to replace the problematic variable. The new definition is shown in Eq. 6.6. Instead of using the event reconstruction result to calculate the ratio, the PMT charges are taken as input to the calculation. The new variable has good agreement between data and MC in all four SK run periods, as shown in Fig. A.2.

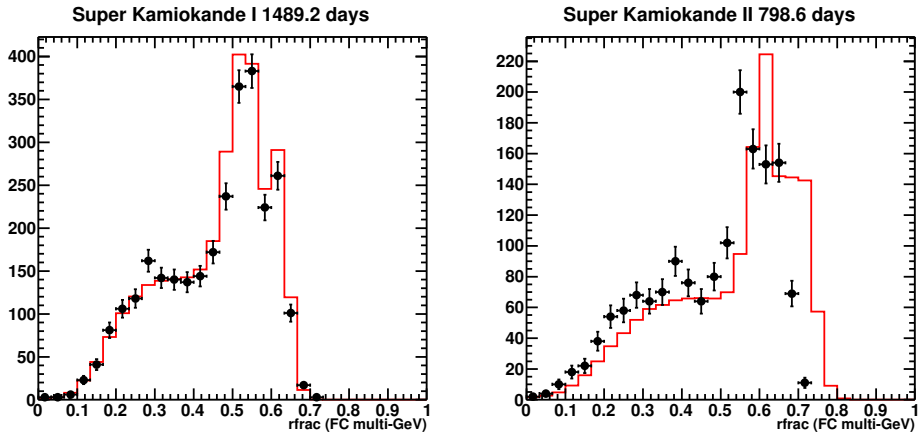

FIGURE A.1: The fraction of energy carried by the most energetic ring for data (dots) and MC (histogram) in SK-I (left) and SK-II (right). SK-III and SK-IV have similar data and MC agreement as in SK-I.

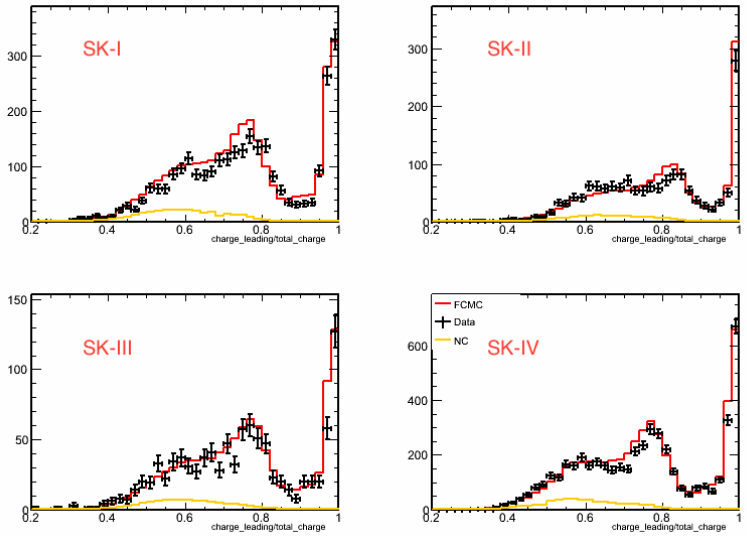

FIGURE A.2: Ratio of charge carried by most energetic ring calculated with PMT charge in each SK period.

Appendix B

Neural Networks and Their Application in Particle Physics

An artificial neural network (ANN) is an information processing method inspired by biological systems. It is composed of a large number of highly inter-connected processing elements (neurons) working together to solve a problem. An ANN is typically organized in layers of inter-connected neurons. The external input is presented to the network via input layer, which communicates to one or more hidden layers where the processing is done via a system of weighted connections. The hidden layer is then linked to an output layer. The ANN is capable of deriving meaning from complicated or imprecise data, which is advantageous over conventional computing. The weights of the connections in the network are adjusted in the learning process according to the external input examples, a process known as training. Neural networks are widely used in particle physics. In this analysis, a multilayer perceptron is chosen to identify tau events. The neural network used is configured with the TMVA package (Hocker et al., 2007). Fig. B.1 demonstrates the structure of a multi-layer perceptron with one hidden layer.

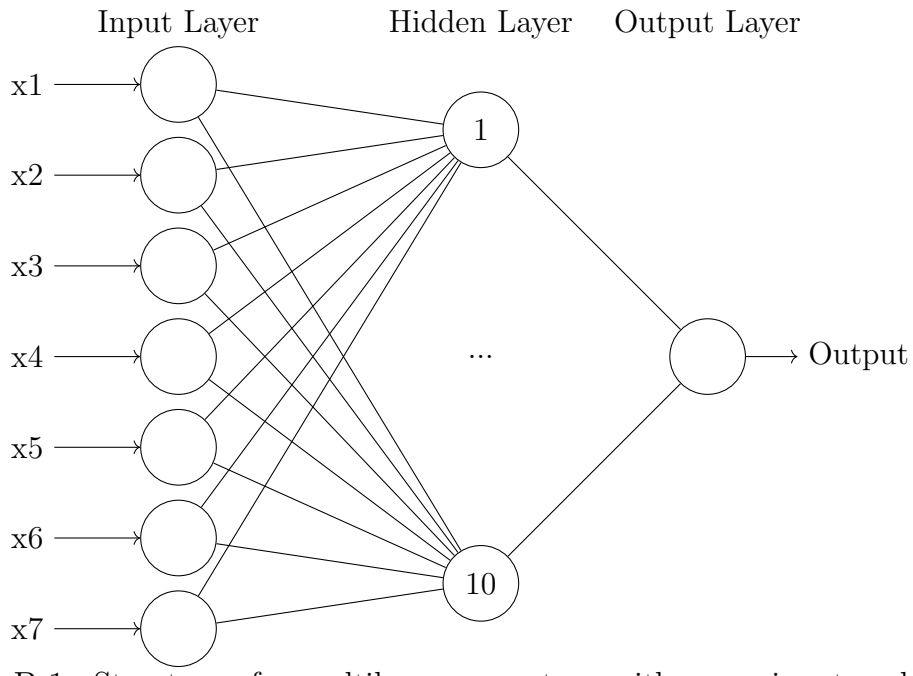

FIGURE B.1: Structure of a multilayer perceptron with seven input nodes in the input layer, one output node in the output layer, and ten nodes in the hidden layer.

Appendix C

Partially Contained Reduction

C.1 Partially Contained Reduction

Partially contained events are different from fully contained events in the OD activities. A dedicated background reduction for the PC events is applied. During the reconstruction of the detector before SK-III, a opaque segmentation was installed in the OD to divide it into three regions - top, side barrel and bottom. The PC reduction is substantially adjusted for SK-III onwards. There are also five stages for PC reduction.

Here PC reduction in SK-III and SK-IV is summarized. Description of PC reduction for SK-I and SK-II could be found in Ref. (Lee, 2012).

C.1.1 PC1

Events that satisfy the following criteria are selected:

1. $\mathrm{PE}_{tot} \geqslant 1000$ p.e.s (500 p.e.s for SK-II). PC events used in the atmospheric neutrino analysis are required to have vertex at least 2 m from the ID wall, corresponding to a minimum momentum of 500 MeV/c. The cut is applied to

conservatively reject events with energy lower than approximately 310 MeV/c.

2. NHITA$_{top}$ < 10 or NHITA$_{bottom}$ < 10, where NHITA$_{top}$ (NHITA$_{bottom}$) is the number of OD hits at the top (bottom) of the OD. The rejects through-going muons from top to bottom.

3. NHITA$_{endcap}$ < 25 or NHITA$_{side}$ < 70, where NHITA$_{side}$ is the number of OD hits on the side barrel of the OD, and "endcap" refers to either top or bottom. This rejects corner clipper muons that produce light in both the endcap and side barrel of the OD.

4. ODR$_{mean}$ < 2100 cm, if OD hits<20 in a 500 nsec time window. where ODR$_{mean}$ is the average distance between all hit pairs that is defined as:

$$ODR_{mean} = \frac{1}{N_{pair}} \sum_{i=1}^{N-1} |\overrightarrow{x_i} - \overrightarrow{x_j}|. \quad \text{(C.1)}$$

Following the first reduction, the event rate is around 2×10^4 events per day.

C.1.2 PC2

PC2 is targeted to remove muon backgrounds based on a cluster algorithm. Events satisfying the following criteria are selected:

1. NHITA$_{endcap}$ < 20 or NHITA$_{endcap}$ < MAX(NHITA$_{side}$), where MAX(NHITA$_{side}$) is defined as $e^{(\alpha-\beta\times NHITA_{side})}$ with α=5.8, β=0.023 if NHITA$_{side}$ < 75, α=4.675, β=0.008 otherwise.

2. Nouter2$\leqslant$10, where Nouter2 is the number of hits in the second highest charge OD cluster.

After PC2, the event rate is reduced to around 8,000 events per day.

C.1.3 PC3

PC3 is is designed to reject flasher events following the same logic as that in the FC3 reduction. Events satisfying the following criteria are removed:

1 NHIT_{100} >14 (9 if the number of ID hits < 800).

C.1.4 PC4

PC4 reduction is based on a muon fitter "muboy" which classifies the remaining cosmic muon background events into stopping muon, through-going muon, multiple muon or corner clipper muon. The six selection criteria based on the muboy information are defined below:

1. Muboy angle < 90°, where Muboy angle is the angle between the muboy fitted direction and the vector between the $pfit$ vertex and the center of the highest charge OD cluster. The cut is targeted to remove stopping muon events.

2. Muboy dotprod>-0.8, where muboy dotprod is similar to muboy angle but instead of using the center of the highest charge OD cluster, the earliest saturated ID PMT is used. This is designed to remove both stopping and through-going cosmic ray muons.

3. Muboy track length<1750 cm, where muboy length is the length of the muon track fitted by muboy.

4. Muboy goodness<0.52. This is the goodness of fit given by muboy. A good fit indicates a cosmic muon.

5. Muboy corner⩾300 cm, where muboy corner is the distance between the muboy entry point and the corners of the tank.

6. Muboy ehit8m$\geqslant$300 cm, where ehit8m is the number of OD hits located within 8 m of the entrance point from muboy fit in a fixed 5 nsec time window.

If an event is classified as a through-going muon by muboy, then it has to pass four of the first five cuts. If an event is classified as a stopping muon by muboy, then it has to pass four out of the first five cuts including the muboy dotprod cut. Additionally, it has to pass either the muboy ehit8m cut or have a muboy goodness $<$0.5. Otherwise, the event only needs to pass two of the first five cuts.

Finally, a cut on the total ID charge is applied to remove low-energy events:

- $\mathrm{PE}_{tot} < 2900$ p.e.

After the PC4 reduction, the event rate is $\sim$300 events/day.

C.1.5 PC5

PC5 consists of a series of cuts dedicated for different types of background sources. The cuts are classified into hard cuts and soft cuts. Hard cuts are cuts that an event is required to pass in order to be kept, including a through-going muon cut, stopping muon cut, cable hole muon cut and corner clipper muon cut. The events are allowed to fail the soft cuts once before being rejected. Soft cuts include through-going muon cut, stopping muon cut, corner clipper muon cut and a decay muon cut. A detailed description of the cuts can be found in Ref. (Lee, 2012).

A corner clipper based on clusters in OD segmented regions is applied on events with visible energy less than 1 GeV, aiming to remove corner clipper muons. Instead of clustering the OD PMTs together, the cluster algorithm is applied on the PMTs on top, bottom and side walls separately. The largest charged cluster on endcap and side wall are selected. In addition, the ID PMTs are clustered and the largest charged cluster is used. The maximum distance between either of the three clusters ($\mathrm{Dist}_{segclust}$) and the smaller charge of the two OD clusters ($\mathrm{NHITA}_{segclust}$) are

calculated. The events satisfying the following criterion are rejected:

- Dist$_{sigclust}$ <1500 and NHITA$_{segclust}$ >30.

Fig. C.1 shows the scatter plot of Dist$_{segclust}$ and NHITA$_{segclust}$ in MC and data.

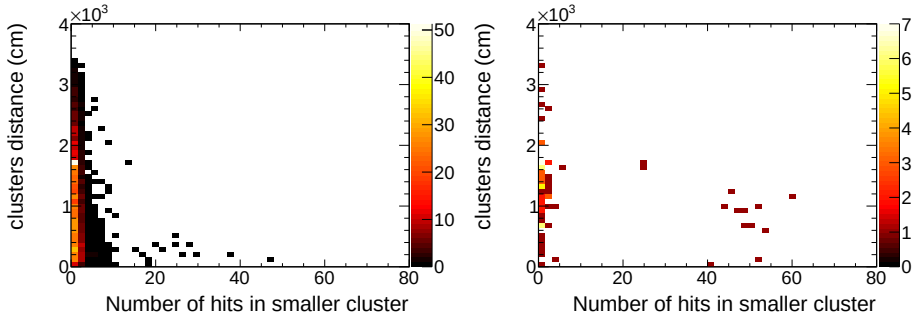

FIGURE C.1: Scatter plot of Dist$_{segclust}$ and NHITA$_{segclust}$ in MC (left) and data (right) before the last corner clipper cut in PC5. The data events with NHITA$_{segclust}$ >30 and E$_{vis}$ < 1500 MeV are mostly background events tagged in the eye-scan.

Following the PC5 reduction, the event rate is ∼1.2 events/day.

C.1.6 PC Reduction Summary

The final dataset of PC events are selected by the following cuts:

1. Reconstructed vertex is located inside the fiducial volume (at least 2 m from the ID wall),
2. NHITAC⩾16 (10 for SK-I),

3.0 Visible energy > 350 MeV.

The final sample is also eye-scanned to tag the background events (but *not* to remove them from the final sample). Table C.1 shows the estimated background contamination in different run periods.

Table C.1: Estimated contamination by cosmic ray muons for PC.

	SK-I	SK-II	SK-III	SK-IV
cosmic ray BG	0.2%	0.7%	1.8%	0.6%

Bibliography

Aad, G. et al. (2012), "Observation of a new particle in the search for the Standard Model Higgs boson with the ATLAS detector at the LHC," *Phys. Lett.*, B716, 1–29.

Aartsen, M. G. et al. (2016), "Neutrino oscillation studies with IceCube-DeepCore," *Nucl. Phys.*, B908, 161–177.

Abdurashitov, J. N. et al. (1999), "Measurement of the solar neutrino capture rate with gallium metal," *Phys. Rev.*, C60, 055801.

Abe, K. et al. (2006), "A Measurement of atmospheric neutrino flux consistent with tau neutrino appearance," *Phys. Rev. Lett.*, 97, 171801.

Abe, K. et al. (2011a), "Indication of Electron Neutrino Appearance from an Accelerator-produced Off-axis Muon Neutrino Beam," *Phys. Rev. Lett.*, 107, 041801.

Abe, K. et al. (2011b), "Search for Differences in Oscillation Parameters for Atmospheric Neutrinos and Antineutrinos at Super-Kamiokande," *Phys. Rev. Lett.*, 107, 241801.

Abe, K. et al. (2012a), "First Muon-Neutrino Disappearance Study with an Off-Axis Beam," *Phys. Rev.*, D85, 031103.

Abe, K. et al. (2013), "Evidence for the Appearance of Atmospheric Tau Neutrinos in Super-Kamiokande," *Phys. Rev. Lett.*, 110, 181802.

Abe, K. et al. (2014), "Calibration of the Super-Kamiokande Detector," *Nucl. Instrum. Meth.*, A737, 253–272.

Abe, K. et al. (2017), "First combined analysis of neutrino and antineutrino oscillations at T2K," .

Abe, Y. et al. (2012b), "Indication for the disappearance of reactor electron antineutrinos in the Double Chooz experiment," *Phys. Rev. Lett.*, 108, 131801.

Achard, P. et al. (2004), "Measurement of the atmospheric muon spectrum from 20-GeV to 3000-GeV," *Phys. Lett.*, B598, 15–32.

Adamson, P. et al. (2011), "Improved search for muon-neutrino to electron-neutrino oscillations in MINOS," *Phys. Rev. Lett.*, 107, 181802.

Adamson, P. et al. (2016), "First measurement of muon-neutrino disappearance in NOvA," *Phys. Rev.*, D93, 051104.

Agafonova, N. et al. (2015), "Discovery of τ Neutrino Appearance in the CNGS Neutrino Beam with the OPERA Experiment," *Phys. Rev. Lett.*, 115, 121802.

Aguilar-Arevalo, A., Bazarko, A., Brice, S., Brown, B., Bugel, L., Cao, J., Coney, L., Conrad, J., Cox, D., Curioni, A., et al. (2008), "Measurement of muon neutrino quasielastic scattering on carbon," *Physical review letters*, 100, 032301.

Aguilar-Arevalo, A. A. et al. (2013), "First measurement of the muon antineutrino double-differential charged-current quasielastic cross section," *Phys. Rev.*, D88, 032001.

Ahmad, Q. R. et al. (2002), "Direct evidence for neutrino flavor transformation from neutral current interactions in the Sudbury Neutrino Observatory," *Phys. Rev. Lett.*, 89, 011301.

Ahn, J. K. et al. (2012), "Observation of Reactor Electron Antineutrino Disappearance in the RENO Experiment," *Phys. Rev. Lett.*, 108, 191802.

Ahn, M. H. et al. (2003), "Indications of neutrino oscillation in a 250 km long baseline experiment," *Phys. Rev. Lett.*, 90, 041801.

Ahrens, L. A. et al. (1986), "Precise Determination of $Sin^2\theta_w$ From Measurements of the Differential Cross-sections for $\nu_\mu p \to \nu_\mu p$ and $\bar{\nu}_\mu p \to \bar{\nu}_\mu p$," *Phys. Rev. Lett.*, 56, 1107, [Erratum: Phys. Rev. Lett.56,1883(1986)].

Alcaraz, J. et al. (2000), "Cosmic protons," *Phys. Lett.*, B490, 27–35.

Allison, W. W. M. et al. (1999), "The Atmospheric neutrino flavor ratio from a 3.9 fiducial kiloton year exposure of Soudan-2," *Phys. Lett.*, B449, 137–144.

Ambrosini, G. et al. (1998), "K / pi production ratios from 450-GeV/c protons on beryllium," *Phys. Lett.*, B420, 225.

An, F. P. et al. (2012), "Observation of electron-antineutrino disappearance at Daya Bay," *Phys. Rev. Lett.*, 108, 171803.

Araki, T. et al. (2005), "Measurement of neutrino oscillation with KamLAND: Evidence of spectral distortion," *Phys. Rev. Lett.*, 94, 081801.

Arnison, G. et al. (1983), "Experimental Observation of Isolated Large Transverse Energy Electrons with Associated Missing Energy at $\sqrt{s} = 540$-GeV," *Phys. Lett.*, 122B, 103–116, [,611(1983)].

Bahcall, J. N., Calaprice, F., McDonald, A. B., and Totsuka, Y. (1996), "Solar neutrino experiments: The next generation," *Physics Today*, 49, 30–36.

Banner, M. et al. (1983), "Observation of Single Isolated Electrons of High Transverse Momentum in Events with Missing Transverse Energy at the CERN anti-p p Collider," *Phys. Lett.*, 122B, 476–485.

Barger, V. D., Whisnant, K., Pakvasa, S., and Phillips, R. J. N. (1980), "Matter Effects on Three-Neutrino Oscillations," *Phys. Rev.*, D22, 2718.

Barish, S. J. et al. (1977), "Study of Neutrino Interactions in Hydrogen and Deuterium. 1. Description of the Experiment and Study of the Reaction Neutrino μ+d$\rightarrow$ μ^-+p+p_s," *Phys. Rev.*, D16, 3103.

Barlag, S. et al. (1982), "Charged Hadron Multiplicities in High-energy Anti-muon Neutrino n and Anti-muon Neutrino p Interactions," *Z. Phys.*, C11, 283, [Erratum: Z. Phys.C14,281(1982)].

Battistoni, G., Ferrari, A., Montaruli, T., and Sala, P. R. (2003), "The FLUKA atmospheric neutrino flux calculation," *Astropart. Phys.*, 19, 269–290, [Erratum: Astropart. Phys.19,291(2003)].

Becker-Szendy, R. et al. (1992), "The Electron-neutrino and muon-neutrino content of the atmospheric flux," *Phys. Rev.*, D46, 3720–3724.

Becker-Szendy, R. et al. (1993), "IMB-3: A Large water Cherenkov detector for nucleon decay and neutrino interactions," *Nucl. Instrum. Meth.*, A324, 363–382.

Belikov, S. V. et al. (1985), "Quasielastic Neutrino and Anti-neutrinos Scattering: Total Cross-sections, Axial Vector Form-factor," *Z. Phys.*, A320, 625.

Benvenuti, A. et al. (1974), "Observation of Muonless Neutrino Induced Inelastic Interactions," *Phys. Rev. Lett.*, 32, 800–803.

Berger, C. and Sehgal, L. M. (2007), "Lepton mass effects in single pion production by neutrinos," *Phys. Rev.*, D76, 113004.

Beringer, J. et al. (2012), "Review of Particle Physics (RPP)," *Phys. Rev.*, D86, 010001.

Bienlein, J. K. et al. (1964), "Spark chamber study of high-energy neutrino interactions," *Phys. Lett.*, 13, 80–86.

Bodek, A. and Yang, U. K. (2002), "Modeling deep inelastic cross-sections in the few GeV region," *Nucl. Phys. Proc. Suppl.*, 112, 70–76, [,70(2002)].

Bonetti, S., Carnesecchi, G., Cavalli, D., Negri, P., Pullia, A., Rollier, M., Romano, F., and Schira, R. (1977), "Study of Quasielastic Reactions of Neutrino and anti-neutrino in Gargamelle," *Nuovo Cim.*, A38, 260–270.

Brun, R., Bruyant, F., Maire, M., McPherson, A. C., and Zanarini, P. (1987), "GEANT3," .

Brunner, J. et al. (1990), "Quasielastic Nucleon and Hyperon Production by Neutrinos and Anti-neutrinos With Energies Below 30-GeV," *Z. Phys.*, C45, 551.

Capella, A., Kaidalov, A., Merino, C., and Tran Thanh Van, J. (1994), "Structure functions and low x physics," *Phys. Lett.*, B337, 358–366.

Chatrchyan, S. et al. (2012), "Observation of a new boson at a mass of 125 GeV with the CMS experiment at the LHC," *Phys. Lett.*, B716, 30–61.

Cowan, C. L., Reines, F., Harrison, F. B., Kruse, H. W., and McGuire, A. D. (1956), "Detection of the Free Neutrino: a Confirmation," *Science*, 124, 103–104.

Danby, G., Gaillard, J.-M., Goulianos, K., Lederman, L. M., Mistry, N., Schwartz, M., and Steinberger, J. (1962), "Observation of High-Energy Neutrino Reactions and the Existence of Two Kinds of Neutrinos," *Phys. Rev. Lett.*, 9, 36–44.

Davidson, N., Nanava, G., Przedzinski, T., Richter-Was, E., and Was, Z. (2012), "Universal Interface of TAUOLA Technical and Physics Documentation," *Comput. Phys. Commun.*, 183, 821–843.

Davis, R. (1994), "A review of the Homestake solar neutrino experiment," *Prog. Part. Nucl. Phys.*, 32, 13–32.

Davis, Jr., R. (1955), "Attempt to detect the antineutrinos from a nuclear reactor by the Cl37(anti-nu,e-) A37 reaction," *Phys. Rev.*, 97, 766–769.

de Perio, P. (2011), "NEUT pion FSI," *AIP Conf. Proc.*, 1405, 223–228.

Derrick, M. et al. (1978), "Properties of the Hadronic System Resulting from anti-Muon-neutrino p Interactions," *Phys. Rev.*, D17, 1.

Dimopoulos, S. and Susskind, L. (1978), "On the Baryon Number of the Universe," *Phys. Rev.*, D18, 4500–4509.

Dziewonski, A. M. and Anderson, D. L. (1981), "Preliminary reference Earth model," *Physics of the earth and planetary interiors*, 25, 297–356.

Fermi, E. (1934), "Trends to a Theory of beta Radiation. (In Italian)," *Nuovo Cim.*, 11, 1–19, [,535(1934)].

Feynman, R. P. and Gell-Mann, M. (1958), "Theory of Fermi interaction," *Phys. Rev.*, 109, 193–198.

Fukuda, S. et al. (2001), "Solar B-8 and hep neutrino measurements from 1258 days of Super-Kamiokande data," *Phys. Rev. Lett.*, 86, 5651–5655.

Fukuda, Y. et al. (1994), "Atmospheric muon-neutrino / electron-neutrino ratio in the multiGeV energy range," *Phys. Lett.*, B335, 237–245.

Fukuda, Y. et al. (1996), "Solar neutrino data covering solar cycle 22," *Phys. Rev. Lett.*, 77, 1683–1686.

Fukuda, Y. et al. (1998), "Evidence for oscillation of atmospheric neutrinos," *Phys. Rev. Lett.*, 81, 1562–1567.

Fukuda, Y. et al. (2003), "The Super-Kamiokande detector," *Nucl. Instrum. Meth.*, A501, 418–462.

Gaisser, T. K. (2013), "Atmospheric leptons," *EPJ Web Conf.*, 52, 09004.

Gamow, G. and Teller, E. (1937), "Some Generalizations of the beta Transformation Theory," *Phys. Rev.*, 51, 289–289.

Glashow, S. L. (1961), "Partial Symmetries of Weak Interactions," *Nucl. Phys.*, 22, 579–588.

Gluck, M., Reya, E., and Vogt, A. (1998), "Dynamical parton distributions revisited," *Eur. Phys. J.*, C5, 461–470.

Goldhaber, M., Grodzins, L., and Sunyar, A. W. (1958), "Helicity of Neutrinos," *Phys. Rev.*, 109, 1015–1017.

Graczyk, K. M. and Sobczyk, J. T. (2008), "Form Factors in the Quark Resonance Model," *Phys. Rev.*, D77, 053001, [Erratum: Phys. Rev.D79,079903(2009)].

Gran, R., Jeon, E., Aliu, E., Andringa, S., Aoki, S., Argyriades, J., Asakura, K., Ashie, R., Berghaus, F., Berns, H., et al. (2006), "Measurement of the quasielastic axial vector mass in neutrino interactions on oxygen," *Physical Review D*, 74, 052002.

Hagiwara, K., Mawatari, K., and Yokoya, H. (2003), "Tau polarization in tau neutrino nucleon scattering," *Nucl. Phys.*, B668, 364–384, [Erratum: Nucl. Phys.B701,405(2004)].

Haino, S. et al. (2004), "Measurements of primary and atmospheric cosmic - ray spectra with the BESS-TeV spectrometer," *Phys. Lett.*, B594, 35–46.

Hampel, W. et al. (1999), "GALLEX solar neutrino observations: Results for GALLEX IV," *Phys. Lett.*, B447, 127–133.

Hasert, F. J. et al. (1973), "Observation of Neutrino Like Interactions Without Muon Or Electron in the Gargamelle Neutrino Experiment," *Phys. Lett.*, 46B, 138–140.

Hayato, Y. (2009), "A neutrino interaction simulation program library NEUT," *Acta Phys. Polon.*, B40, 2477–2489.

Hedin, A. E. (1991), "Extension of the MSIS thermosphere model into the middle and lower atmosphere," *Journal of Geophysical Research: Space Physics*, 96, 1159–1172.

Hernandez, E., Nieves, J., and Valverde, M. (2008), "Neutrino induced weak pion production off the nucleon," *Mod. Phys. Lett.*, A23, 2317–2320.

Hocker, A. et al. (2007), "TMVA - Toolkit for Multivariate Data Analysis," *PoS*, ACAT, 040.

Honda, M., Kajita, T., Kasahara, K., and Midorikawa, S. (2004), "A New calculation of the atmospheric neutrino flux in a 3-dimensional scheme," *Phys. Rev.*, D70, 043008.

Honda, M., Sajjad Athar, M., Kajita, T., Kasahara, K., and Midorikawa, S. (2015), "Atmospheric neutrino flux calculation using the NRLMSISE-00 atmospheric model," *Phys. Rev.*, D92, 023004.

Ishihara, C. (2010), "Full three flavor oscillation analysis of atmospheric neutrino data observed in Super-Kamiokande," Ph.D. thesis, Tokyo U.

Jeong, Y. S. and Reno, M. H. (2010), "Tau neutrino and antineutrino cross sections," *Phys. Rev.*, D82, 033010.

Kajita, T. (2006), "Discovery of neutrino oscillations," *Reports on Progress in Physics*, 69, 1607.

King, S. F. and Luhn, C. (2013), "Neutrino Mass and Mixing with Discrete Symmetry," *Rept. Prog. Phys.*, 76, 056201.

Kodama, K. et al. (2001), "Observation of tau neutrino interactions," *Phys. Lett.*, B504, 218–224.

Kodama, K. et al. (2008), "Final tau-neutrino results from the DONuT experiment," *Phys. Rev.*, D78, 052002.

Kume, H., Sawaki, S., Ito, M., Arisaka, K., Kajita, T., Nishimura, A., and Suzuki, A. (1983), "20-INCH DIAMETER PHOTOMULTIPLIER," *Nucl. Instrum. Meth.*, 205, 443–449.

Lee, K.-P. (2012), "Study of the neutrino mass hierarchy with the atmospheric neutrino data observed in Super-Kamiokande," Ph.D. thesis, University of Tokyo.

Lee, T. D. and Yang, C.-N. (1956), "Question of Parity Conservation in Weak Interactions," *Phys. Rev.*, 104, 254–258.

Levy, J.-M. (2009), "Cross-section and polarization of neutrino-produced tau's made simple," *J. Phys.*, G36, 055002.

Llewellyn Smith, C. H. (1972), "Neutrino Reactions at Accelerator Energies," *Phys. Rept.*, 3, 261–379.

Mead, C. A. (1958), "Quantum Theory of the Refractive Index," *Phys. Rev.*, 110, 359–369.

Michael, D. G. et al. (2006), "Observation of muon neutrino disappearance with the MINOS detectors and the NuMI neutrino beam," *Phys. Rev. Lett.*, 97, 191801.

Mikheev, S. P. and Smirnov, A. Yu. (1985), "Resonance Amplification of Oscillations in Matter and Spectroscopy of Solar Neutrinos," *Sov. J. Nucl. Phys.*, 42, 913–917, [Yad. Fiz.42,1441(1985)].

Motoki, M. et al. (2003), "Precise measurements of atmospheric muon fluxes with the BESS spectrometer," *Astropart. Phys.*, 19, 113–126.

Nakajima, Y. (2011), "A Measurement of Neutrino Charged Current Interactions and a Search for Muon Neutrino Disappearance with the Fermilab Booster Neutrino Beam," Ph.D. thesis, Kyoto U.

Nieves, J., Amaro, J. E., and Valverde, M. (2004), "Inclusive quasielastic charged-current neutrino-nucleus reactions," *Physical Review C*, 70, 055503.

Nieves, J., Ruiz Simo, I., and Vicente Vacas, M. J. (2011), "Inclusive Charged–Current Neutrino–Nucleus Reactions," *Phys. Rev.*, C83, 045501.

Niita, K., Sato, T., Nakashima, H., Iwase, H., Nose, H., and Sihver, L. (2006), "PHITS: A particle and heavy ion transport code system," *Radiat. Meas.*, 41, 1080–1090.

Nishino, H. (2009), "Search for Nucleon Decay into Charged Antilepton plus Meson in Super-Kamiokande," Ph.D. thesis, Tokyo U.

Nishino, H., Awai, K., Hayato, Y., Nakayama, S., Okumura, K., Shiozawa, M., Takeda, A., Ishikawa, K., Minegishi, A., and Arai, Y. (2009), "High-speed charge-to-time converter ASIC for the Super-Kamiokande detector," *Nucl. Instrum. Meth.*, A610, 710–717.

NOAA, U. and Force, U. A. (1976), "US standard atmosphere, 1976," Tech. rep., NOAA-S/T.

Olive, K. A. et al. (2014), "Review of Particle Physics," *Chin. Phys.*, C38, 090001.

Patrignani, C. et al. (2016), "Review of Particle Physics," *Chin. Phys.*, C40, 100001.

Pauli, W. (1930), "Pauli's Letter-Dear Radioactive Ladies and Gentlemen," *Tübingen, December*, 4.

Pohl, M. et al. (1978), "Study of Neutrino Proton Elastic Scattering in the GARGAMELLE Freon Experiment," *Phys. Lett.*, B72, 489–492.

Rein, D. and Sehgal, L. M. (1981), "Neutrino Excitation of Baryon Resonances and Single Pion Production," *Annals Phys.*, 133, 79–153.

Rein, D. and Sehgal, L. M. (1983), "Coherent pi0 Production in Neutrino Reactions," *Nucl. Phys.*, B223, 29–44.

Rein, D. and Sehgal, L. M. (2007), "PCAC and the Deficit of Forward Muons in pi+ Production by Neutrinos," *Phys. Lett.*, B657, 207–209.

Roesler, S., Engel, R., and Ranft, J. (2000), "The Monte Carlo event generator DPMJET-III," in *Advanced Monte Carlo for radiation physics, particle transport simulation and applications. Proceedings, Conference, MC2000, Lisbon, Portugal, October 23-26, 2000*, pp. 1033–1038.

Salam, A. (1968), "Elementary Particle Physics: Relativistic Groups and Analyticity (Nobel Symp. 8), ed," *N. Svartholm*, p. 367.

Salam, A. and Ward, J. C. (1964), "Electromagnetic and weak interactions," *Phys. Lett.*, 13, 168–171.

Sanuki, T. et al. (2000), "Precise measurement of cosmic ray proton and helium spectra with the BESS spectrometer," *Astrophys. J.*, 545, 1135.

Sanuki, T. et al. (2002), "Measurements of atmospheric muon spectra at mountain altitude," *Phys. Lett.*, B541, 234–242, [Erratum: Phys. Lett.B581,272(2004)].

Schael, S. et al. (2006), "Precision electroweak measurements on the Z resonance," *Phys. Rept.*, 427, 257–454.

Schwinger, J. S. (1957), "A Theory of the Fundamental Interactions," *Annals Phys.*, 2, 407–434.

Sekiya, H. (2013), "Solar neutrino analysis of Super-Kamiokande," in *Proceedings, 33rd International Cosmic Ray Conference (ICRC2013): Rio de Janeiro, Brazil, July 2-9, 2013*, p. 0048.

Sjostrand, T. (1995), "PYTHIA 5.7 and JETSET 7.4: Physics and manual," .

Smith, R. A. and Moniz, E. J. (1972), "NEUTRINO REACTIONS ON NUCLEAR TARGETS," *Nucl. Phys.*, B43, 605, [Erratum: Nucl. Phys.B101,547(1975)].

Sudarshan, E. C. G. and Marshak, R. E. (1994), "Origin of the Universal V?A theory," *AIP Conf. Proc.*, 300, 110–124, [,0001(1984)].

Suzuki, A., Mori, M., Kaneyuki, K., Tanimori, T., Takeuchi, J., Kyushima, H., and Ohashi, Y. (1993), "Improvement of 20-inch diameter photomultiplier tubes," *Nucl. Instrum. Meth.*, A329, 299–313.

Thébault, E., Finlay, C. C., Beggan, C. D., Alken, P., Aubert, J., Barrois, O., Bertrand, F., Bondar, T., Boness, A., Brocco, L., et al. (2015), "International geomagnetic reference field: the 12th generation," *Earth, Planets and Space*, 67, 1–19.

Verkerke, W. and Kirkby, D. P. (2003), "The RooFit toolkit for data modeling," *eConf*, C0303241, MOLT007, [,186(2003)].

Weinberg, S. (1967), "A Model of Leptons," *Phys. Rev. Lett.*, 19, 1264–1266.

Wendell, R. et al. (2010), "Atmospheric neutrino oscillation analysis with sub-leading effects in Super-Kamiokande I, II, and III," *Phys. Rev.*, D81, 092004.

Wendell, R. et al. (2012), "Prob3++," `http://www.phy.duke.edu/~raw22/public/Prob3++/`, Accessed: 2017-01-10.

Wilkinson, C., Rodrigues, P., Cartwright, S., Thompson, L., and McFarland, K. (2014), "Reanalysis of bubble chamber measurements of muon-neutrino induced single pion production," *Phys. Rev.*, D90, 112017.

Wolfenstein, L. (1978), "Neutrino Oscillations in Matter," *Phys. Rev.*, D17, 2369–2374.

Woods, R. D. and Saxon, D. S. (1954), "Diffuse Surface Optical Model for Nucleon-Nuclei Scattering," *Phys. Rev.*, 95, 577–578.

Wu, C. S., Ambler, E., Hayward, R. W., Hoppes, D. D., and Hudson, R. P. (1957), "Experimental Test of Parity Conservation in Beta Decay," *Phys. Rev.*, 105, 1413–1414.

Xing, Z.-z. and Zhao, Z.-h. (2016), "A review of $\mu - \tau$ flavor symmetry in neutrino physics," *Rept. Prog. Phys.*, 79, 076201.

Yamada, S. et al. (2010), "Commissioning of the new electronics and online system for the Super-Kamiokande experiment," *IEEE Trans. Nucl. Sci.*, 57, 428–432.

Zeitnitz, C. and Gabriel, T. A. (1994), "The GEANT - CALOR interface and benchmark calculations of ZEUS test calorimeters," *Nucl. Instrum. Meth.*, A349, 106–111.

Biography

Zepeng Li was born February 20, 1989, in Yantai, China. He attended University of Science and Technology of China between 2007 and 2011. He received his Bachelor degree in Physics in 2011. In the same year, he started graduate studies in physics at Duke University. Under the direction of Professor Chris Walter and Professor Kate Scholberg, he worked on the Long-Baseline Neutrino Experiment and the Super-Kamiokande experiment.